Organic Fouling of Desalination Membranes

by

Emily Winona Tow

S.B., Massachusetts Institute of Technology (2012)
S.M., Massachusetts Institute of Technology (2014)

Submitted to the Department of Mechanical Engineering
in partial fulfillment of the requirements for the degree of

Doctor of Philosophy in Mechanical Engineering

at the

MASSACHUSETTS INSTITUTE OF TECHNOLOGY

June 2017

Author .....
Department of Mechanical Engineering
May 12, 2017

Certified by .....
John H. Lienhard V
Abdul Latif Jameel Professor of Water
Director, Abdul Latif Jameel World Water and Food Security Lab
Director, Center for Clean Water and Clean Energy
Director, Rohsenow Kendall Heat Transfer Laboratory
Thesis Supervisor

Accepted by .....
Rohan Abeyaratne
Graduate Officer
Department of Mechanical Engineering

Organic Fouling of Desalination Membranes

by

Emily Winona Tow

Submitted to the Department of Mechanical Engineering
on May 12, 2017, in partial fulfillment of the
requirements for the degree of
Doctor of Philosophy in Mechanical Engineering

Abstract

Energy-efficient desalination and water reuse are necessary to ensure universal access to clean water. Reverse osmosis (RO) is the most efficient desalination process for almost any water source, but it is susceptible to membrane fouling, which can reduce product water quality and raise energy consumption. Fouling can be reduced through (energy-intensive) pretreatment, delayed by membrane coatings, and partially reversed by cleaning. However, poor understanding of fouling physics hinders our ability to predict fouling or design for fouling resistance. Better models of fouling are needed to improve the RO process and provide sustainable sources of desalinated or recycled water to water-scarce communities.

Through experiments and modeling, this thesis compares several desalination systems, quantifies the effect of pressure on fouling, and elucidates mechanisms of foulant removal. An experimental apparatus was created to simulate operating conditions in full-scale RO, forward osmosis (FO), and membrane distillation (MD) desalination systems and compare the fouling behavior of these processes under identical hydrodynamic conditions. In the FO configuration, both fluid streams could be pressurized to experimentally isolate the effects of pressure from other operating conditions that affect fouling. A window in the membrane module allowed in situ visualization of membrane fouling and cleaning at pressures as high as 69 bar. Experiments were complemented by the development of physics-based models that predict the effect of hydraulic pressure on foulant layer properties and flux decline and also enable the calculation of foulant layer thickness from measured flux.

The findings provide new insight into the relative fouling propensity of membrane desalination systems, the factors influencing flux decline, and the mechanisms of foulant removal. Experiments and modeling show that, although flux decline is slower in FO than in RO, the FO membrane accumulates a thicker foulant layer. Furthermore, FO fouling trials at elevated pressure reveal that fouling behavior is not adversely affected by high hydraulic pressure. Despite this, low operating temperature and unfavorable surface chemistry cause RO to be more susceptible to organic fouling than MD and more susceptible to inorganic fouling than FO. However, neither FO nor MD is immune to fouling: FO flux declined as much as RO flux in the pres-

ence of alginate fouling, and MD exhibited rapid flux decline as a result of inorganic fouling. Finally, in situ visualization revealed that osmotic backwashing causes the foulant layer to swell, buckle, and detach in large pieces from both FO and RO membranes, regardless of operating pressure. These findings guide desalination process selection, membrane design, and cleaning protocol development to reduce the energy consumption associated with membrane fouling in desalination.

Thesis Supervisor: John H. Lienhard V
Title: Abdul Latif Jameel Professor of Water
Director, Abdul Latif Jameel World Water and Food Security Lab
Director, Center for Clean Water and Clean Energy
Director, Rohsenow Kendall Heat Transfer Laboratory

Acknowledgments

Let me start with my family. Mom and Dad, your support and encouragement were vital in getting me to MIT and through the trials of graduate school. Thank you for everything. Charles, from our introduction in East Campus to our wedding at the MIT Chapel, my entire MIT experience has been entwined with our journey together. Thank you for being here for me all this time.

I would also like to thank a number of people at MIT who helped me along the way. I am grateful to my advisor, John Lienhard, who gave me the freedom to pursue the research I felt compelled to do, his expert advice when necessary, and all the support I needed to succeed on my chosen career path. My thesis committee members—Gareth McKinley, Rohit Karnik, and Bradley Olsen—gave me their time and shaped the direction of my research. I also appreciate the mentorship I have received over the years from other MIT faculty, including Pierre Lermusiaux, Azra Aksamija, and Tony Patera. I would like to thank my labmates in the Lienhard Research Group for many useful discussions. I would like to thank the Community Care at MIT Medical staff, especially Cathy Dwyer, whose limitless compassion I will never forget. I would also like to acknowledge my brilliant collaborators Ali Trueworthy and Martin Rencken, who contributed substantially to the work presented in Chapters 5 and 6, respectively.

Finally, I would like to acknowledge funding from the King Fahd University of Petroleum and Minerals through the Center for Clean Water and Clean Energy at MIT and KFUPM (Project #R4-CW-11), the Martin Fellowship for Sustainability, and the MIT Deshpande Center for Technological Innovation. This material is based upon work supported by the National Science Foundation Graduate Research Fellowship Program under grant No. 1122374.

Contents

List of Figures

List of Tables

Nomenclature

A	Active layer permeability [m/s-Pa]
A_s	Surface area [m^2]
B	Salt permeation coefficient of active layer [m/s]
C	Concentration [mol/m^3]
D	NaCl diffusion coefficient [m^2/s]
D_h	Hydraulic diameter [m]
D_s	$CaCl_2$ diffusion coefficient [m^2/s]
E	Elastic modulus [Pa]
J_s	Salt molar flux [mol/m^2-s]
J_w	Water flux [m/s]
J_w^*	Asymptotic water flux [m/s]
$J_w^\star$	Normalization flux [m/s]
J_{norm}	Normalized flux [-]
K	Solute resistivity [s/m] (Ch. 2) or salt-in-membrane sorption coefficient [-] (Ch. 3) or bulk modulus [Pa] (Ch. 4)
K_{sp}	Solubility product

L Effective capillary length [m]

P Gauge pressure [Pa]

P_v Vapor pressure [Pa]

R Salt rejection [-] (Ch. 2) or universal gas constant [J/mol-K] (Ch. 5)

S Structural parameter [m]

T Absolute temperature [K]

V Volume [m^3]

V_m Molar volume [m^3/mol]

$\dot{Q}$ Heat transfer rate [W]

$\dot{W}$ Work transfer rate [W]

$\dot{m}$ Mass flow rate [kg/s]

$\dot{m}''$ Mass flux [kg/m^2-s]

a Activity (units vary)

c_p Specific heat at constant pressure [J/kg-K]

d_p Particle diameter [m]

f_d Darcy friction factor [-]

g Specific Gibbs energy [J/kg]

h Heat transfer coefficient [W/m^2-K]

h_{fg} Latent heat of vaporization [J/kg]

k Mass transfer coefficient [m/s]

k_m Membrane thermal conductivity [W/m-K]

k_w Water thermal conductivity [W/m-K]

l Channel length [m]

s Salinity or solute mass fraction [kg solute/kg solution]

t Time [s]

$t^\star$ Normalization time [s]

u Uncertainty (units vary)

v Velocity [m/s]

x Distance coordinate perpendicular to membrane [m]

Nu Nusselt number [-]

Pr Prandtl number [-]

Re Reynolds number [-]

Sc Schmidt number [-]

Sh Sherwood number [-]

MR Mass flow rate ratio [-]

MR* Analytical optimum mass flow rate ratio [-]

RR Recovery ratio [-]

SI Saturation index [-]

SR Salt consumption ratio [-]

α Dispersivity, as defined in Eq. 3.14 [m]

δ Thickness [m]

δ_c Channel thickness [m]

δ_m Membrane thickness [m]

$\dot{\Xi}$ Exergy flow rate [W]

ϵ Porosity [-]

ϵ_c Cleaning effectiveness [-]

η Exergetic efficiency [-]

γ Surface tension [N/m]

μ Dynamic viscosity [Pa-s]

ν Kinematic viscosity [m^2/s] or Poisson's ratio [-] (Ch. 4)

ω Foulant mass fraction in feed [-]

ϕ Porosity (water volume fraction) [-]

π Osmotic pressure [Pa]

ρ Density [kg/m^3]

σ Inhomogeneity factor [-]

τ Tortuosity [-]

ξ Specific exergy [J/kg]

Subscripts:

0 Environment (Ch. 2) or foulant-free (Ch. 3)

A Active layer (Ch. 3) or alginate (Ch. 4)

C Cake layer

D Osmotic dilution (Ch. 2) or draw boundary layer (Ch. 3) or deposition (Ch. 4)

F	Fuel (Ch. 2) or feed boundary layer (Ch. 3)
R	Regenerator
S	Salt (Ch. 2) or support layer (Ch. 3)
T	Terminal
X	FO exchanger
a	Apparent (Ch. 3) or after cleaning (Ch. 4)
act	Actual
b	Interface between support layer and draw (Ch. 3) or before cleaning (Ch. 4) or bulk (Ch. 5)
c	Concentrated brine (Ch. 2) or interface between cake and feed (Ch. 3)
d	Draw stream (Ch. 2 and 3) or draw/permeate (Ch. 4)
dc	Concentrated draw
dd	Diluted draw
f	Feed
h	Heating fluid
i	In
$least$	Thermodynamic minimum
m	Interface between membrane and cake (Ch. 3) or at membrane (Ch. 5)
o	Out
p	Permeate
p'	Fictitious permeate

s	Saline stream (Ch. 2) or interface between active layer and support layer (Ch. 3)
u	Uncompressed
w	Water
eff	Effective

Chapter 1

Introduction

The severity of global water scarcity is increasing due to population growth and, to a lesser degree, climate change [16]. Water conservation, reuse, and desalination all have parts to play in ensuring universal access to water for agriculture, industry, and domestic uses such as drinking and sanitation. Desalination processes, which produce drinkable water by removing salts from water sources like seawater, saline groundwater, and municipal wastewater can now operate at a fraction of the energy consumption of conventional distillation [17]. However, desalination still comes with a significant energy consumption [18] and carbon footprint [19].

Reverse osmosis (RO) is the most energy-efficient process for desalinating almost any water source [2, 20], and innovations in membrane materials [21] and process design [22] continue to reduce its energy consumption. However, concerns about membrane fouling inhibit the use of RO in high fouling potential applications such as the remediation of produced water from hydraulic fracturing [1]. Our inability to sufficiently mitigate fouling in RO is one of the main drivers of the development of the forward osmosis (FO) and membrane distillation (MD) desalination processes, which are less efficient than RO [23, 24] but are reported to resist fouling [9, 25].

Membrane fouling occurs due to the buildup of various foulants, including microbes, dissolved solutes, and suspended solids, as well as membrane damage by contaminants such as oils and chlorine [25, 26, 27]. Membrane fouling can lead to declining water production, increasing salt permeation, and higher energy consumption

and water cost. Fouling can be prevented to some extent through feed water pretreatment and specialized membrane coatings, and can also be partially or fully reversed by cleaning the membrane with detergents, acidic or alkaline solutions, chelating agents, or biocides [28]. The rate of membrane performance decline between cleanings and the time before the irreversible effects of fouling necessitate membrane replacement can affect the economic viability of an RO desalination plant, but current fouling models (e.g., [29]) that rely on fitting parameters are insufficient to guide the design of energy-efficient and fouling-resistant RO systems.

Better models of membrane fouling and cleaning are needed to reduce the energy consumption associated with membrane fouling, replace energy-intensive distillation processes with efficient RO, and provide affordable desalinated water to water-scarce communities. Through modeling and experiments, this thesis aims to improve understanding of membrane fouling in desalination and enable more efficient fouling mitigation.

1.1 Approach

The need for efficient fouling mitigation stems from the high energy requirement of desalination systems and the impact of fouling on both energy consumption and process selection. Therefore, in Ch. 2, the energy requirements of desalination are compared across a wide range of technologies and water sources. Although FO is a fouling-resistant process, it is found to be inefficient relative to other technologies, and potential improvements in FO efficiency are quantified through modeling.

Design of highly energy-efficient desalination plants will depend on the ability to predict membrane performance and choose pretreatment steps, membranes, operating parameters, and cleaning protocols accordingly. Predictive models should be capable of predicting both the rate of foulant accumulation and performance decline of a given membrane based on the water source and operating conditions. Chapter 3 models the relationship between foulant accumulation and flux decline in RO and FO and, through experiments, elucidates the influence of feed ionic composition on

mechanisms of flux decline.

To create a predictive model of fouling, the effects of individual variables on membrane fouling must be isolated and understood. Pressure is of particular interest due to widespread claims that it "compacts" foulants and causes irreversible fouling (see, e.g., Refs. [9, 10, 11, 12]). In Ch. 4, the effect of pressure on fouling is experimentally isolated by pressurizing both sides of an FO module, revealing that hydraulic pressure alone does not compact foulants or reduce fouling reversibility.

Comparisons of fouling propensity and energy efficiency between different desalination systems help to prioritize research and development. Although energy-intensive, MD is considered to be fouling-resistant despite the lack of direct comparisons to other membrane desalination systems. In Ch. 5, the fouling behavior of MD is compared to RO and FO using a single membrane module that can be configured for each system. Although high temperature improves MD's resistance to organic fouling and membrane chemistry enhances FO's resistance to scaling, no one system is resistant to both organic and inorganic foulants.

Even if fouling is unavoidable, it may be reversed through cleaning. Developing targeted cleaning processes that are effective, energy-efficient, and environmentally-friendly relies on understanding the physics of foulant removal. In Ch. 6, in situ visualization is used to elucidate foulant removal mechanisms and identify a promising method of chemical-free foulant removal: swelling-induced detachment.

Through isolating variables affecting fouling, comparing systems' fouling behaviors, and elucidating foulant removal mechanisms, this thesis informs the design of membranes and cleaning processes. Futhermore, the results of this study form a basis for predictive modeling of fouling, which is an essential step toward the creation of highly-efficient desalination and water reuse systems.

Chapter 2

Energy consumption in forward osmosis desalination

This chapter is based a paper by Tow, McGovern and Lienhard [20].

2.1 Introduction

Forward osmosis (FO) is a promising technology for oil and gas (O&G) wastewater treatment [1, 30] because it can concentrate wastewater to high salinities that are currently unattainable with reverse osmosis (RO). FO may also be a suitable treatment method for other high fouling potential water streams because it is considered to be a fouling-resistant process [1]. In FO, a stream is concentrated as water is drawn from it through a semi-permeable membrane by the high osmotic pressure of a draw solution. Zhao et al. [31] provide a review of the FO process and its applications. FO desalination plants take FO from a pretreatment process to a desalination system by integrating draw regeneration by thermal or membrane processes. In this chapter, we consider FO systems with regeneration except where noted. The efficacy of FO in O&G wastewater desalination has been demonstrated by several pilot plants with varying regeneration systems [1], but energy consumption has yet to be optimized. We will show that reductions in energy consumption may arise from improvements to the FO exchangers, regeneration systems, and system flow rate balance.

Balancing is a method of reducing entropy generation within exchange devices and improving system efficiency through the careful choice of flow rates. Balancing improves gained output ratio (GOR) in humidification dehumidification desalination systems [32, 33, 34, 35, 36] and generally improves efficiency in other applications involving heat and/or mass exchange [37]. Thermodynamically balancing RO, for example, leads to an efficiency improvement of 4.3 percentage points at fixed membrane size and productivity [37]. In the case of FO brine concentration, balancing involves optimizing the ratio of feed and draw flow rates to match osmotic pressure differences on feed and concentrate sides to raise the FO exchanger efficiency, which in turn raises the efficiency of the system.

In this chapter, we first evaluate the exergetic efficiency of FO systems and compare them to conventional technologies operating at similar salinities. We then outline an approach to thermodynamically balance the FO exchanger and show the potential of balancing to improve the efficiency of existing FO pilot plants.

2.2 Exergetic efficiency of brine concentration

Exergetic efficiency quantifies how much room still exists for reduction of energy consumption in a given process. In this section we define exergetic efficiency for brine concentration processes, and in Sec. 2.2.1 we assess the efficiency of various processses including FO.

As shown in Fig. 2-1, a generic FO brine concentration system consists of an FO exchanger, in which brine is concentrated by osmosis as a draw solution is diluted, and a regeneration system, which takes in diluted draw and produces permeate and concentrated draw solution. Although the forward osmosis exchanger consumes minimal energy (in the form of low pressure pump work), the regeneration step is energetically costly.

Exergetic brine concentration efficiency compares the least exergy of separating the saline waste stream into concentrate and permeate (which is a purely thermodynamic quantity) to the actual exergy consumed in the process, which is larger due to

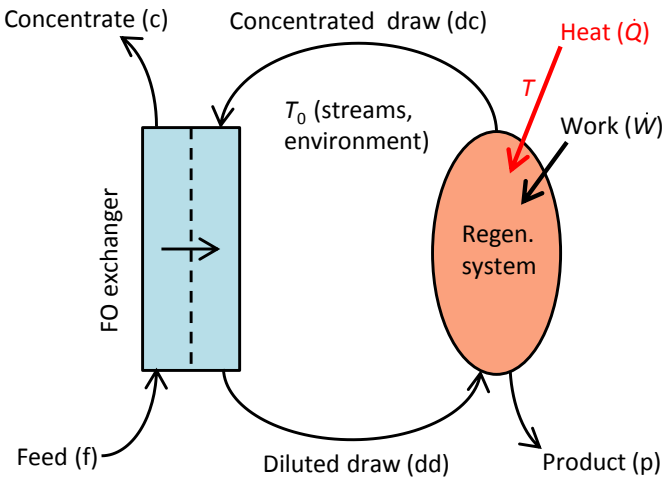

Figure 2-1: Schematic diagram of an FO desalination system consisting of an FO exchanger and a regeneration system (e.g., RO or distillation). Pre- and post-treatment may also be necessary, but are not considered in this analysis.

irreversibilities in the system. Equation 2.1 gives the exergetic efficiency, η, of brine concentration:

$$\eta = \frac{\text{least exergy of separation}}{\text{actual exergy consumption}} = \frac{\dot{\Xi}_{least}}{\dot{\Xi}_{act}}. \tag{2.1}$$

In contrast to the desalination efficiency defined by Mistry and Lienhard [38], which uses the *minimum*[1] least exergy of separating fresh water from a saline stream, the definition employed here uses the least work for a given recovery ratio because in many FO applications (including O&G wastewater treatment) there is value in not only in producing permeate but also in reducing the volume of the feed stream. The exergetic efficiency of brine concentration processes is discussed further in [2]. The least work of separation, $\dot{\Xi}_{least}$, in Eq. 2.1 is given by Eq. 2.2 [17] for a system where all streams enter and leave at atmospheric temperature and pressure:

$$\dot{\Xi}_{least} = \dot{m}_p g_p + \dot{m}_c g_c - \dot{m}_f g_f, \tag{2.2}$$

where $\dot{m}$ and g are mass flow rate and specific Gibbs energy, respectively.

Draw regeneration systems take in exergy in the form of work, heat transfers (HT),

[1]Corresponding to an infinitesimal recovery ratio, which is defined in Eq. 2.11.

and fuel combustion. The actual exergy consumed, $\dot{\Xi}_{act}$, is expanded in Eq. 2.3:

$$\dot{\Xi}_{act} = \underbrace{\dot{Q}\left(1 - \frac{T_0}{T}\right)}_{\text{isothermal HT}} + \underbrace{\dot{m}_h(\xi_{h,i} - \xi_{h,o})}_{\text{non-isothermal HT}} + \underbrace{\dot{m}_F \xi_F}_{\text{fuel}} + \underbrace{\dot{W}}_{\text{work}}. \tag{2.3}$$

$\dot{Q}$ is the isothermal heat transfer rate at temperature T (e.g., by condensation of steam), and T_0 is the temperature of the environment. $\dot{m}_h$, $\xi_{h,i}$, and $\xi_{h,o}$ are the mass flow rate, specific exergy in and specific exergy out, respectively, of any non-isothermal heating fluid streams. $\dot{m}_F$ and ξ_F are the mass flow rate and exergetic value of any fuels used. Exergetic values of fuels are given in [39]. $\dot{W}$ is the total work transfer rate (e.g., electrical power).

Substituting Eqs. 2.2 and 2.3 into Eq. 2.1, we can compute the efficiency of any brine concentration system, including FO:

$$\eta = \frac{\dot{m}_p g_p + \dot{m}_c g_c - \dot{m}_f g_f}{\dot{Q}\left(1 - \frac{T_0}{T}\right) + \dot{m}_h(\xi_{h,i} - \xi_{h,o}) + \dot{m}_F \xi_F + \dot{W}}. \tag{2.4}$$

Equation 2.4 is used to evaluate the exergetic efficiencies of FO brine concentration systems and conventional desalination methods in the following section.

2.2.1 Assessment of technologies

The efficiency of brine concentration is visualized in this section with an efficiency-salinity map, Fig. 2-2. The need for a two-dimensional rating of efficiency stems from the optimization of different processes for particular salinity ranges (e.g., EDR for low-salinity brackish applications) and the effect of salinity on least work of separation.

The values of FO efficiency that appear in the efficiency-salinity map are calculated using the limited FO pilot plant energy consumption data available in the open literature. McGinnis et al. [3] describe the operation of an FO pilot plant that uses an ammonia-carbon dioxide draw solution and thermal draw regeneration to concentrate high-salinity O&G wastewater from the Marcellus and Permian Basin shale regions. This thermal FO pilot uses a distillation column to regenerate the draw, but other

thermal draw regeneration types have been proposed or investigated at the lab scale, including mechanical vapor compression (MVC) [3], membrane distillation (MD) [40], and multi-stage flash (MSF) [41]. Thermally-regenerated FO has also been modeled by Semiat et al. [42]. An FO pilot system with RO regeneration (FO-RO) was used to concentrate low-salinity O&G wastewater [1, 4]. FO-RO has also been suggested to be more efficient than RO for seawater desalination [5, 43], but other studies have shown that this is unlikely [23, 44]. Another FO pilot plant forgoes draw regeneration in favor of "osmotic dilution" [1, 4]: the dilution of a pure sodium chloride solution powers the concentration of O&G wastewater. Osmotic dilution is also used in emergency hydration [45], fertigation [46], and other applications described in [47].

In addition to three existing FO brine concentration pilots, plant efficiency data for seawater RO (SWRO), brackish water RO (BWRO), electrodialysis (EDR), MSF, and high-salinity MVC are included for comparison. Models of seawater FO-RO and high-salinity MVC as well as typical efficiencies of MVC and multi-effect distillation with thermal vapor compression (TVC-MED) are also given. The assumptions made in constructing Fig. 2-2 are discussed in App. A.1. In Fig. 2-2, arrows are drawn from the feed salinity to the concentrate salinity at the efficiency of the process.

The efficiency-salinity map (Fig. 2-2) can be used to choose energy-efficient desalination technologies for specific applications by first locating the desired salinity range on the horizontal axis and then moving up until reaching the most efficient technology.

Figure 2-2 shows that FO, in its current state, is not the most efficient technology at any salinity. At brackish and seawater salinities, RO is more efficient than FO. Due to irreversible water transport in the FO exchanger, this will probably always be the case [23]. At high salinities, the efficiency of FO with thermal draw regeneration is currently lower that of MVC [2] because of that pilot plant's use of simple distillation for draw regeneration. However, several advanced thermal draw regeneration processes have been proposed [3, 40, 41] that may contribute to raising thermal FO efficiency.

Due to the absence of a regeneration step, the osmotic dilution process has a

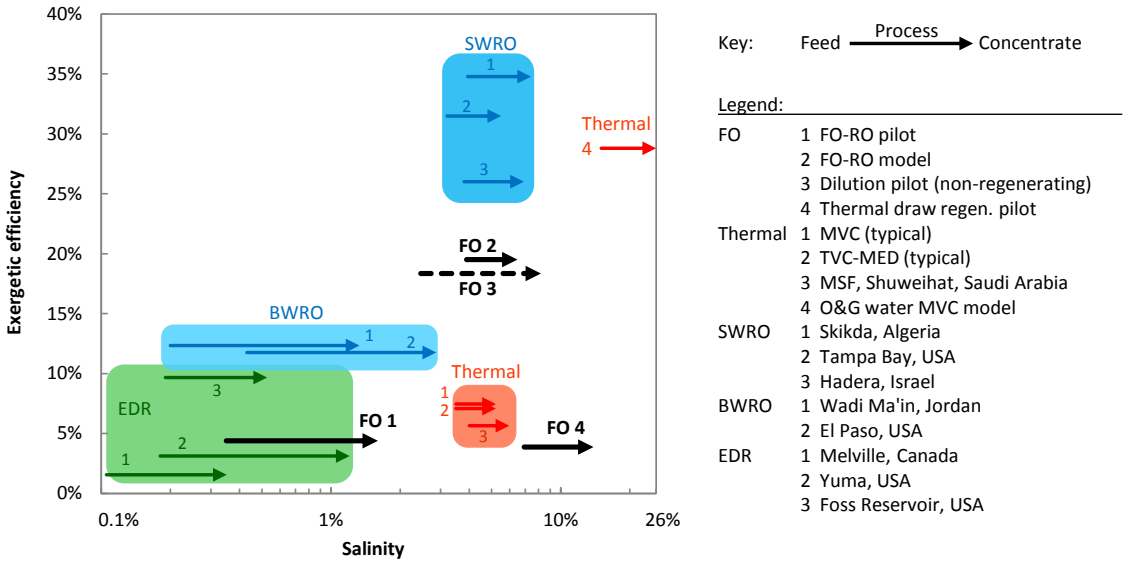

Figure 2-2: Efficiency-salinity map of desalination processes including FO. Efficiency is calculated with Eqs. 2.4 and A.1 using data reported in Refs. [1, 2, 3, 4, 5, 6, 7, 8]. Processes are represented with arrows that begin and end at the feed and concentrate salinities, respectively.

relatively high exergetic efficiency (as defined in App. A.1). However, in the Hutchings et al. pilot [4], at least 75 kg of NaCl must be consumed per cubic meter of water removed from the feed (see App. A.2), and the process produces saline water rather than fresh water. Draw solutes other than NaCl may be used, but in each case the cost of sourcing the solute and the cost of disposing (or value of producing) the dilute draw must be considered. This process might be a good choice for wastewater volume reduction when clean brine production is also desired.

In some cases, the advantages of FO may outweigh the disadvantage of low efficiency. For example, FO is reported to be more resistant to fouling than RO [1, 48, 49], and it has been shown that membrane fouling is more easily reversible in FO than in RO operated under similar conditions [9]. The fouling behavior of FO relative to RO is further discussed in Chapters 3–6.

2.3 FO exchanger efficiency

As it is for most systems, the overall efficiency of an FO brine concentration system is related to the efficiencies of its components. A basic FO system such as that depicted in Fig. 2-1 consists of two components: an FO exchanger and a draw regenerator. Both components require external exergy inputs: a substantial exergy input in the regenerator, $\dot{\Xi}_R$, and the much smaller power consumption of the FO exchanger, $\dot{W}_X$. The total exergy consumption of the system is $\dot{\Xi}_{act}$, Eq. 2.3.

The regenerator carries out a separation of the dilute draw solution into permeate and concentrated draw. Here, the least exergy is that of separating the dilute draw stream (equivalent to the mixing work of combining pure and concentrated draw streams), $\dot{\Xi}_{least,R}$:

$$\dot{\Xi}_{least,R} = \dot{m}_p g_p + \dot{m}_{dc} g_{dc} - \dot{m}_{dd} g_{dd}, \tag{2.5}$$

and the actual exergy is $\dot{\Xi}_R = \dot{\Xi}_{act} - \dot{W}_X$. Substituting these expressions into Eq. 2.1 results in the regeneration system efficiency, η_R:

$$\eta_R = \frac{\dot{m}_p g_p + \dot{m}_{dc} g_{dc} - \dot{m}_{dd} g_{dd}}{\dot{\Xi}_{act} - \dot{W}_X}. \tag{2.6}$$

In systems with regeneration, an FO exchanger efficiency[2] can be defined. Forward osmosis is a spontaneous process, and the transfer of water down a chemical potential gradient is inherently lossy. An exchanger efficiency reflects the exergy destruction in the FO exchanger by comparing the minimum exergy needed to remove water from the feed to the exergy needed to remove the same water from the draw plus the work required by the FO exchanger. The exergetic efficiency of the exchanger can then be expressed as a ratio of the least work of desalinating the feed (Eq. 2.2) to the least work of separating the draw (Eq. 2.5) plus the parasitic power consumption associated with overcoming hydraulic losses within the FO exchanger:

$$\eta_X = \frac{\dot{m}_p g_p + \dot{m}_c g_c - \dot{m}_f g_f}{\dot{m}_p g_p + \dot{m}_{dc} g_{dc} - \dot{m}_{dd} g_{dd} + \dot{W}_X}. \tag{2.7}$$

[2]The exchanger efficiency should not be confused with the exchanger effectiveness [50], which quantifies the achieved fraction of water recovery.

The exergetic efficiency of the FO unit varies between 0 for no transfer of water and 1 for an ideal exchanger with zero osmotic pressure difference everywhere and no parasitic work consumption. Current pilot plant exchanger efficiencies are in the range of 8-45% (see Sec. 2.4.2).

The numerator of regenerator efficiency and the denominator of exchanger efficiency are identical (neglecting the parasitic exchanger power consumption) because the draw streams do not cross the system boundary, but only move between components. By relating the component efficiencies to the system efficiency, we can see how changes to each component affect system performance. Using Eqs. 2.6 and 2.7, the efficiency a brine concentration system as defined by Eqs. 2.1 and 2.2 may be written as a function of the component efficiencies:

$$\eta = \eta_X \eta_R \Big(\frac{\dot{m}_p g_p + \dot{m}_{dc} g_{dc} - \dot{m}_{dd} g_{dd} + \dot{W}_X}{\dot{m}_p g_p + \dot{m}_{dc} g_{dc} - \dot{m}_{dd} g_{dd} + \dot{W}_X \eta_R} \Big). \tag{2.8}$$

In the case that the hydraulic pressure drop through the FO channels (e.g., 2.8 bar in [3]) is much less than the osmotic pressure of the draw, as would typically occur in FO, $\dot{W}_X \ll \dot{m}_p g_p + \dot{m}_{dc} g_{dc} - \dot{m}_{dd} g_{dd}$ and the system efficiency reduces to Eq. 2.9:

$$\eta \approx \eta_X \eta_R. \tag{2.9}$$

Equation 2.9 shows that the efficiencies of the FO exchanger and the regeneration step are equally important in determining the system efficiency. Regeneration efficiency improvements tend to require increased complexity (e.g., through multistage designs) and/or increased exchanger area (e.g., of RO membrane), both of which add capital cost. Therefore, in the following section we focus on improving the exchanger efficiency inexpensively by optimizing flow rates through the FO exchanger.

2.4 FO exchanger balancing

FO system efficiency can potentially be raised by improving regeneration, improving the FO exchanger (e.g., through innovation in membranes [51] or draw solutions [52]),

or by balancing flow rates throughout the system. Improvements to components can be expensive, but balancing has been shown to raise efficiency at a fixed exchanger area [37]. Therefore, in this section, we will describe thermodynamic balancing as it applies to FO exchangers and quantify its potential to improve FO system efficiency. Parallel-flow exchangers are inherently unbalanced, so only counterflow FO exchangers are considered in this analysis.

Balancing aims to improve the system efficiency at a fixed exchanger area by optimizing the ratio of the mass flow rates entering the exchanger on the draw and feed sides, MR:

$$\mathrm{MR} \equiv \frac{\dot{m}_{dc}}{\dot{m}_f}. \tag{2.10}$$

Rather than numerically modeling particular systems,we approach balancing analytically in this section, using fixed terminal osmotic pressure difference as a proxy for fixed exchanger area. The terminal osmotic pressure difference, $\Delta\pi_T$, is the minimum difference between feed and draw stream osmotic pressures at either end of the FO exchanger.[3] As the mass flow rate ratio is varied, $\Delta\pi_T$ is kept constant to minimize the effect on exchanger size and cost.

Recovery ratio defines the mass fraction of the feed that is removed as permeate:

$$\mathrm{RR} \equiv \frac{\dot{m}_p}{\dot{m}_f} = 1 - \frac{s_f}{s_c}. \tag{2.11}$$

Because of its limited effect on exergetic efficiency, salt permeation through the FO membrane is neglected in this analysis.

Exchanger efficiency (Eq. 2.7) may be written as a function of MR for a fixed feed salinity, recovery ratio, and terminal osmotic pressure difference. Mass flow rates in Eq. 2.7 can be normalized by $\dot{m}_f$: $\dot{m}_p/\dot{m}_f = \mathrm{RR}$, $\dot{m}_c/\dot{m}_f = 1-\mathrm{RR}$, $\dot{m}_{dc}/\dot{m}_f = \mathrm{MR}$ and $\dot{m}_{dd}/\dot{m}_f = \mathrm{MR}+\mathrm{RR}$. The Gibbs energy of each stream depends on its salinity (or osmotic pressure). When the minimum osmotic pressure difference occurs at the

[3]Contrary to the German proverb, *alles hat ein Ende nur die Wurst hat zwei*, a counterflow FO exchanger *also* has two ends with corresponding osmotic pressure differences. The minimum of the two is considered the terminal osmotic pressure difference, $\Delta\pi_T$.

feed inlet,

$$s_{dd,f} = s_d|_{\pi_f + \Delta\pi_T}, \tag{2.12}$$

and concentrated draw salinity can be computed with Eq. A.6:

$$s_{dc,f} = \frac{\text{MR+RR}}{\text{MR}}\, s_d|_{\pi_f + \Delta\pi_T}. \tag{2.13}$$

Similarly, when $\Delta\pi_T$ is at the concentrate side,

$$s_{dc,c} = s_d|_{\pi_c + \Delta\pi_T}, \tag{2.14}$$

and

$$s_{dd,c} = \frac{\text{MR}}{\text{MR+RR}}\, s_d|_{\pi_c + \Delta\pi_T}. \tag{2.15}$$

To enforce a minimum terminal osmotic pressure difference of $\Delta\pi_T$, we use a piecewise expression for exchanger efficiency that is the minimum of the efficiencies that would be calculated for minimum osmotic pressure differences occurring at the feed and concentrate sides at a given MR. Therefore, the denominator contains the maximum of the expressions for draw stream mixing work that correspond to the two possible terminal locations of the minimum osmotic pressure difference. Substituting the above relationships into Eq. 2.7, we arrive at an expression for exchanger efficiency as a function of MR:

$$\begin{aligned}\eta_X = {} & [\text{RR}\; g_p + (1 - \text{RR})\; g_c - g_f] \\ & \times \Bigg(\text{RR}\; g_p + \max\; \Big\{ [\text{MR}\; g_d|_{s_{dc,f}} - (\text{MR} + \text{RR})\; g_d|_{s_{dd,f}}], \\ & \qquad [\text{MR}\; g_d|_{[s_{dc,c}} - (\text{MR} + \text{RR})\; g_d|_{s_{dd,c}}] \Big\} + \frac{\dot{W}_X}{\dot{m}_f} \Bigg)^{-1}. \end{aligned} \tag{2.16}$$

In Eq. 2.16, $s_{dc,f}$, $s_{dd,f}$, $s_{dc,c}$, and $s_{dd,c}$ (Eqs. 2.12 through 2.15) are themselves functions of MR.

Exchanger efficiency (Eq. 2.16) is evaluated in Fig. 2-3 over a range of mass flow rate ratios to demonstrate the importance of balancing. In Fig. 2-3, both streams

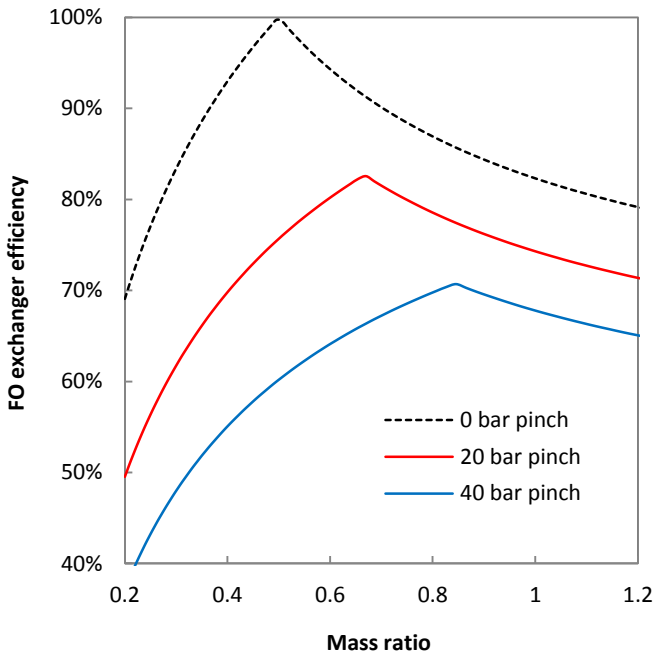

Figure 2-3: Importance of balancing: FO exchanger efficiency depends on mass flow rate ratio

are NaCl solutions, the feed salinity is 8% by mass, the recovery ratio is 50%, and parasitic power consumption is neglected. As the mass flow rate ratio approaches the optimal mass flow rate ratio, the exchanger efficiency rises. Because system efficiency is the product of FO exchanger and regenerator efficiencies (see Eq. 2.9), any improvement in exchanger efficiency due to balancing results in a roughly proportional improvement in system efficiency for systems with relatively salinity-independent regeneration efficiency.

The sharp peak in efficiency seen in Fig. 2-3 results from fixing the terminal osmotic pressure difference (which causes the maximum in the denominator of Eq. 2.16); if instead a fixed exchanger length were imposed, the curves would be smoother.

Conceptually, balancing works by maintaining a relatively uniform osmotic pressure difference throughout the exchanger to minimize entropy generation and maximize efficiency while maintaining sufficient mass flux everywhere. Figure 2-4 demonstrates the effect of balancing at a fixed terminal osmotic pressure difference (35 bar, based on the low-salinity FO-RO pilot [1, 4]) using salinity profiles derived in App.

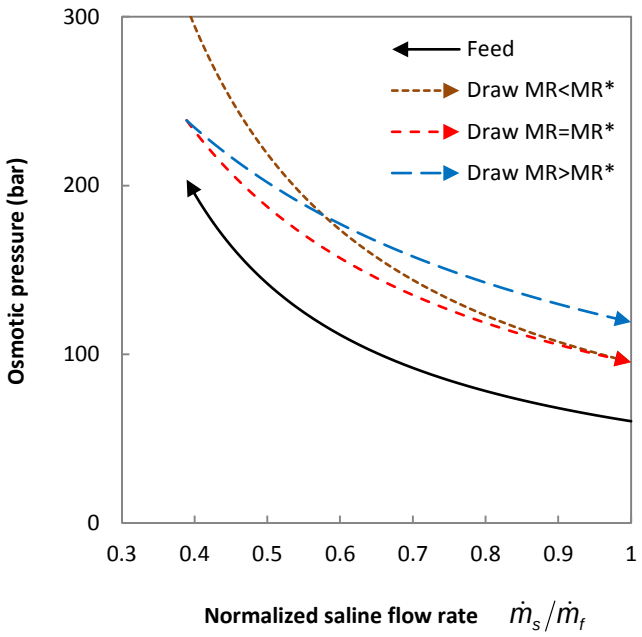

Figure 2-4: The effect of balancing on the draw salinity profile for an exchanger with $\Delta\pi_T = 35$ bar. MR = MR* represents an analytically balanced exchanger.

A.3. As the mass flow rate ratio is varied, the slope of the draw salinity profile changes. Larger mass flow rate ratios lead to a smaller change in draw salinity but require that a larger mass flow rate goes through the regeneration device. Smaller mass flow rate ratios minimize the mass flow rate through the regenerator, but require a larger change in draw salinity. Somewhere in the middle, an optimal mass flow ratio exists that maximizes the exchanger efficiency.

The optimal mass flow rate ratio can be found numerically (as in Fig. 2-3) or analytically. In general, the mass flow rate ratio is a function of the recovery ratio and the draw salinities at the two ends of the FO exchanger:

$$\mathrm{MR} = \mathrm{RR}\,\frac{s_{dd}}{s_{dc} - s_{dd}}. \tag{2.17}$$

When MR=MR*,

$$\mathrm{MR}^* = \frac{\mathrm{RR}\; s_d|_{\pi_f+\Delta\pi_T}}{s_d|_{\pi_c+\Delta\pi_T} - s_d|_{\pi_f+\Delta\pi_T}}, \tag{2.18}$$

the osmotic pressure difference is equal on feed and concentrate sides.

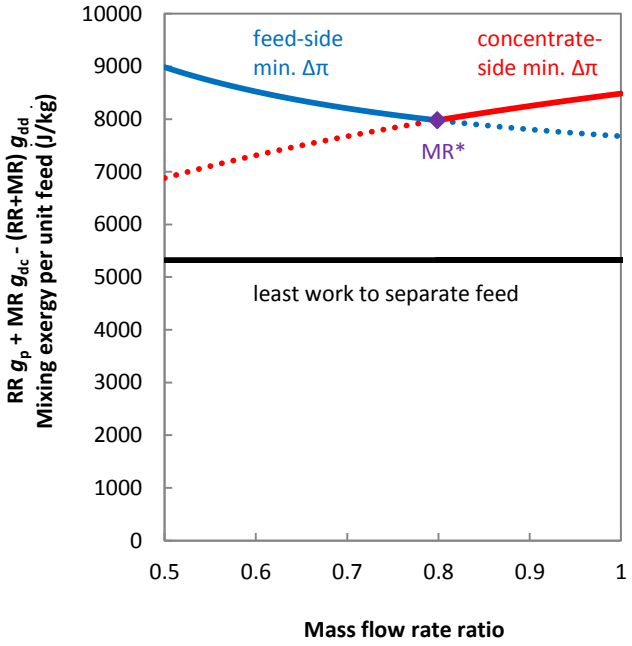

Figure 2-5: Effect of mass flow rate ratio on the denominator of exchanger efficiency, showing that it is minimized at MR=MR* for a feed salinity of 8% by mass, RR of 50%, 35 bar terminal osmotic pressure difference, and 2 bar hydraulic losses in the exchanger.

To find the optimal mass flow rate ratio analytically, we examine the effect of MR on η_X, Eq. 2.7. When the hydraulic pressure drop in the FO exchanger is very small compared to the feed osmotic pressure, as it is in Fig. 2-5, the change in the parasitic work term in exchanger efficiency ($\dot{W}_X/\dot{m}_f$) with changes in MR is small compared to the change in the mixing work (Eq. 2.5) of the draw per unit mass of feed, $[\dot{\Xi}_{least,R}/\dot{m}_f = \mathrm{RR}\, g_p + \mathrm{MR}\, g_{dc} - (\mathrm{MR}+\mathrm{RR})\, g_{dd}]$. As shown in Fig. 2-5, when MR is such that the minimum osmotic pressure difference occurs on the feed side ($\mathrm{MR} \leq \mathrm{MR}^*$), this mixing work decreases with increasing MR, and when $\Delta\pi_T$ is on the concentrate side ($\mathrm{MR} \geq \mathrm{MR}^*$), the mixing work increases with increasing MR. Therefore, the minimum mixing work occurs when the terminal osmotic pressure difference is the same at both ends ($\mathrm{MR} = \mathrm{MR}^*$). Mixing work is in the denominator of exchanger efficiency, and when the parasitic work can be neglected, the expression for MR* (Eq. 2.18) is the mass flow rate ratio that maximizes FO exchanger efficiency.

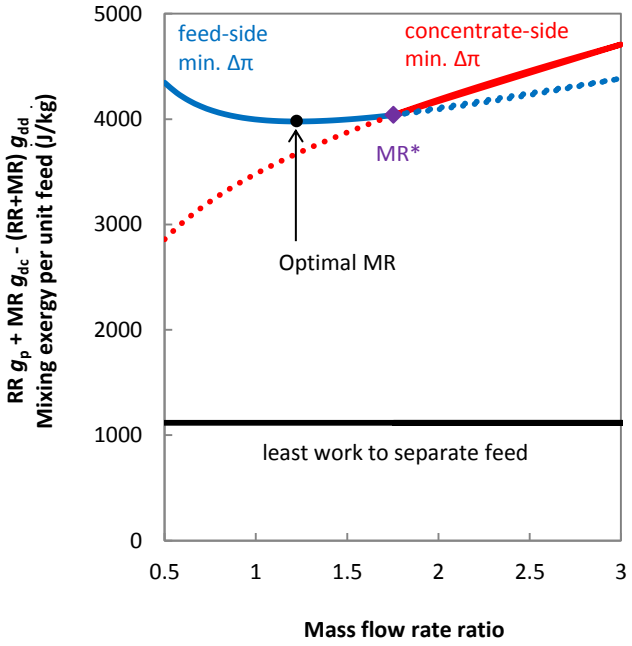

Figure 2-6: Effect of mass flow rate ratio on the denominator of exchanger efficiency in low salinity operation, showing that the optimal MR occurs below MR*. Here, feed salinity is just 2%, RR is 50%, $\Delta\pi_T = 35$ bar, and hydraulic losses in the exchanger are 2 bar.

2.4.1 Limitations

The analytical expression for optimal mass flow rate ratio is based on fixing the terminal osmotic pressure difference and the approximations of low parasitic power consumption and salinity-independent regenerator efficiency. Therefore, Eq. 2.18 has some limitations.

In low-salinity FO brine concentration, MR* (Eq. 2.18) does not predict the optimal mass flow rate ratio, as shown in Fig. 2-6. Here, the hydraulic pressure loss is significant relative to the feed osmotic pressure, and the variation of the parasitic work term with varying MR cannot be neglected. Numerical optimization, rather than Eq. 2.18, must be used in low-salinity applications such as wastewater treatment with FO membrane bioreactors [53].

Numerical modeling can also be employed to account for internal concentration polarization (ICP), which affects the required membrane area in FO. Assuming op-

eration in FO mode (membrane active layer facing the feed to minimize fouling [54]), and neglecting external concentration polarization, the flux at any point in an FO exchanger is given by Eq. 2.19 [54]:

$$J_w = A[\pi_d \exp(-J_w K) - \pi_s], \tag{2.19}$$

where J_w is the water flux into the draw side, A is the membrane active layer permeability, π_d and π_s are the local osmotic pressures of the draw and feed streams, respectively, and K is the solute resistivity of the FO membrane support layer. Eq. 2.19 shows that the nearly-uniform osmotic pressure difference enforced by Eq. 2.18 would cause flux to vary throughout the exchanger, which may not be optimal.

Changing the mass flow rate ratio at a fixed terminal osmotic pressure difference requires some change in exchanger area and cost. However, numerically optimizing the mass flow rate ratio at a fixed exchanger area would still improve efficiency according the the theory described in [37]. Analytically balancing the FO exchanger alone also neglects the change in regenerator efficiency with draw salinity, which may be most pronounced with thermal regeneration methods. Future work on numerical modeling of balancing in FO systems could quantify the effect of balancing at a fixed exchanger length including the effects of ICP, parasitic power consumption, and regeneration system efficiency.

2.4.2 Applications

Optimizing the mass flow rate ratio can improve the efficiency of real systems. In Fig. 2-7, mass flow rate ratio is varied for the FO exchangers used in the low-salinity FO-RO pilot [1, 4] and the thermal FO pilot [3] as well as the seawater FO-RO model by Nicoll [5]. The osmotic dilution pilot [4] is not included in Fig. 2-7 because it is more practical to minimize salt use (see App. A.2) than to maximize exchanger efficiency in the osmotic dilution case. Theoretical exchanger efficiency curves were plotted with the same terminal osmotic pressure difference, feed salinity, and recovery ratio as each pilot plant using Eq. 2.16. The parasitic electrical consumption of all

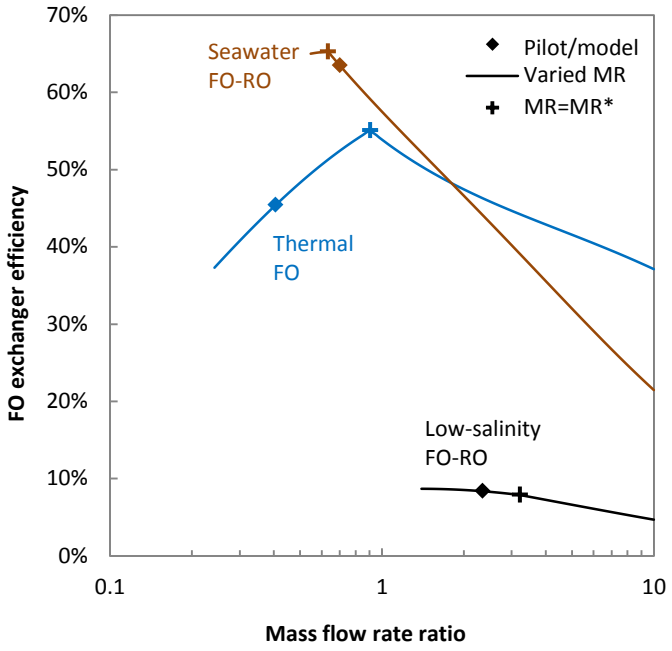

Figure 2-7: Potential improvements in the FO exchanger efficiency of pilot plants. Mass flow rate ratio is varied for the same terminal osmotic pressure difference, feed salinity, and recovery ratio as each pilot plant using data from [1, 3, 5]. The performance of each plant at its reported mass flow rate ratio as well as at the analytical optimum (MR^*) are also plotted.

FO exchangers was estimated based on a 2 bar hydraulic pressure drop in both feed and draw streams. The minimum mass flow rate ratios for the osmotic dilution and thermal FO pilots correspond to a saturated draw solution.[4] The minimum mass flow rate ratios for the low salinity FO-RO pilot and the Nicoll FO-RO model correspond to 7% NaCl draw because they use RO regeneration.

Figure 2-7 shows the potential of balancing to raise exchanger efficiency in existing systems. The exchanger efficiency varies with mass flow rate ratio (as well as minimum osmotic pressure difference, feed salinity, and recovery ratio, as in Eq. 2.16), reaching a maximum at MR^* (Eq. 2.18) in all cases except the low-salinity FO-RO pilot, where the low feed salinity (0.35%) leads to a hydraulic pressure drop comparable to the feed osmotic pressure, as discussed in Sec. 2.4.1. By choosing the optimal mass flow

[4]Properties of the ammonia-carbon dioxide draw solution in [3] were estimated using the extended UNIQUAC model for electrolyte solutions as in [55] with additional data from [56].

rate ratio, efficiency improvements of 3% in Nicoll's FO-RO model [5] to 21% in the thermal FO pilot [3] could be realized.

For systems with regeneration processes such as RO whose efficiency is relatively independent of feed salinity [2], Eq. 2.9 shows that the increases in exchanger efficiency due to balancing will be translated into proportional increases in system efficiency. However, the efficiency of thermal regeneration processes may vary more with draw stream salinity, and therefore such systems should be optimized by varying the mass flow rate ratio within a numerical model of the entire system. Either way, the efficiency gain attainable by balancing alone is small, and will not change the trends seen in the salinity-efficiency map (Fig. 2-2).

2.5 Chapter conclusion

FO brine concentration processes were compared to established technologies to demonstrate that improvements in exergetic efficiency are needed for FO to become more energetically competitive. We showed that FO system exergetic efficiency is approximately the product of FO exchanger efficiency, which we defined in Eq. 2.7, and regenerator efficiency. This expression demonstrates that the exchanger and regenerator efficiencies are equally important, and improvements to either will affect the system efficiency proportionally.

The mass flow rate ratio was identified as a crucial parameter in high-efficiency FO system design, and we showed that thermodynamically balancing systems by optimizing the mass flow rate ratio leads to modest improvements in efficiency. We offered a simple expression (Eq. 2.18) for the optimal mass flow rate ratio that maximizes the FO exchanger efficiency for high salinity FO at a fixed terminal osmotic pressure difference. In the pilot systems considered, balancing by flow rate optimization would improve the exergetic efficiency of FO brine concentration by around 3–21%. In FO desalination system design, the balancing method is best applied by numerically optimizing the mass flow rate ratio for maximum system efficiency at a fixed FO exchanger size, using the analytical expression to provide an initial estimate, and

setting the mass flow rates and concentrated draw salinity of the FO system according to the results of the optimization.

Chapter 3

Quantifying osmotic membrane fouling to enable comparisons across diverse processes

This chapter is based on a paper by Tow and Lienhard [14].

3.1 Introduction

Although osmotic separation processes such as reverse osmosis (RO) are the most energy-efficient water treatment technologies for a wide range of water compositions [2, 20, 54], they are plagued by membrane fouling. A recent review by She et al. [27] discussed a range of fouling types, flux decline models, and mitigation methods. To understand the factors that govern membrane fouling and develop mitigation strategies, many studies have compared different processes, coatings, etc. using flux decline as a metric. Flux decline (the change in flux due to fouling divided by the initial flux) quantifies the effect of fouling on the productivity of a given process, but does not give any insight into the accumulation of foulant itself. Therefore, when studies compare diverse processes such as RO and forward osmosis (FO) using flux decline alone, differences in the response of the processes to foulant accumulation preclude meaningful comparisons. In order to translate experimental results into

fundamental understanding of membrane fouling, a deposit-centric, in situ fouling quantification method is needed.

In this chapter, a method is outlined for quantifying porous foulant accumulation on semipermeable membranes in terms of two parameters that capture both osmotic and hydraulic causes of flux decline. FO and RO models are developed, although other osmotic processes (assisted forward osmosis, etc.) could be treated similarly if the active layer is facing the feed. The type of fouling considered is porous fouling, which could consist of biofouling, organic fouling, or inorganic fouling so long as no crystals pierce the membrane's active layer and the active area is not blocked by oil deposition or crystal growth. Here, alginate is used as a model porous foulant because of its gelation in the presence of calcium ions and the strong dependence of its material properties on its ionic environment. The proposed method is used to quantify fouling in experimental RO and FO.

3.1.1 Limitations of flux decline

Many fouling studies are concerned with comparisons, such as the relative fouling propensity of FO vs. RO [9], pressurized vs. unpressurized FO [11, 12], or new membrane coatings vs. commercial membranes [57]. Although flux decline comparisons often keep initial flux constant because of the dependence of fouling rate on flux [29], differences in membrane properties and solution composition can lead to differences in flux decline between experiments even if the foulant layers are identical in size and structure. Flux decline effectively measures the response of the system to fouling; however, it can only hint at the quantity of accumulated foulant.

As an example, Lee et al. [9] compare fouling with colloidal silica and various dissolved organics in FO and RO, and find that FO has more severe flux decline in most cases. However, they claim that the faster flux decline in FO is primarily due to the increase in osmotic pressure near the membrane that is enhanced by reverse salt diffusion from the draw solution to the feed solution. Because of the reverse salt diffusion in FO, no conclusion could be drawn about the relative accumulation rates of foulants in FO and RO by observing flux decline alone. Rather than continue to

make comparisons in terms of flux decline and speculate on how those results relate to fouling propensity, this chapter provides a framework using flux measurements to quantify the amount of foulant accumulated as a function of time.

3.1.2 Existing methods of quantifying fouling

Some methods have been developed based on the hydraulic resistance to flow through the porous foulant cake. Hydraulic resistance is generally the main cause of flux decline for membranes with large pores (e.g., ultrafiltration), which do not reject small dissolved species, but this assumption is sometimes extended to salt-rejecting membranes such as RO. For example, Farias et al. [58] quantify fouling with a "membrane fouling index" based on a (hydraulic) resistance in series model presented by Nguyen et al. [59] for ultrafiltration membranes. However, methods such as this neglect to account for another important factor in flux decline of semipermeable membranes: the concentration of dissolved constituents within the cake layer and the resulting increase in osmotic pressure at the membrane.

For salt-rejecting membranes such as FO and RO, this concentrative mechanism of flux decline has been described by Hoek and Elimelech [60]: When a porous cake layer forms on a salt-rejecting membrane, diffusion of salt away from the membrane must counter the flux of salts toward the membrane due to convection with the feed. In this way, the cake layer causes an increase in the osmotic pressure at the membrane active layer, reducing the driving force for water flux according to the solution–diffusion model [61]. As with more porous membranes, there is also some hydraulic resistance to permeation of water through the foulant cake layer, which is accounted for in the Hoek and Elimelech model [60]. This model quantifies foulant accumulation in terms of the osmotic pressure differential across the cake, which they term "cake enhanced osmotic pressure" (CEOP). The CEOP model is useful when making comparisons at a fixed salinity within a fixed process (e.g., seawater RO). However, changes in salinity will affect the osmotic pressure differential for a given foulant cake, so it cannot be used to compare fouling at different salinities (between wastewater RO and seawater RO, for example).

The path toward a universal model has been laid out by these existing studies, which we build on using a layered transport model that accounts for both hydraulic and concentrative causes of flux decline in FO and RO. We take an approach similar to Nagy's model for flux in unfouled FO membranes [62], but incorporate the presence of a porous foulant layer with gradients in both hydraulic and osmotic pressure. We reduce the problem of quantification to two parameters: cake structural parameter (analogous to the support layer structural parameter in FO membranes) and pore hydraulic diameter. Using this model, fouling tests spanning a range of membranes, processes, and feed compositions can be compared directly to improve fundamental understanding of fouling processes. We then experimentally compare accumulation rates of alginate gel fouling across two dimensions that take advantage of the comparison capabilities of the new quantification method: (1) the effect of feed salinity in RO and (2) the difference between FO and RO with the same feed solution.

3.2 Layered transport model for fouled RO and FO

Modeling the effects of fouling in osmotic separation processes is challenging due to widely-ranging length scales, complex geometries, and spatially-varying material properties. As a simplification, we model quasi-steady, one-dimensional transport of salt and water perpendicular to the membrane in both FO and RO. Real membranes and foulant layers may have indistinct and/or rough interfaces, but this model divides the flow path into distinct, planar layers, each with its own transport model. In many ways, the model developed here parallels the model of Nagy [62] for FO without fouling. Like Nagy, we model transport of a single salt in one dimension through several layers with their own appropriate models, but we add a layer of porous foulant on the feed-facing side of the membrane and also account for dispersion in the FO membrane support layer.

Figure 3-1 depicts the layers considered and their respective transport models.

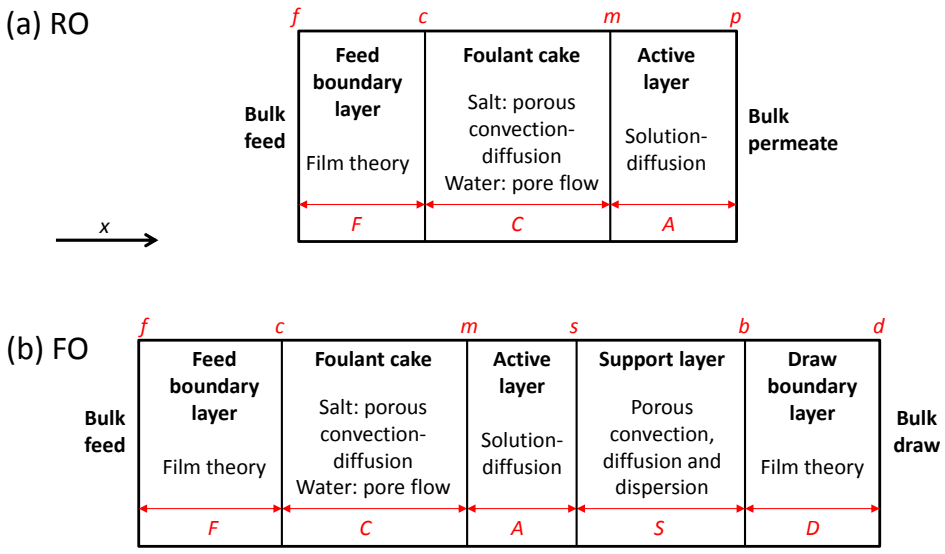

Figure 3-1: Summary of layers and their respective models for (a) RO and (b) FO, with water flow from left to right. Boundary conditions (bulk feed, draw and permeate), the positive x direction for all modeling, and subscripts (in red) used to denote layers and interfaces are labeled.

Feed and draw/permeate concentrations in the bulk flow are treated as boundary conditions. Because salt and water flows are assumed to be one-dimensional and quasi-steady, the salt flux and water flux can be treated as uniform along the direction of flow.

There are several limitations of the model developed herein. Pore blocking (described in [27]) and active layer damage are not modelled. The PRO orientation (active layer facing the draw) and its unique fouling mechanisms (e.g., suction-induced membrane dryout [13]) are not considered. The model can only be applied to foulants of known pore size or those with relatively large pores (over approximately 20 nm in diameter). Finally, predicting the deposition rate of foulant material is outside the scope of this chapter; rather, the model can be used to quantify foulant deposition based on experimentally measured water flux for foulant layers with sufficiently large pores.

In this section, we first address salt and water transport modeling in the foulant cake layer, which is relevant to both FO and RO. We then describe transport through the remaining layers in FO, utilizing the approach of Nagy [62], and develop a sim-

ilar model for fouled RO. Finally, we suggest a method for solving these systems of equations.

3.2.1 Cake structural parameter

Concentration polarization within the foulant cake layer is a major cause of flux decline for salt-rejecting membranes [60]. The tight pore structure of foulant cakes largely limits flow to the direction perpendicular to the membrane because that path through the cake layer is shortest. As long as the pores in the foulant layer are large enough to permit the passage of dissolved salts, salt is swept into the foulant layer by convection with the water being transported to the membrane. In one-dimensional, quasi-steady operation, the salt flux must be equal everywhere along the axis perpendicular to the membrane; however, RO and FO membranes generally exhibit high salt rejection, so the net salt flux is much less than the convective flux toward the membrane. To counter convection, salt diffuses away from the membrane down a concentration gradient. This concentration gradient is the cause of CEOP [60], which in turn causes flux decline due to the increased osmotic pressure at the membrane.

Both convection and diffusion occur through the porous foulant material, which hinders transport by both processes. Neglecting dispersion due to convection through the porous foulant (an assumption justified in Sec. 3.2.3), the pores can be treated as having an effective length that is greater than the cake thickness, δ_C, by a factor of the cake tortuosity, τ_C, and an area for diffusion that is reduced by a factor of the foulant porosity, ϵ_C. The diffusive flux is thus modified by a factor of ϵ_C/τ_C from the unhindered case, and the effective diffusion distance can be described as $L = \delta_C\tau_C/\epsilon_C$. Gels like alginate can be treated as porous materials because they have a continuous solid phase, with the rest of the volume filled by liquid.

In the support layer of an FO membrane, a similar effective length for diffusion that controls internal concentration polarization (ICP) is called the structural parameter. Therefore, we define the effective thickness of the foulant cake layer as the *cake* structural parameter, S_C:

$$S_C \equiv \frac{\delta_C \tau_C}{\epsilon_C}. \tag{3.1}$$

Having defined a cake structural parameter, salt transport by convection and diffusion through the foulant layer can be modelled the same way as it is in the support layer in FO by Nagy [62]. The cake layer salt transport equation is given in Sec. 3.2.3.

3.2.2 Cake hydraulic resistance

Hydraulic resistance to water flow through the cake also contributes to flux decline by reducing the pressure at the feed side of the membrane. Permeation of water through the cake occurs across a pressure drop[1] that can be estimated using a correlation appropriate for the structure of the porous material. Hoek and Elimelech [60] give a correlation appropriate for an agglomeration of spherical particles; however, we use a capillary model that is more appropriate for a highly hydrated gel such as alginate [63], which is used as a model foulant in our experiments.

In the capillary model, the porous foulant is treated as a bundle of tubes whose pressure drop is prescribed by the Hagen-Poiseuille equation, Eq. 3.2:

$$\Delta P = f_d \frac{L}{D_{h,C}} \frac{\rho v_C^2}{2}, \tag{3.2}$$

where ΔP is the pressure drop through the bundle, f_d is the Darcy friction factor, L is the effective length, $D_{h,C}$ is the hydraulic diameter of pores in the cake, ρ is the fluid density, and v_C is the average velocity through the bundle. For pores with diameters on the order of nanometers (true of alginate gels [64], and likely true of most foulant cakes because particles over 0.45 μm in diameter generally do not accumulate on the membrane [26], and pores are unlikely to be larger than the particle size), flow through the porous media is laminar. The friction factor can be estimated by the

[1]For salt-rejecting membranes, water flow through the cake is also driven by diffusion, but for the low salt mole fractions typical of desalination feeds, the ratio of diffusive to convective water transport is negligible.

correlation for laminar flow through round tubes,

$$f_d = \frac{64}{\mathrm{Re}_{D_{h,C}}} = \frac{64\mu}{\rho v_C D_{h,C}}, \tag{3.3}$$

where $\mathrm{Re}_{D_{h,C}}$ is the Reynolds number. Because cakes are not really bundles of round tubes, Eq. 3.3 is a rough approximation for friction factor. Additionally, we expect a range of pore sizes within any foulant cake. However, if $D_{h,C}$ is treated as an *effective* hydraulic diameter and fit from experimental data using the capillary model (as we do in Appendix B.1.1), this expression can be used.

The velocity of flow through the pores, v_C, is inversely related to the porosity, ϵ_C, as $v_C = J_w/\epsilon_C$ because of the reduced flow area. The length of flow, L, is greater than the foulant thickness, δ_C, by a factor of the tortuosity, τ_C: $L = \tau_C \delta_C$. By substituting these and Eqs. 3.1 and 3.3 into Eq. 3.2, the pressure drop between the feed and the membrane can be related to the structural parameter, pore hydraulic diameter, and water flux:

$$P_f - P_m = \frac{32\mu S_C J_w}{D_{h,C}^2}. \tag{3.4}$$

3.2.3 FO model

In this section, we present transport equations for salt and water through the remaining layers of the fouled FO membrane. The type of FO modelled in this study transports water from a feed solution into a more concentrated draw solution, which would then typically be regenerated by another separation process [54]. The distance coordinate x is defined as zero at the feed-facing edge of the membrane active layer and positive in the direction of water flow in typical FO and RO operation, i.e., from feed to draw or feed to permeate (direction shown in Fig. 3-1). Both salt and water fluxes are defined as positive in the positive x direction; as a result, salt flux in FO tends to be negative.

Using stagnant film theory, Nagy [62] models salt transport through both feed and draw boundary layers in FO with the 1-D equation for mass transport by convection

and diffusion:

$$J_s = J_w C - D\frac{\partial C}{\partial x}. \tag{3.5}$$

J_s is the salt (molar) flux in the x direction in units of [mol/m^2-s], C is the salt concentration in [mol/m^3], and D is the diffusion coefficient of salt in water. The concentration differences that drive salt diffusion through the boundary layers are often called external concentration polarization, or ECP.

Incorporating a mass transfer coefficient and assuming quasi-steady flow and conserving species (i.e., prescribing constant, spatially uniform J_s and J_w), Nagy [62] finds the following equations for salt transport in the feed and draw mass transfer boundary layers in FO:

$$J_s = -J_w \frac{C_c - C_f \exp(J_w/k_F)}{\exp(J_w/k_F) - 1}, \tag{3.6}$$

where C_c is the salt concentration at the outer edge of the foulant cake where it contacts the feed boundary layer. C_f is the concentration of the feed solution and k_F is the mass transfer coefficient of the feed flow, and:

$$J_s = -J_w \frac{C_d - C_b \exp(J_w/k_D)}{\exp(J_w/k_D) - 1}, \tag{3.7}$$

where k_D is the draw flow mass transfer coefficient, C_d is the bulk draw concentration, and C_b is the concentration at the draw side of the membrane support layer.

In the active layers of FO or RO membranes, the solution–diffusion model (see Wijmans and Baker [61]) describes the flow of both water and salt. In essence, the solution–diffusion model dictates that both species dissolve into the membrane and diffuse down their chemical potential gradient through a resistance that is characteristic of the membrane active layer. FO water flux depends on both the hydraulic and osmotic pressures according to Eq. 3.8 [61], which assumes an atmospheric pressure draw:

$$J_w = A|_{C_m}[P_m - (\pi|_{C_m} - \pi|_{C_s})], \tag{3.8}$$

where A is the water permeability of the membrane active layer (see Appendix B.2.1

for a discussion of the concentration-dependence of A), C is the salt concentration, P and π are hydraulic (gauge) and osmotic pressures, and subscripts m and s refer to the feed-facing and draw-facing sides of the active layer, respectively. Typically, the pressure in FO is close to atmospheric on both sides, but fouling may reduce the pressure at the membrane relative to that of the bulk feed. The pressure drop for convection of water through the porous structure of the support layer is assumed to be negligible, so the pressure behind the active layer is equated in Eq. 3.8 to the (assumed atmospheric) pressure of the bulk draw.

Salt flux (positive defined as into the draw) is given by the solution–diffusion model [61] as:

$$J_s = -B(C_s - C_m), \tag{3.9}$$

where B is the salt permeation coefficient of the active layer. To be precise, Eqs. 3.8 and 3.9 are a simplified form of the solution–diffusion model that applies when the driving force across the active layer is smaller than about 100 bar, as it would be in a typical desalination system, due to the linearization mentioned above [61]. Even when a large osmotic pressure gradient is applied to an FO membrane, the osmotic pressure difference across the active layer tends to be dwarfed by the one across the support layer (see Sec. 3.4.1).

Nagy [62] gives the following equation for salt flux due to convection and diffusion through the porous support layer:

$$J_s = -J_w \frac{C_b - C_s \exp(J_w S_S / D_S)}{\exp(J_w S_S / D_S) - 1}, \tag{3.10}$$

where S_S is the support layer sturctural parameter,

$$S_S \equiv \frac{\delta_S \tau_S}{\epsilon_S}. \tag{3.11}$$

However, based on our measurements of unfouled FO membrane flux (see Appendix B.1.2 and Fig. B-2), it would appear that, at higher water fluxes, dispersion is an important mechanism of salt transport in the support layer of the FO membrane

that has been neglected in prior modeling. Dispersion occurs in convection–diffusion processes through relatively large pores at relatively high flow rates [65], such as in groundwater flows. If dispersion is included, the support layer salt transport equation becomes Eq. 3.12:

$$J_s = -J_w \frac{C_b - C_s \exp(J_w S_S / D_{S,\text{eff}})}{\exp(J_w S_S / D_{S,\text{eff}}) - 1}, \tag{3.12}$$

where $D_{S,\text{eff}}$ is the effective diffusion coefficient, which encompasses the effect of dispersion.

When dispersion is accounted for, the effective diffusion coefficient increases with increasing flux. Perkins and Johnston [65] give the following equation for the apparent diffusion coefficient D_a (which we will relate to $D_{S,\text{eff}}$) for longitudinal dispersion in random packs of spheres:

$$D_a = D_a|_{v=0} + 0.5\sigma d_p v, \tag{3.13}$$

where $D_a|_{v=0}$ is the apparent diffusion coefficient in the porous medium in the absence of convection-driven dispersion, σ is the inhomogeneity factor of the porous medium (σ=3.5 would be typical for a random pack of spheres [65]), d_p is the diameter of particles in the pack, and v is an average flow velocity inside the pores. Although the support layer is not really a random pack of spheres, the dispersivity can be fit from experimental data, as we do in Appendix B.1.2.

To translate the apparent diffusivity (Eq. 3.13) into the effective diffusion coefficient in Eq. 3.12, we first note that the effective diffusion coefficient in the support layer is $D_{S,\text{eff}} = (\tau_S/\epsilon_S)D_a$ and that the effective diffusion coefficient without dispersion is $D_{S,\text{eff}}|_{J_w=0} \equiv D = (\tau_S/\epsilon_S)D_a|_{v=0}$. If we approximate the flow speed inside the porous support layer as $v \approx J_w \tau_S/\epsilon_S$, the resulting effective diffusion coefficient for the support layer can be expressed as:

$$D_{S,\text{eff}} = D_S + \alpha J_w, \tag{3.14}$$

where

$$\alpha \approx 0.5\sigma d_p \left(\frac{\tau_S}{\epsilon_S}\right)^2, \tag{3.15}$$

and d_p is the equivalent particle diameter of the porous support layer. Short of numerically simulating dispersion based on measured support layer microstructure, accurate calculation of α may be all but impossible. However, dispersivity can be fit from flux measured in foulant-free FO experiments and Eq. 3.15 can be used to make sure the fitted dispersivity is within a reasonable range. As described in Appendix B.1.2, the value of dispersivity fit from our foulant-free FO flux measurements across a wide range of feed and draw concentrations was $\alpha = 1.65 \times 10^{-4}$ m, which corresponds to $\sigma d_p \approx 6.5$ μm for the product of support layer pore diameter and inhomogeneity factor. SEM and optical micrographs of the same CTA FO membrane used in the present experiments show support layer pore diameters on the order of 10 μm [66], so we would expect to see some enhancement of diffusion.

Salt transport through the porous cake layer occurs through convection and diffusion, so we utilize the definition of the cake structural parameter (Eq. 3.1) to create a salt flux equation analogous to Eq. 3.12, but for the foulant cake layer:

$$J_s = -J_w \frac{C_m - C_c \exp(J_w S_C / D_C)}{\exp(J_w S_C / D_C) - 1}. \tag{3.16}$$

Here, D_C is the diffusion coefficient at a representative cake layer concentration without dispersion. Dispersion is neglected in modeling salt transport through the cake layer because, as Eq. 3.15 shows, dispersivity is proportional to pore diameter, and the pore diameter of the alginate gels considered in the experimental portion of this study have pore diameters on the order of 10 nm (see Fig. B-1). The ratio τ_S/ϵ_S is also small relative to the support layer. At the fluxes considered in this study (and common in membrane desalination processes), the increase in effective diffusion coefficient due to dispersion through the alginate gel layer should be negligible. However, for other foulant cakes with lower porosity and larger pore diameter, the possibility of dispersion should be evaluated using Eqs. 3.14 and 3.15.

If the concentration of the feed and draw streams are known, nine unknown variables remain: C_c, C_m, C_s, C_b, J_w, J_s, P_m, and the foulant parameters $D_{h,C}$ and S_C. So far we have presented just seven equations: Eqs. 3.6, 3.7, 3.9, 3.12, and 3.16 for

salt transport and Eqs. 3.4 and 3.8 for water. When the pore size of the foulant cake, $D_{h,C}$ is known, the water and salt fluxes can be predicted for a given cake stuctural parameter, S_C, or S_C can be calculated based on measured water flux. A protocol for estimating the foulant pore diameter is given in Appendix B.1.1, and results are provided for alginate. Alternatively, if the pore size is large enough, the hydraulic pressure drop through the foulant cake can be neglected, and the equation $P_m = P_f$ added.

A method for solving this system of equations and the necessary correlations for mass transfer coefficients and osmotic pressure are laid out in Sec. 3.2.5.

3.2.4 RO model

The model for transport through the layers of a fouled RO membrane closely parallels the FO model.

The equation for salt transport in the RO feed boundary layer is identical to the one for FO (Eq. 3.6). However, unlike FO, concentration polarization in and behind the support layer in RO can be neglected. Although permeate flowing along the permeate channel may have a different concentration than the permeate coming through the membrane in modules with significant recovery, the high salt rejection of commercial RO membranes leads to a very low permeate salinity and thus negligible concentration polarization on the permeate side.

Equations for salt and water flux through the cake layer in RO are identical to those for FO (Eqs. 3.4 and 3.16).

Salt and water flux through the membrane (Eqs. 3.17 and 3.18) are again governed by the solution–diffusion model [61], but the boundary conditions on the back side are the permeate pressure (assumed to be atmospheric) and concentration:

$$J_s = B(C_m - C_p), \tag{3.17}$$

and

$$J_w = A|_{C_m}[P_m - (\pi|_{C_m} - \pi|_{C_p})], \tag{3.18}$$

where the subscript p refers to the permeate stream. As in FO, the water permeability as a function of salt concentration can be calculated from Eq. B.5. Rather than specifying a permeate salinity, as we do for the draw in FO, permeate salinity is explicitly calculated from the salt and water fluxes:

$$C_p = \frac{J_s}{J_w}. \tag{3.19}$$

When feed concentration and pressure are known, C_c, C_m, C_p, J_w, J_s, P_m, $D_{h,C}$, and S_C make up eight unknowns. With just six equations (3.4, 3.6, and 3.16–3.19), it is insufficient to specify just the flux or structural parameter. As with FO, a known relationship between foulant pore diameter and local conditions can add one equation. Alternatively, in RO, C_p can be measured.

3.2.5 Solution method

In the model of Nagy [62] for unfouled FO, the multiple equations for J_s are combined into one through a mass transfer resistance in series model, but the complexity of this equation increases with the number of layers considered by the model. The complexity is further increased by the current model's consideration of the hydraulic resistance of the foulant layer and dispersive salt transport (i.e., effective diffusion coefficient dependence on flux) in the support layer. We have also relaxed the assumption of ideal solution behavior to enable the present model to be used with highly saturated FO draw solutions. Some other models combine layers into an algebraic equation by approximating the salt flux as zero everywhere [27], but these models do not account for salt back-diffusion in FO or its effect on foulants whose properties depend on solution ionic composition. To solve these systems of equations, we combine the equations for salt flux into one matrix equation and the equations for water flux into one algebraic equation. These two equations must then be solved simultaneously (we use MATLAB's *fsolve*). The matrix equations for RO and FO with and without fouling are provided in Appendix B.2.3 for convenience.

To apply the model, mass transfer coefficient correlations are needed for the feed

and draw boundary layers. In evaluating the model, we use mass transfer coefficients measured experimentally with the apparatus configured for RO as detailed in Appendix B.1.3. As the foulant cake grows large and begins to encroach on the channel, the mass transfer coefficient may change due to the increasing cross-flow velocity (assuming fixed feed flow rate) as well as changes to the flow pattern when the cake contacts the feed spacer. Future work may address these complexities; for now, the cake layer is assumed to be thin compared to the feed channel and the mass transfer coefficients are assumed to be constant.

Solution properties are also needed to evaluate the model. We use Pitzer's model for electrolyte solutions (see, e.g., [67, 68, 69]) to calculate sodium chloride solution osmotic pressure and density as a function of concentration. Due to the low compressibility of water [70], the high pressures utilized in RO systems are not expected to significantly affect the physical properties of the solutions. Diffusion coefficients are taken from data in [71] (see Appendix B.2.2).

Membrane properties can be fit from experimental data or estimated from published test results. In Appendix B.1.2, we demonstrate how the salt permeation coefficients were measured experimentally and calculated from the test results supplied with the membranes and how the FO membrane's support layer structural parameter and dispersivity were fit. In this study, the membrane properties are assumed to vary between membrane samples and one property is fit for each sample from the flux measured just after the foulant was added, and before any significant cake layer could form. In RO, water permeability is fit for each membrane. In FO, we fit for the dispersivity because of its strong dependence on support layer properties (Eq. 3.15).

Finally, in order to relate foulant accumulation to flux decline, pore diameter must be evaluated. We show in Appendix B.1.1 that for a sufficiently high ratio of sodium to calcium ion concentration, the alginate used as a model porous foulant in this study has sufficiently large pores that the hydraulic pressure drop across the cake is small in comparison to the cake enhanced osmotic pressure. Based on pore size measurements at high sodium:calcium concentration ratios (see Appendix B.1.1), we use an estimated pore diameter of 20 nm to calculate cake structural parameter from

experimental flux measurements.

3.3 Experiment

RO and FO fouling experiments are performed to validate and test the proposed fouling quantification method. Transmembrane flux is recorded over time to monitor the evolution of the cake structural parameter in RO and FO due to fouling with feed solutions containing sodium alginate, calcium chloride, and sodium chloride. Flux is calculated from the rate of change in permeate or draw mass in RO and FO, respectively, while temperature, pressure, and cross flow velocity are fixed. Using this experiment and the layered transport model, we compare foulant accumulation as cake structural parameter between FO and RO and across a range of salinities (2–3.7% NaCl) in RO. Salt concentrations are chosen to be within the range where hydraulic pressure drop through the foulant cake (Sec. 3.2.2) is small compared to the CEOP. Initial flux is kept constant between different trials.

3.3.1 Apparatus

The experimental apparatus, which can be configured for RO or FO, is illustrated in Fig. 3-2.

In our custom-built membrane module, the feed channel is cut 1 mm deep to roughly approximate flow conditions in spiral-wound RO elements, and is equipped with a 0.79 mm-thick non-woven feed spacer (Sterlitech 31 mil diamond). The draw/permeate channel is also 1 mm deep and uses two 0.43 mm-thick non-woven feed spacers (Sterlitech 17 mil diamond) in FO operation; in RO operation, it is filled with five layers of permeate spacer mesh cut from a low-pressure RO module. The channels are 8 cm long and 3 cm wide, which is comparable to the channel area in previous controlled fouling studies [9, 72]. Three nested O-rings, which contact each side of the membrane and outside the membrane, rest in grooves designed to minimize membrane damage and provide sealing that ensures very good overall salt rejection (see Appendix B.1.2) for a membrane module of this size. Details of module design

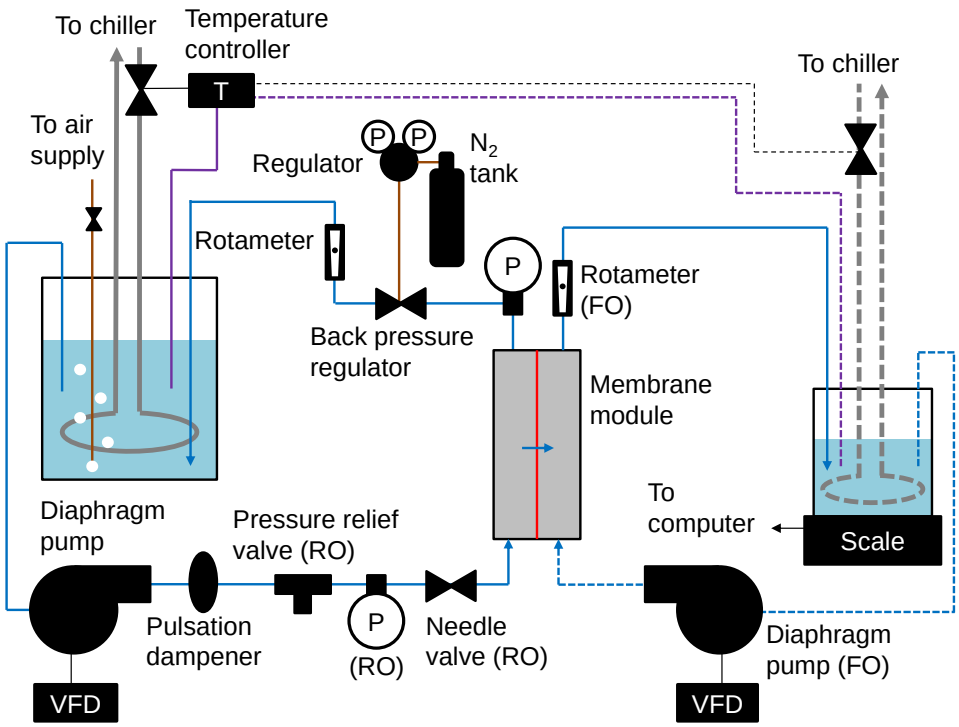

Figure 3-2: Schematic diagram of the experimental apparatus which can be operated in RO or FO. Some elements (labeled) are only used for RO or FO; dashed lines represent flows only present in FO operation. Purple lines represent thermocouples.

are provided in [13].

Flux in lmh (L/m^2-hr) is calculated from the change in permeate or draw mass during 15 minute intervals. Mass is recorded every second with an Ohaus Scout Pro digital scale of 6 kg capacity and 0.1 g repeatability.

Temperature is maintained at 20±1 °C by a temperature controller (Omega) and stainless steel cooling coils, which are supplied with chilled water and immersed in the feed and draw tanks. Volume displaced by the draw cooling coil, inlet, and outlet is accounted for in the data analysis. Diaphragm pumps (Hydracell) are driven with variable frequency drives (VFDs) to set the flow rate. A pulsation dampener steadies the flow rate on the feed side; in FO, the need to measure changes in draw volume precludes the use of a pulsation dampener, and the draw flow oscillates around a prescribed mean. Feed pressure is controlled with a back pressure regulator (Equilibar).

Rather than controlling draw and feed concentration, gradual variation is allowed

and accounted for in the feed and draw salinities input to the model, as we discuss in Appendix B.1.4. Conductivity is measured with a Hach conductivity meter, and sodium chloride concentration is interpolated from tabulated data in [73]. The feed is kept well-mixed by a slow stream of air bubbles, which also serve to improve thermal control of the feed by increasing the heat transfer coefficient on the cooling coil [74, 75]. The draw is not actively mixed, but the inlet to the draw pump is placed halfway up the draw tank so that if the tank becomes stratified, draw is taken from the middle of any salinity and temperature gradients.

The maximum system pressure[2] is 69 barg (1000 psig), allowing for testing of solutions comparable in osmotic pressure to seawater. Aside from diaphragms, all material in contact with high pressure fluid is 316 stainless steel for good corrosion resistance.

3.3.2 Membranes

For RO tests, high-rejection thin-film composite polyamide membranes (Dow FILMTEC SW30HR) are used. For the FO test, an asymmetric cellulose triacetate membrane (Hydration Technology Innovations CTA-ES) was used in FO mode (active layer facing the feed). Property characterization for both membranes is described in Appendix B.1.2. In contrast to a previous study that compared RO and FO fouling using the same FO membrane [9], the present study uses different membranes for primarily practical reasons: RO membranes are not effective in FO operation because of the high support layer structural parameter, while the chosen FO membranes, rated for just 0.69 bar (10 psi) of transmembrane pressure [76], are not designed to withstand the pressures typical of the RO process. In addition, membrane surface chemistry has a limited effect on foulant cake evolution beyond the adsorbed layer, as shown by Wu et al. [77].

[2]The pressure unit "barg" refers to bar *gauge*, or differential pressure with respect to atmospheric pressure; similarly, "psig" denotes psi gauge.

3.3.3 Model porous foulant

Sodium alginate, a polysaccharide composed of mannuronic and guluronic acids, is used as a model porous foulant because polysaccharides are an important component of RO membrane fouling in both wastewater and seawater applications [78] and because it exhibits similarities to the extracellular polymeric substances (EPS) that form a cake layer in biofouling [79]. As described in [80, 81], the polyguluronates in alginic acid complex with calcium and other multivalent ions [82], which are present in most water sources, causing dissolved alginate that concentrates near the membrane to form a cross-linked gel. The sodium alginate used here (Sigma-Aldrich) has a molecular weight rating of 80,000-120,000 g/mol.

The pore diameter of the alginate gel determines the hydraulic resistance to flow through the foulant cake and is a necessary parameter for computation of the cake layer structural parameter. Many studies have characterized alginate gel pore size, but the range of measurements is wide due to differences in the alginate molecules themselves (which vary in molecular weight, guluronate fraction, and monomer ordering), gelation method, solution ionic composition, and measurement method. For example, Boontheekul et al. [83] characterize an average pore diameter of alginate through thermoporometry, finding a pore diameter of 11.6 $\pm$0.4 nm for their high molecular weight (270,000 g/mol) alginate gel. Klein et al. [84] who found pore diameters of approximately 6.8-16.6 nm for three alginates through inverse steric exclusion chromatography. Imaging methods tend to identify larger pore sizes (likely due to the drying necessary), but three diffusion-based methods reviewed in [64] find pore sizes that are also in the 10 nm range. Shoichet et al. [85] find that a higher degree of cross-linking leads to smaller pores.

Unfortunately (for the aims of this study), permeation hydraulic resistance is related to the square of the hydraulic diameter, and small errors in estimation of the pore radius can lead to large errors in the calculated cake structural parameter when the hydraulic resistance is significant. Future work to characterize pore sizes in alginate formed in RO conditions will be important, but for the present study

we will focus on the range in which the hydraulic pressure drop through the cake is very small compared to CEOP (less than about 10%), so that uncertainties in pore diameter do not significantly influence our results. Appendix B.1.1 details how this range was bounded.

3.3.4 Fouling procedure

Membranes were soaked in 50% ethanol, 50% water solution for five minutes and then in DI water for at least 30 minutes before use. Membranes were installed in the apparatus with the spacers described in Sec. 3.3.1. Before any foulants were added, RO membranes were compacted and equilibrated with the feed solution for at least two hours or until flux stabilized. FO membranes were equilibrated for at least two hours with the feed solution and saturated NaCl draw solution (which had been partially degassed to prevent air accumulation in the draw loop). During this period, feed flow rate was maintained at 16.7 cm/s to discourage premature fouling. In FO, draw flow rate is maintained at 4.3 cm/s. In RO, after membrane compaction and equilibration, feed pressure was adjusted to achieve the desired transmembrane flux.

The fouling procedure was identical between RO and FO experiments aside from the membranes used (see Sec. 3.3.2) and the driving force for water permeation. To begin fouling, 0.13% sodium alginate solution (mixed 24 hours prior to ensure complete solvation) was added to the feed tank to reach a final concentration of 200 mg/L. After allowing the alginate to disperse in the air-mixed feed tank for a few minutes, concentrated calcium chloride solution was added to the feed to reach a concentration of 1 mM. The feed velocity was then reduced to 8.3 cm/s, except in the case of the comparison of FO and RO (Sec. 3.4.3), in which the feed velocity was reduced to 5.6 cm/s to accelerate fouling in both tests. Typically, a small, rapid drop in flux occurred just after the alginate and calcium were added and the feed velocity was reduced. We attribute this to increased concentration polarization in the feed channel due to decreased velocity and increased solution viscosity, and the initial flux used to fit permeability and calculate flux decline is chosen to be the flux just after the initial drop. Once fouling has been initiated, transmembrane flux is monitored

for ten hours at constant pressure, temperature, and cross-flow velocity.

3.4 Results and discussion

3.4.1 Model results: concentration and pressure profiles

In this section, we calculate concentration and pressure profiles in FO and RO to illustrate the effects of fouling in osmotic processes and help explain the experimental results that follow. Cases considered include high and low concentrations of sodium chloride with 1 mM calcium chloride to show different fouling regimes that depend on ionic composition in both FO and RO. (Appendix B.2.4 contains piecewise equations for concentration and pressure based on the layered model.)

At high sodium:calcium ratio, cake hydraulic resistance is negligible and the cake layer affects flux through CEOP. Figure 3-3 shows osmotic and hydraulic pressure profiles throughout the membrane and surrounding layers in FO and RO with a foulant accumulation of $S_C = 100$ μm (similar to experimental measurements in Secs. 3.4.2 and 3.4.3) and a feed solution of 3.5% wt. NaCl. The modelled FO draw solution was 24% wt. NaCl and RO feed pressure was 66 barg. Pore diameter was assumed to be 20 nm based on Fig. B-1. For the purpose of illustration only, τ_C/ϵ_C was assumed to be 1.1 to calculate cake thickness from structural parameter.

RO and FO processes differ greatly in their response to CEOP. In FO, pressure is close to atmospheric everywhere, and flux is driven by the osmotic pressure difference across the membrane active layer. However, as Fig. 3-3 shows, the driving osmotic pressure difference in FO is dwarfed by the difference across the support layer due to ICP. In contrast, the hydraulic–osmotic pressure difference across the active layer in RO is by far the largest of any layer in the system. When a certain CEOP develops in RO, the driving force for flow across the active layer is reduced by an equal amount (neglecting the small impact of feed ECP). In FO, a small flux reduction due to CEOP causes a significant reduction in the concentration difference across the support layer, so although the osmotic pressure on the feed side of the active layer increases, the

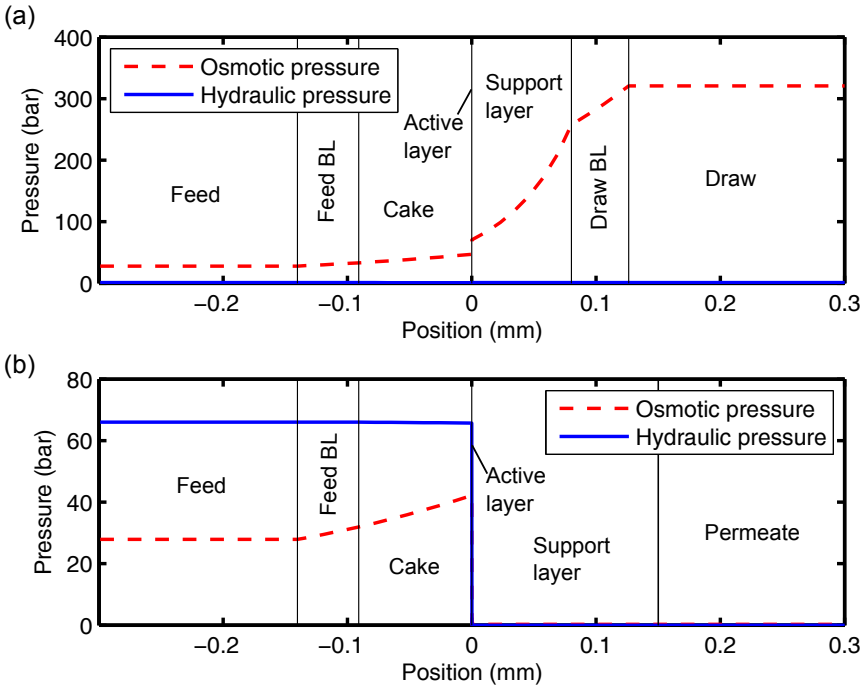

Figure 3-3: Modelled osmotic and absolute hydraulic pressure profiles for (a) FO and (b) RO with a foulant accumulation of $S_C = 100$ μm with 3.5% wt. NaCl feed. The label BL stands for "boundary layer."

draw side osmotic pressure increases almost as much. This phenomenon, referred to as "ICP self-compensation" [27], results in a smaller flux decrease in FO than in RO for the same cake layer. This important difference between these systems' response to fouling is also demonstrated through experimental results in Sec. 3.4.3.

When the sodium:calcium ratio is lower, the relative importance of hydraulic pressure drop and CEOP are reversed with respect to the high-sodium case. Figure 3-4 shows concentration and pressure profiles in FO and RO for a feed of 50 mM NaCl and 1 mM $CaCl_2$, for which a pore size of 6.6 nm was estimated from the results in Fig. B-1. FO draw solution was 24% wt. NaCl and RO feed pressure was 30 barg. The feed salinity (0.27% wt. NaCl) is so low that concentration polarization in the cake layer causes only a small increase in osmotic pressure at the membrane. However, the hydraulic pressure drops by several bars through the cake, reaching a minimum *absolute* pressure of −3.9 bar at the membrane.

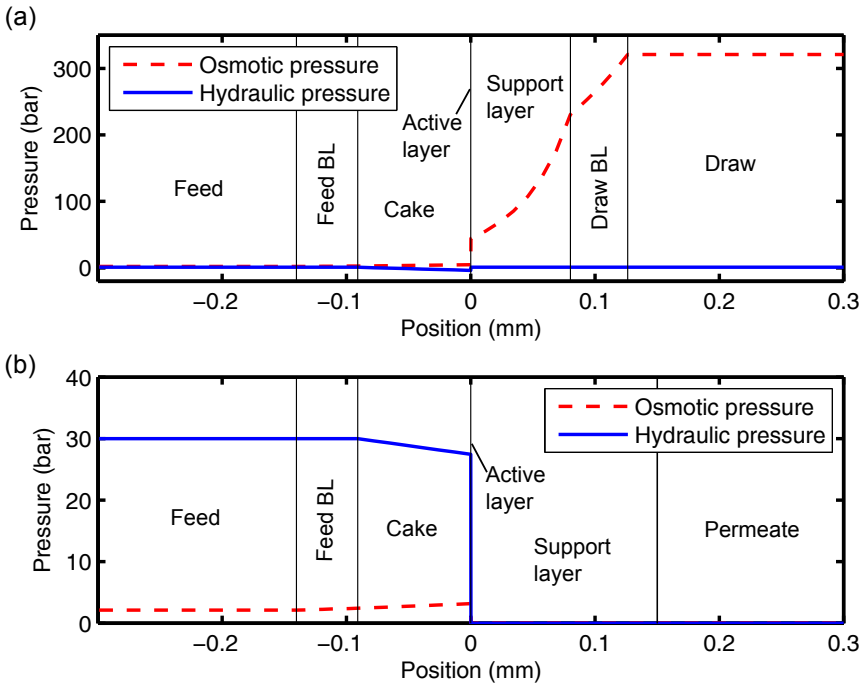

Figure 3-4: Modelled osmotic and absolute hydraulic pressure profiles for (a) FO and (b) RO with 50 mM NaCl feed and a foulant accumulation of $S_C = 100$ μm, showing negative absolute pressure within the cake in the FO case.

It is possible for negative absolute pressures to develop within the foulant layer because of the small pore size of alginate gels: in a matrix of a highly hydrophilic material like alginate, the interfacial pressure drop of a stable vapor bubble within a pore would scale with $4\gamma/D_{h,C}$, where γ is the surface tension of saline water at the local salinity and $D_{h,C}$ is the pore hydraulic diameter within the cake. For a pore size around 7 nm, the interfacial pressure difference between the inside and outside of a bubble would have to be on the order of 400 bar. In this way, the nano-scale pores of the alginate gel prevent cavitation within the foulant cake even when it is under some tension. Negative pressures have been shown to exist in tree xylem, another liquid-filled nanoporous material subjected to suction [86]. However, alginate fouling has been shown to cause nucleation in the larger, micro-scale pores of the feed-facing support layer of FO membranes in PRO orientation [13]. Large pores or hydrophobic materials in the foulant layer could theoretically act as nucleation sites regardless of

membrane orientation, although this has not to our knowledge been demonstrated.

3.4.2 Effect of feed salinity in RO

Part of the motivation for developing a universal method for fouling quantification is to be able to compare fouling rates in waters of differing ionic composition. In this section, we examine experimental fouling results for RO at NaCl concentrations of 2–3.7% wt. in terms of both flux decline and cake structural parameter. As in all trials, alginate concentration was 200 mg/L with 1 mM $CaCl_2$. Flux decline due to fouling was calculated from measured flux as $1 - J_w/J_{w,0}$, where $J_{w,0}$ is the foulant-free flux calculated from the layered model with no foulant layer (Eqs. B.8, B.9, B.12, and B.13). The 95% confidence intervals on the measurements in this section are ±3.6% for flux decline and ±13 μm for cake structural parameter in RO (±14 μm for the 2% wt. NaCl case). Uncertainty analysis is discussed in Appendix B.1.5. The RO model was validated against experimental data in Appendix B.1.1.

Trials were conducted as close as possible to the same initial flux, but the actual initial flux values were 22.8±0.4 lmh. To minimize the effects of slight deviations in initial flux on the fouling comparison, both flux decline and cake structural parameter are reported as a change from the values at the moment the flux reached 22.4 lmh. We have assumed that the period where the fouling accumulation rate is affected by the membrane surface properties is short compared to the time over which the initial flux is calculated (15 minutes). In the present experiments, the foulant layer thickness (on the order of tens or hundreds of micrometers) is much greater than the roughness of the membrane (order 100 nm in RO [87] or less in FO [66]) or the pore size of alginate (order 10 nm). Additionally, different membrane functional groups that affect initial alginate adsorption rate in RO have been shown not to significantly affect fouling in the long term [77]. Therefore, we focus on the stage of the foulant accumulation process where new foulant is attaching to existing foulant, not the membrane, and thus fouling trials beginning at different fluxes can be compared with respect to an arbitrary "initial" flux.

Figures 3-5 and 3-6 show the flux decline and foulant accumulation (as cake struc-

tural parameter) of three different feed solutions with NaCl concentrations of 2.0, 3.1, and 3.7% wt. at pressures of 36, 64.5, and (again) 64.5 barg, respectively. The flux decline results in Fig. 3-5 follow no clear trend with respect to salinity or pressure because of the variation in permeability (which itself affects flux decline) between membrane coupons. However, Fig. 3-6 is more illustrative: when flux measurements are used to compute cake structural parameter starting at the same flux, the evolution of the cake structural parameter over time is indistinguishable between the trials (with the exception of a brief excursion around 3 hours of the 3.1% NaCl trial, which we attribute to experimental error). By allowing the quantity of foulant to be extracted from flux decline measurements, the layered model shows that within the range of high sodium:calcium ratios considered here, solution ionic composition does not affect alginate gel accumulation rate. Morris et al. [80] find that the bound calcium fraction asymptotes to a minimum value beyond a certain sodium:calcium ratio, so it is possible that other properties asymptote similarly. However, the bound calcium fraction [80] and intermolecular adhesion forces [72] do vary within a lower range of sodium:calcium ratios, so some change in foulant accumulation rate might be expected with feeds of lower sodium or higher calcium concentration.

Notably, Fig. 3-6 shows no effect of pressure on foulant accumulation rate, even between pressures of 36 and 64.5 barg. This result contrasts with the findings of Xie et al. [12] on the effect of pressure in forward osmosis, in which confocal laser scanning microscopy was used to show that thicker foulant layers develop in FO at atmospheric pressure than in RO at just 12.5 barg on the same membrane. The apparent effect of pressure on fouling of FO membranes does not seem to extend to RO.

3.4.3 Comparison of RO and FO

Fouling rates in FO and RO are compared in this section in terms of flux decline and cake structural parameter to elucidate differences in the response to fouling and the rate of foulant accumulation. For these trials, the NaCl mass fraction was 3.5% and the cross-flow velocity was 5.6 cm/s. Alginate concentration was again 200 mg/L and $CaCl_2$ concentration was 1 mM. RO initial flux was 18.2 lmh (at 50 barg) and FO

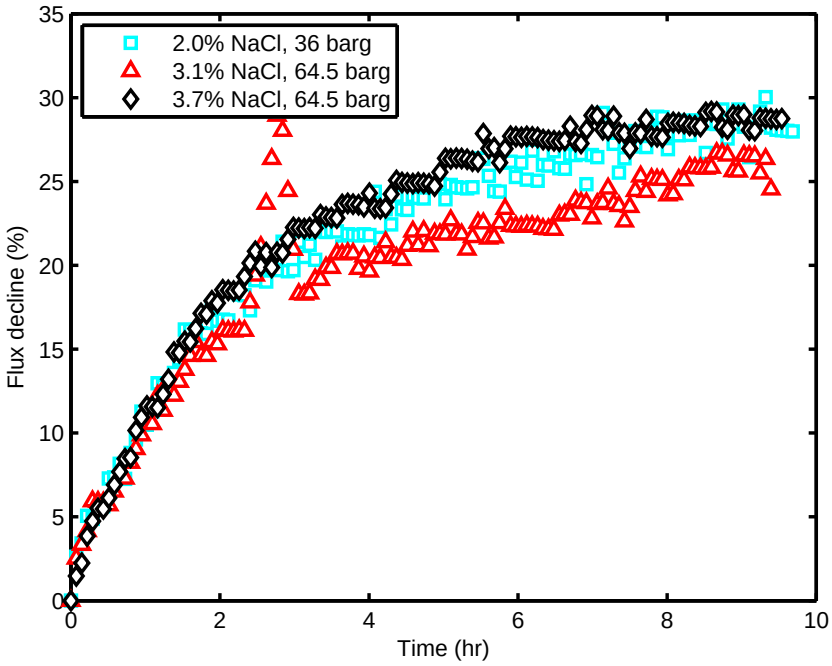

Figure 3-5: Comparison of flux decline profiles in RO with feeds of different salinity at different pressures. Permeability varied between coupons and pressures were chosen such that initial flux was 22.8 ± 0.4 lmh. To minimze the effect of initial flux on fouling rate, flux decline is given relative to the moment each run reached a flux of 22.4 lmh. Cross-flow velocity was fixed at 8.3 cm/s. Uncertainty in flux decline is ±3.6 percentage points.

initial flux was 18.0 lmh, but flux decline and S_C are given relative to the moment each run reached a flux of 18.0 lmh to eliminate the effect of initial flux on fouling rate. The 95% confidence intervals on RO flux decline and cake structural parameter measurements are again ±3.6% and ±13 μm, respectively. As discussed in Appendix B.1.5, the uncertainty in FO flux decline and cake structural parameter are ±5.7% and ±40 μm, respectively.

As shown in Fig. 3-7, flux decline is slower in FO than in RO under the same conditions. However, FO flux decline is expected to be slower because of the ICP self-compensation effect, as discussed in Sec. 3.4.1. As a result, it is not meaningful to draw a conclusion about the amount of fouling that occurred in FO vs. RO based on flux decline alone.

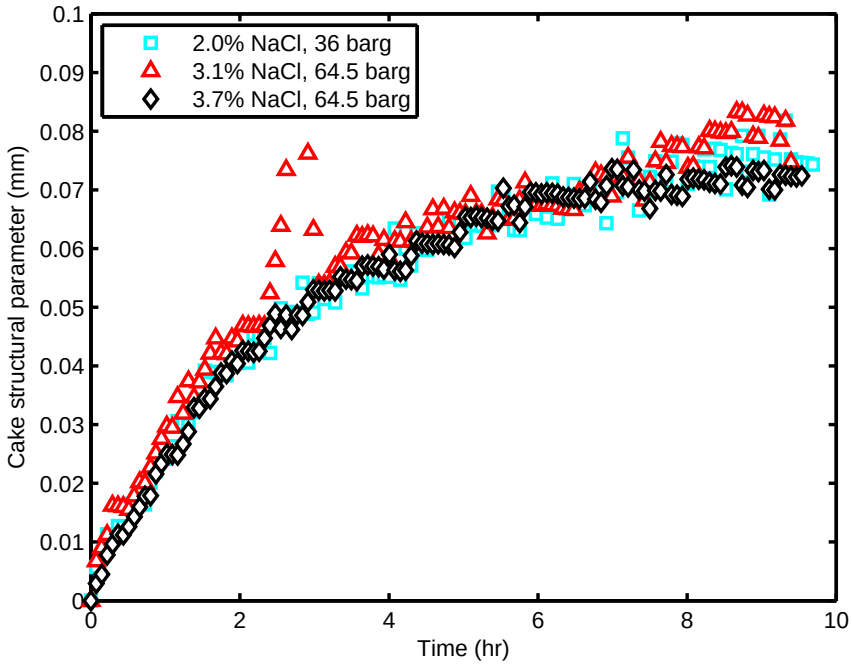

Figure 3-6: Comparison of calculated foulant accumulation in RO tests with feeds of different salinity on membrane coupons of varying permeability at different pressures, showing strong similarity. The cake structural parameter was calculated using the model presented here for the same tests that exhibited differences in flux decline in Fig. 3-5. To eliminate the effect of flux on fouling rate, cake structural parameter is given as a change relative to the moment each run reached a flux of 22.4 lmh. Uncertainty is ± 14 μm for 2% NaCl is and ± 13 μm for others.

When fouling accumulation is reported as cake structural parameter (Fig. 3-8), it is clear that despite its lower flux decline, the FO test resulted in a thicker foulant cake. Initially, the flux and accumulation rate are similar between FO and RO. However, as time progresses, flux drops more rapidly in RO than in FO (Fig. 3-7), as does the rate of foulant accumulation. This effect can be explained, at least to some extent, through an analogy to heat exchanger fouling made by Qureshi et al. [88], which suggests that RO fouling resistance follows an exponential approach to an asymptotic value at which the rate of deposition (proportional to flux) is equal to the rate of removal. According to that model, the total accumulation should be propotional to the time integral of flux minus asymptotic flux, and the process with a slower flux decline (FO, in this comparison) should have a larger cake structural parameter. Xie et al. [12]

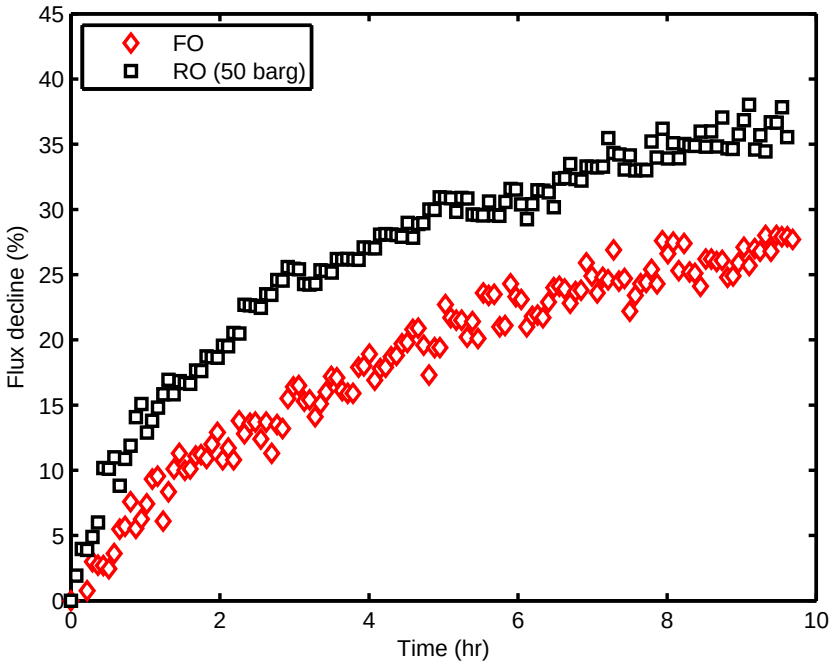

Figure 3-7: Comparison of flux decline profiles in RO and FO with 3.5% NaCl feed, showing greater flux decline in RO. RO initial flux was 18.2 lmh and FO initial flux was 18.0 lmh, but flux decline is given relative to the moment each run reached a flux of 18.0 lmh to eliminate the effect of initial flux on fouling rate. Feed cross-flow velocity was 8.3 cm/s in both trials. 95% confidence intervals are ±3.6 and ±5.7 percentage points in RO and FO, respectively.

found a similar result using confocal laser scanning microscopy on alginate gel layers harvested from fouled membranes: when operated under similar conditions with the same initial flux, thicker cake layers developed in FO than in RO; however, that study attributed the thinner layer in RO to compaction by hydraulic pressure. Future work should address whether the disparity in foulant accumulation is solely driven by the difference in flux decline rates of FO and RO systems, or whether other differences contribute as well.

As a means of validating the FO structural parameter model, the foulant cake formed during the FO trial in Fig. 3-8 was scraped off of the membrane immediately after the trial and weighed at 0.46 g. Assuming the density of the hydrogel is similar to water and the tortuosity and porosity are near 1, the final structural parameter

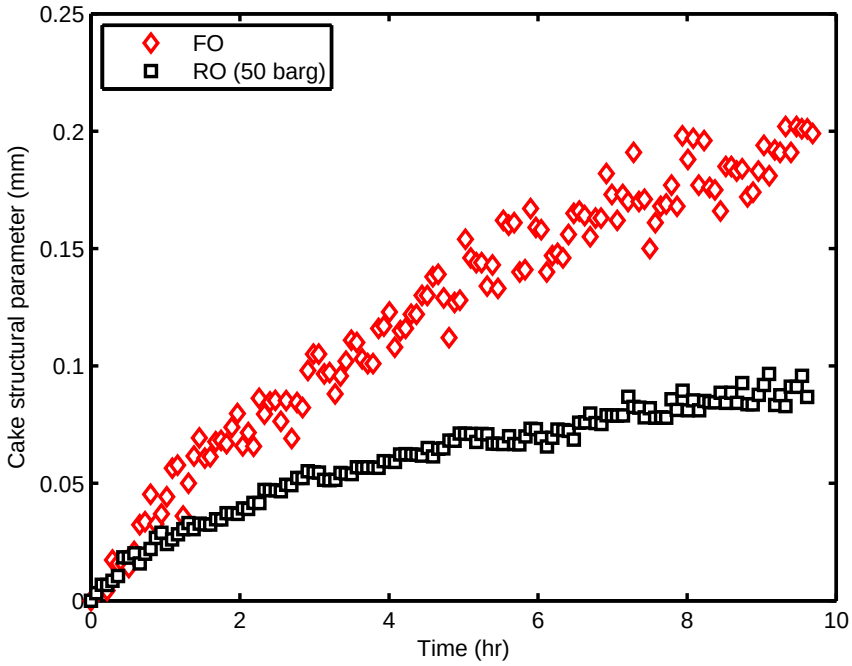

Figure 3-8: Comparison of calculated foulant accumulation in RO and FO, showing similar accumulation rates initially but greater accumulation over time in FO. To eliminate the effect of initial flux on initial fouling rate, cake structural parameter is given as a change relative to the moment each run reached a flux of 18.0 lmh. 95% confidence intervals are ± 13 μm for RO and ± 40 μm for FO.

can be estimated from the mass measurement as 190 μm, which is within 5% of the final structural parameter calculated from the flux decline (approximately 200 μm).

3.5 Conclusion

In this study, we developed a method of in situ fouling quantification that allows for comparisons of foulant accumulation between diverse processes with different membranes and feed solutions. Foulant accumulation is reduced to two variables (cake structural parameter and foulant pore hydraulic diameter) that can be calculated in RO or FO from experimental flux measurements using a layered model for salt and water transport which includes dispersion in the FO support layer. Notably, the model demonstrates that in FO, under certain conditions, absolute pressure can

reach negative values at the membrane. The model was experimentally validated for alginate gel fouling in a range of conditions where cake hydraulic resistance is negligible; future work to characterize the dependence of pore size on ionic environment for various foulants is needed to broaden the applicability of this quantification method.

The proposed method was used to analyze fouling experiments, leading to the following conclusions:

- In waters with a high sodium:calcium concentration ratio, alginate fouling accumulation rates in RO are independent of salinity and pressure.
- The slower flux decline of FO results in a higher rate foulant accumulation compared to RO.

We hope that this quantification method will accelerate progress in understanding fouling, especially as related to claimed differences in fouling propensity between FO and RO, and that it will lead to future capabilities in predictive modeling of fouling.

Chapter 4

Isolating the effect of pressure on alginate fouling in forward osmosis

This chapter is based on "Unpacking compaction: Effect of hydraulic pressure on alginate fouling" by Tow and Lienhard [89].

4.1 Introduction

Forward osmosis (FO) is often compared to reverse osmosis (RO) in terms of energy consumption and fouling propensity. After some debate [90, 91], RO has been found to be more energy-efficient [2, 20, 54, 92] but also more prone to irreversible fouling [9]. Although FO can foul significantly (see, e.g., [93]), many authors have postulated that the high feed hydraulic pressure used in RO exacerbates fouling. A number of recent reports, including Refs. [9, 10, 11, 12, 49, 94, 95, 96], attribute differences between RO and FO membrane fouling to foulant compaction by high hydraulic pressure. The most compelling evidence comes from studies that show a marked difference in the effectiveness of physical cleaning between identical membranes fouled under identical hydrodynamic conditions at the same initial flux in RO and FO [9, 10, 11, 12, 13]. According to the theory that foulant cake density increases with feed hydraulic pressure, the less-compact cake layer formed near atmospheric pressure in FO should be easier to remove. However, the effects of pressure have never been

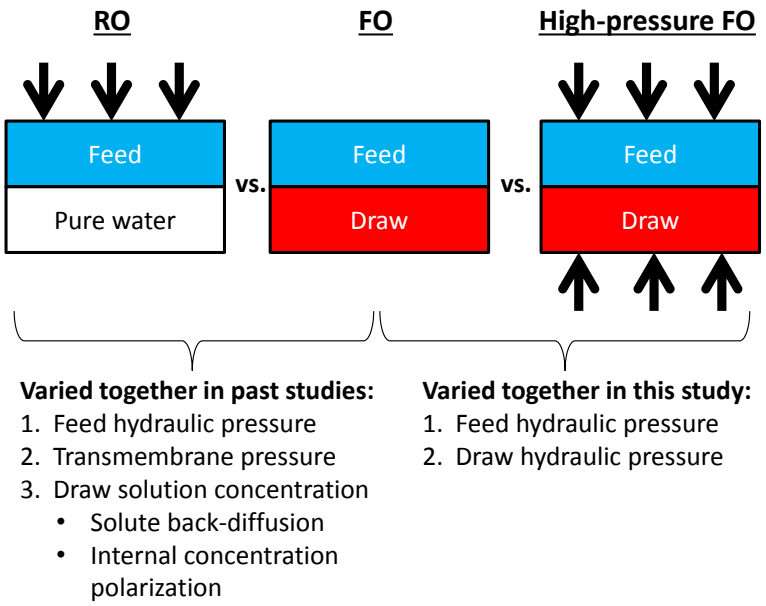

Figure 4-1: Methods of isolating the effect of pressure on osmotic membrane fouling taken by past studies (Refs. [9], [10], [11], and [12]) and the present study. All studies varied feed hydraulic pressure, but other variables that could potentially affect fouling were changed as well to avoid altering flux.

experimentally isolated from other differences between FO and RO.

In this study, we seek to experimentally validate or invalidate the theory that high feed pressure compacts foulants. We review previous studies of the effect of pressure on cleaning effectiveness in FO and RO and model the hypothetical effects of compaction on flux decline. As discussed further in Sec. 4.2, foulant compression is related only to feed hydraulic pressure and the pressure drop through the foulant layer and is not affected by the hydraulic pressure of the draw or permeate. Therefore, we experimentally isolate hydraulic pressure as an independent variable by conducting FO fouling and cleaning trials with the feed and draw streams at elevated but equal hydraulic pressures (up to 40 bar), thus sidestepping the need to vary the draw solution concentration to maintain a fixed initial flux. Figure 4-1 illustrates the approaches to examining the effect of pressure on fouling taken by this study and previous studies.

For clarity, we would like to define certain terms relating to pressure in the context of this study. Hydraulic pressure, P, is used to mean the gauge pressure relative to

atmospheric pressure. Therefore, feed hydraulic pressure, P_f, refers to the gauge pressure of the feed. Transmembrane pressure difference (TMP) is the difference in pressure across the membrane (including any fouling layer), $P_f - P_d$, where P_d is the gauge pressure on the back side of the membrane, whether the solution there is draw or permeate. When the draw or permeate pressure is atmospheric, as it is in RO and standard implementations of FO, feed hydraulic pressure is equal to TMP, and this distinction is unimportant. However, our approach to testing the effect of feed hydraulic pressure on fouling propensity involves raising the hydraulic pressure of the draw solution in FO. As a result, feed hydraulic pressure is not necessarily equal to TMP in this study. The final term to define is the pressure drop across the foulant, which refers to the difference in hydraulic pressure between the feed solution and the feed-facing side of the membrane that results from resistance to flow through the foulant layer. The potential effects of these various pressure differences on fouling are discussed in Sec. 4.2.

In Sec. 4.4, we compare measurements of flux decline due to fouling over a range of hydraulic pressures to the theoretical effect of foulant compaction. We also compare the effectiveness of membrane cleaning across different hydraulic pressures. Finally, we record video of the cleaning process to identify effects of pressure on mechanisms of foulant removal. We find no effect of feed hydraulic pressure on flux decline rate, cleaning effectiveness, or foulant removal mechanisms, and conclude that foulant compaction by high feed hydraulic pressure does not explain the high fouling propensity of RO relative to FO.

4.1.1 Role of pressure in osmotic membrane fouling

The theory that hydraulic pressure worsens fouling by compacting foulants stems from a plethora of experimental studies showing that FO fouls more slowly than RO and that FO fouling is easier to remove. The slower flux decline of FO at a given initial flux has been explained by the internal concentration polarization (ICP) self-compensation effect [14, 27, 97], which is unrelated to the system pressure. However, the lower effectiveness of cleaning fouled RO membranes is typically attributed to the

high hydraulic pressure of the feed.

Multiple studies have compared fouling removal in osmotic membrane separation processes at different feed pressures and the same initial flux, and all have observed better fouling reversibility in FO than in RO. Alginate, a polysaccharide that complexes with calcium to form a hydrogel [80, 81] has been used as a model foulant in nearly all of these comparisons. Various differences exist between feed solutions, draw solutions, membranes, channel geometries, and cleaning methods used in these studies, but all show that cleaning effectiveness declines with increasing feed hydraulic pressure. Xie et al. [12] used a feed of 200 mg/L of alginate and 1 mM $CaCl_2$ and a glucose draw solution of varying concentration to compare RO, FO, and pressurized FO. Cellulose triacetate (CTA) FO membranes were used in all processes and cleaning was performed with DI water at high cross-flow velocity. Lee et al. [9] used a feed solution with 200 mg/L alginate, 1 mM $CaCl_2$, and an ionic strength of 50 mM, and cleaning was performed with the same feed at high velocity. CTA FO membranes were used with a draw solution of NaCl. Kim et al. [11] used CTA FO membranes with a feed of 100 mg/L alginate and 1 g/L of colloidal (approximately 100 nm) silica without calcium but with 50 mM ionic strength and an NaCl draw. A feed spacer was used and cleaning was performed at high cross-flow velocity with the same feed solution. Mi and Elimelech [10] used CTA FO membranes with a feed solution of 200 mg/L alginate, 50 mM NaCl, and 0.5 mM $CaCl_2$ and an NaCl draw. Cleaning was performed with a solution of 50 mM NaCl at high cross-flow velocity.

Figure 4-2 summarizes the results of these prior fouling and cleaning studies in terms of cleaning effectiveness (sometimes termed "cleaning efficiency"), which is defined as the fraction of flux lost due to fouling that is recovered by cleaning. Figure 4-2a shows that cleaning effectiveness always decreased with increasing feed pressure. Although they revealed a significant difference between FO and RO, none of these studies truly isolated pressure as an independent variable because the osmotic pressure of the solution on the other side of the membrane was also varied. Because the concentration of the solution opposite the feed (called the "draw" in Fig. 4-2b, even in the case of a pure RO permeate) was also varied between these trials, Fig. 4-

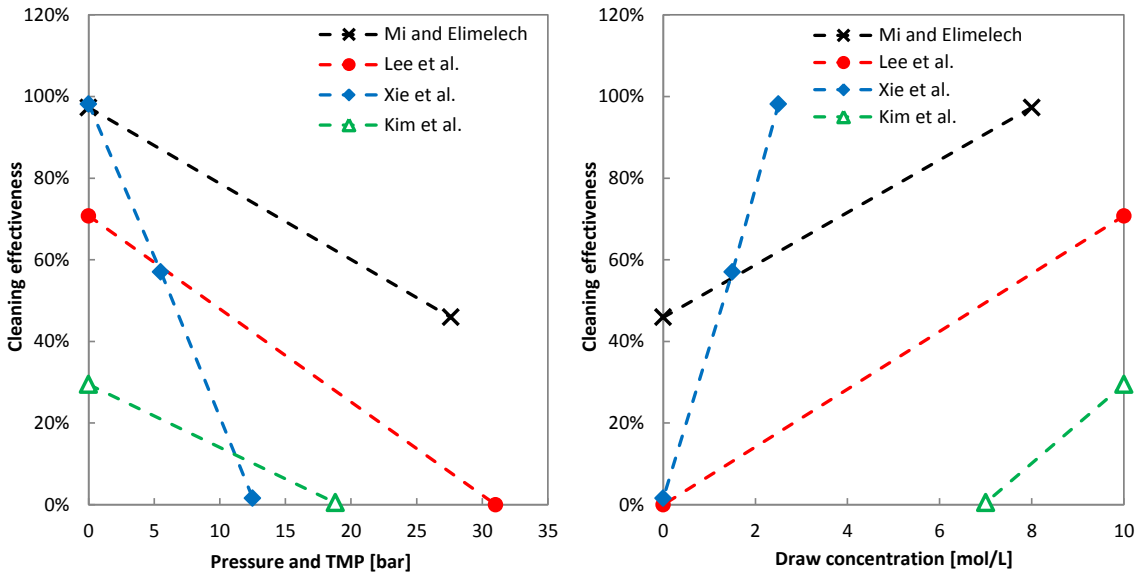

(a) Pressure

(b) Concentration

Figure 4-2: Apparent effects of (a) feed pressure (equal to TMP in these studies) and (b) draw/permeate concentration on alginate fouling reversibility revealed by studies by Mi and Elimelech [10], Lee at al. [9], Xie et al. [12], and Kim et al. [11], in which feed pressure and draw solution concentration were varied together to maintain a particular initial flux. Points represent experimental data; dashed lines are only a guide for the eye. Except in the Xie et al. study, which used glucose, NaCl was used as the draw solute and its concentration is given as total ion concentration here.

2b presents an alternative summary of these results. Experiments in which both pressure and draw concentration are varied cannot distinguish between the effects of feed hydraulic pressure, TMP, draw solute diffusion, and ICP, all of which differ between FO and RO and could potentially influence fouling (see discussion in Sec. 4.5).

Some studies have additionally explored the physical characteristics of fouling layers formed in FO and RO both in situ and ex situ. Mi and Elimelech [10] visually examined fouling layers formed in both processes, and found that FO fouling was more "soft and fluffy, indicating a loose structure." Fouling layers created in FO and RO have also been imaged using confocal laser scanning microscopy (CLSM) to show that both alginate cakes [12] and biofilms [98] are thinner and more uniform in RO than in FO. Although this has been considered to be evidence for foulant compaction by high pressure, the ICP self-compensation effect contributes to the higher foulant thickness in FO [14]. Furthermore, no justification has been given for why pressure should lead to a more uniform foulant layer. Ex situ measurements and images may be affected by changes in the gel's ionic environment that occur after the fouled membrane is removed from the experimental apparatus. Changes in calcium and sodium ion concentration within the gel, such as could occur when it is rinsed or placed in a dye solution, can cause it to shrink or swell [99]. In situ visualization of FO and RO foulant layers has been used to compare mechanisms of foulant removal [13]. Although previous studies suggested that the low pressure in FO led to a looser layer that could more easily be broken up during cleaning [9, 10], in situ observation of mechanical cleaning with reverse permeation revealed a similar progression of wrinkling, tearing, and peeling of full-thickness sheets of gel in both FO and RO [13].

Prior modeling has shown that foulant compaction by the high hydraulic pressure of the RO feed could be significant, but only for foulants with particular properties. Lay et al. [97] find the idea of compaction by high hydraulic pressure "contradictory to the well established critical flux concept," [100] which implies that, "regardless of the type of driving force, the effect of membrane fouling should be comparable

under similar flux and operational conditions." However, Xie et al. [12] show through modeling that high pressure could cause compaction of compressible foulant cakes, i.e., those with Poisson's ratios less than 0.5. Xie et al. model the compression of foulants by pemeate drag, which they state should affect FO and RO similarly at equal flux, as well as compression by "hydraulic pressure," which varies between FO and RO. They do not specify whether "hydraulic pressure" is the absolute feed pressure, gauge pressure of the feed with respect to atmosphere, or TMP[1], but we presume the intended meaning is gauge pressure with respect to atmosphere because their derived expression would predict no foulant compression at zero flux and atmospheric feed pressure. By modeling the foulant cake as a slab of polymer with vertical pores, they find that the ratio of compression by feed pressure ("compaction") to compression by drag is small except when the foulant is "dense" (when the porosity is not close to 1) or when the foulant is compressible. Although alginate was used in all trials summarized in Fig. 4-2, alginate gels are neither dense [63] nor compressible [101]. Xie et al. acknowledge these contradictions, but they suggest that foulant compaction by high feed hydraulic pressure could still occur because hydraulic pressure and drag "work simultaneously and therefore reinforce each other" [12]. A highly-hydrated polymer hydrogel such as alginate (in which free volume is filled with nearly-incompressible water) ought to be essentially incompressible and the effects of drag and hydraulic pressure should be linearly additive. Furthermore, no justification has yet been given for why a thinner, denser alginate gel should necessarily be harder to remove from a membrane.

[1]Gauge pressure of the feed with respect to atmosphere is equal to TMP in standard RO, FO, and pressure-assisted FO processes (the processes tested by Xie et al. [12]), because the draw or permeate is maintained at atmospheric pressure. However, this distinction is important when interpreting the theory developed by Xie et al. in the context of the present study, which includes trials at elevated gauge pressure but zero TMP.

4.2 Modeling the effect of compaction on flux decline

In this section, we develop a model that relates foulant compaction to permeate flux. First, the roles of feed hydraulic pressure, TMP, and pressure drop through the foulant layer are briefly discussed. Next, in Sec. 4.2.1, a model is developed to predict the hypothetical effect of compression by hydraulic pressure on flux decline in FO. Finally, in Sec. 4.2.2, the model is evaluated to aid in the interpretation of experimental results.

As discussed by Xie et al. [12], foulant layer compression in both RO and FO can be caused by the drag-induced hydraulic pressure drop across the foulant layer, which occurs due to permeation through the foulant's small pores. The effect of this pressure drop across the foulant should have the same effect on equivalent fouling layers at equal permeate flux, regardless of the hydraulic pressure of the feed. Even in FO, when the feed and draw solutions are both at atmospheric pressure, a pressure drop can exist across the foulant layer: As water is pulled through the active layer of a fouled membrane by osmosis, the pressure at the foulant–membrane interface dips below atmospheric so that the pressure gradient in the foulant layer is large enough to overcome resistance to flow through the nanoporous gel. In order to separate effects of feed hydraulic pressure from the pressure drop across the foulant layer, all experiments in this study are conducted at the same draw osmotic pressure and zero TMP with the aim of maintaining a fixed initial flux. In practice, variations in membrane properties between samples resulted in some variation in initial flux; we account for this by comparing flux decline rate to flux and initial flux as well as hydraulic pressure.

Regardless of the pressure drop across the foulant layer, high feed hydraulic pressure has the potential to affect foulants that are compressible. The volume of the foulant will depend on its material properties and the hydraulic pressure on the feed side of the membrane, where the foulants are located. The difference in volume of a particular mass of alginate due to accumulation at high pressure (versus accumulation

of the same amount of alginate at atmospheric pressure) can be calculated using the definition of the bulk modulus, K, and its relationship to the compressibility, ν, and Young's modulus, E, of the alginate gel (see Ref. [102]) using Eq. 4.1, which assumes small displacements:

$$\frac{V_u}{V} = 1 - \frac{P}{K} = 1 - \frac{3P(1-2\nu)}{E}, \tag{4.1}$$

where V is the volume of the cake, V_u is the uncompressed volume the same cake at atmospheric pressure, and P is the gauge pressure (with respect to atmosphere) of the feed. More compressible foulants, for which ν is significantly less than 0.5, will experience greater strain in response to increased feed hydraulic pressure. Incompressible foulants will not be compressed by high feed hydraulic pressure.

Xie et al. [12] similarly found that foulant compressibility ($\nu < 0.5$) would lead to an effect of feed pressure on foulant density. Values of E and ν for alginate gel, the model foulant used in studies that saw a difference in fouling reversibility between FO and RO, as described in Sec. 4.1.1, have been calculated by Wang et al. [101] from micro-sphere compression tests conducted at high compression speed to minimize flow of water out of the nanoporous gel. Wang et al. show that alginate is incompressible or nearly so, and it is therefore unlikely that high hydraulic feed pressure will contribute to compressing alginate foulant. Nevertheless, the dominant explanation of RO's high fouling propensity relative to FO is that high feed hydraulic pressure compacts foulants, so we will consider the possibility that alginate gel could be slightly compressible and thus its volume (per unit mass of polymer) could decrease with increasing feed hydraulic pressure.

Taken independently from flux and feed hydraulic pressure, TMP itself is unlikely to cause compaction of foulants on FO or RO membranes. Fouling and cleaning could theoretically be affected by TMP in the case of single-layered nanoporous graphene RO membranes (see, e.g., Ref. [103]), which have straight-through pores, but the active layers of commercial RO and FO membranes are generally considered to be either nonporous or composed of an interconnected nano-pore network. The solution-diffusion model [61, 104] considers the active layer to be nonporous and, modeling the

active layer and contained water as a single phase [105], predicts uniform pressure equal to that of the feed throughout the active layer. According to this model, foulants on the feed side of the membrane are only exposed to the feed pressure and the permeate (or draw) pressure is irrelevant. More recent studies show that the RO active layer contains free-volume holes with diameters in the range of 0.40-0.58 nm [106]. Even so, as long as water flow paths are interconnected (as they are in most porous materials), pore blocking should not lead to propagation of the draw/permeate pressure back to a foulant particle deposited on the feed side, and the draw/permeate pressure (and thus TMP) should again be irrelevant. However, TMP may still affect fouling and cleaning in other ways, e.g., through changes in membrane texture as a result of pressurization, as seen in CLSM images of fouling of FO membranes with and without TMP [98]. The present study does not vary TMP, and thus cannot resolve effects of TMP on fouling.

4.2.1 Properties of compressed foulant cakes

Flux in FO depends on the thickness, tortuosity, porosity, and hydraulic diameter of the foulant layer as well as the feed composition, draw composition, channel hydrodynamics, and membrane properties [14]. In this model, we assume that only the foulant layer properties are affected by hydraulic pressure, and neglect any possible effects of pressurization on the membrane or solutions. The model focuses on alginate fouling, specifically, because of the extensive use of alginate in previous studies of the effect of pressure on fouling as well as the structural similarity of alginate to extracellular polymeric substances (EPS) [79], which play a significant role in biofouling. To relate changes in the foulant layer properties to volumetric compression, we model the alginate gel as an isotropic 3–D scaffold of alginate chains in water with uniform pore sizes. The surface area of the polymer–water interface is assumed to be a function of the alginate composition (particularly the polyguluronate fraction) and ionic composition of the surrounding solution and thus constant during compression. The equations developed in this section are intended to predict the effect of compression on foulant cake properties regardless of whether compression occurs due

to permeation through the foulant cake, high feed hydraulic pressure, or both.

The alginate gel pore hydraulic diameter, D_h, can be defined on a volumetric basis as it would be for a tube bundle:

$$D_h = \frac{4V\phi}{A_s} \tag{4.2}$$

where A_s is the alginate–water interfacial surface area inside a volume V of gel, and ϕ is the gel porosity (or water volume fraction). Assuming the alginate chains are not themselves compressible, the volume of polymer should be constant during the compression:

$$(1-\phi)V = (1-\phi_u)V_u, \tag{4.3}$$

where the subscript u refers to the uncompressed gel at atmospheric pressure. Substituting Eq. 4.3 into Eq. 4.2 gives the hydraulic diameter as a function of volumetric compression:

$$D_h = D_{h,u}\Big(1 - \frac{1 - V/V_u}{\phi_u}\Big), \tag{4.4}$$

where $D_{h,u} = 4V_u\phi_u/A_s$ is the hydraulic diameter at atmospheric pressure. Equation 4.4 shows that pore hydraulic diameter decreases due to compression, in agreement with the assessment of Xie et al. [12].

The gel porosity should decrease with compression according to Eq. 4.5:

$$\phi = 1 - \frac{(1-\phi_u)V_u}{V}. \tag{4.5}$$

The relationship between porosity and tortuosity, τ, has been the subject of many investigations, some of which are reviewed in Ref. [107]. A general correlation for packed beds of various geometries is given by Mauret and Renaud [108]:

$$\tau = 1 - 0.49\ln(\phi). \tag{4.6}$$

Due to the high porosity typical of alginate gels, tortuosity is expected to remain close to one.

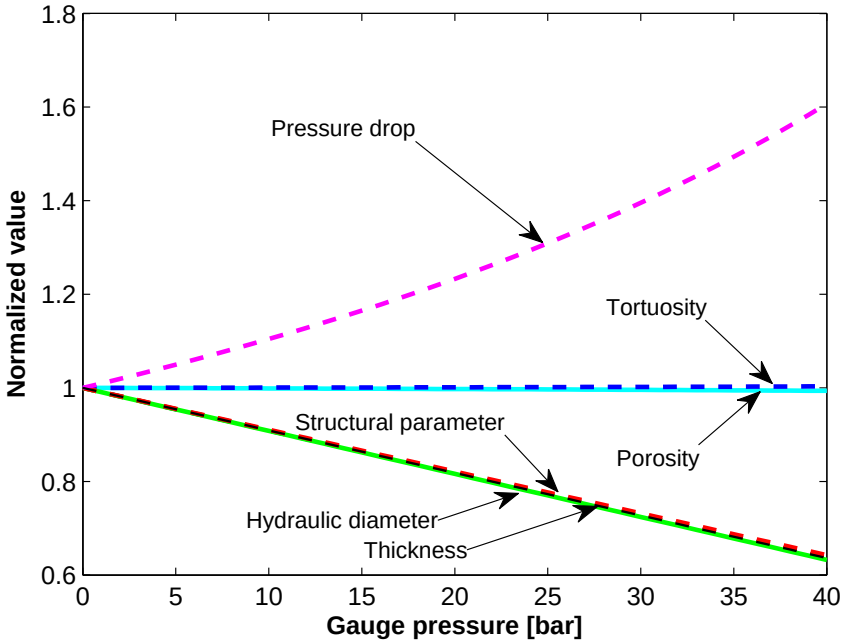

Figure 4-3: Modeled effect of pressure on foulant cake properties with a hypothetical Poisson's ratio of $\nu = 0.495$. Each parameter is normalized by its uncompressed value for a cake formed at atmospheric pressure.

Compression is typically thought to accelerate flux decline, but foulant compression may increase or decrease flux decline rate depending on the dominant mechanism of flux decline. Although the thickness, δ, of a gel containing a fixed mass of polymer decreases due to compression as in Eq. 4.7,

$$\delta = \delta_u \frac{V}{V_u}, \tag{4.7}$$

the simultaneous decrease in pore size causes an overall increase in hydraulic resistance, which is proportional to δ/D_h^2 [14]. On the other hand, cake-enhanced concentration polarization (see, e.g., [60]) is reduced due to the decreased cake thickness. Both mechanisms of flux decline are also affected by changes in porosity and tortuosity resulting from compaction, although the high hydration of alginate renders these effects insignificant.

The modeled effect of compression on the cake properties D_h, ϕ, τ, and δ, as

well as the cake's structural parameter ($\delta\tau/\phi$) and hydraulic pressure drop at a given flux (see [14]) is plotted in Fig. 4-3 for a hypothetical 2% wt. alginate gel with a slight compressibility ($\nu = 0.495$). Pressure drop through the foulant cake increases while thickness, cake structural parameter, and pore hydraulic diameter decrease almost identically. Tortuosity and porosity change very little because of alginate's high water mass fraction.

4.2.2 Foulant accumulation and flux decline

In this section, we model the effect on flux of compression-induced changes in foulant layer properties and predict the effect of compression on flux decline.

Foulant accumulation on the membrane is modeled as the difference between deposition and removal rates as in the critical flux model for cake fouling developed for microfiltration by Field et al. [100] and validated against RO fouling experiments by Qureshi et al. [88]. Various mechanisms govern transport toward and away from the membrane, depending on the separation process and the type of fouling. For the alginate fouling of FO membranes considered here, foulant deposition rate is modeled as being equal to the rate of convection toward the membrane, which is proportional to the permeate flux J_w and foulant mass fraction ω_A in the feed:

$$\dot{m}''_D = J_w \omega_A. \tag{4.8}$$

Foulant removal rate is assumed to be constant in time, as in the cake filtration model of Field et al. [100]. In RO, the removal rate is reported to be a function of solution composition and temperature, cross-flow velocity, system geometry (e.g., feed channel thickness and spacer type), and TMP [88]. We assume the same is true for FO, and therefore the rate of removal is not expected to vary between the FO trials conducted in this study under conditions that are identical except for the varying feed hydraulic pressure. Over time, flux is expected to approach an asymptote at which the rate of deposition equals the rate of removal (the "critical flux" [100]), or at least reduce to a level where further foulant accumulation is negligible (the "threshold

flux" [109]). Given that neither rate of deposition nor rate of removal are expected to depend on hydraulic pressure, the asymptotic flux is not expected to vary with hydraulic pressure. The pressure-independence of the asymptotic flux, J_w^*, has been demonstrated experimentally in a comparison of alginate fouling in FO, pressurized FO, and RO with identical membranes, in which the flux reached an asymptotic limit of approximately 14 L/m^2-hr (lmh) in all three cases despite differing pressures [12].

The net accumulation rate of mass on the membrane, $\dot{m}''$, is equal to the rate of deposition minus the rate of removal, where the rate of removal is equal to the rate of deposition evaluated at the asymptotic flux, J_w^*:

$$\dot{m}'' = (J_w - J_w^*)\omega_A. \tag{4.9}$$

Given the very low permeate recovery (<1%) of a single pass through the 8 cm-long channel used in our experiments, the water flux and foulant mass flux are assumed to be uniform. Effects of spatial variations in mass transfer coefficient on flux and foulant removal rate are neglected in the present analysis.

The rate of change in foulant cake thickness is related to the foulant accumulation rate and gel porosity:

$$\frac{\mathrm{d}\delta}{\mathrm{d}t} = \frac{[J_w(t) - J_w^*]\omega_A}{(1-\phi)\rho_A}, \tag{4.10}$$

where ρ_A is the density of the alginate polymer that composes the solid phase of the gel.

Flux decline can be predicted by integrating Eq. 4.10 numerically: At each time step, flux is calculated as a function of foulant thickness and morphology using a layered model of water and solute transport through fouled FO membranes detailed in Ref. [14], which accounts for both cake-enhanced osmotic pressure and cake hydraulic resistance.

Depending on the foulant composition and feed salinity, compression can lead to either higher or lower rates of flux decline. The initial rate of flux decline (at the limit of zero foulant accumulation, so that there is no compression due to flux through the foulant cake) is predicted as a function of feed salinity for several degrees of volumetric

compression in Fig. 4-4 that could hypothetically occur due to high feed hydraulic pressure and/or pressure drop across the foulant layer. The feed solution is modeled as 0.02% wt. alginate and 1 mM $CaCl_2$ as in the experiments reported in Sec. 4.4. The draw solution is modeled as 5 M NaCl. The pore hydraulic diameter of the uncompressed foulant cake[2] is modeled using a linear interpolation of pore diameters estimated from experimental measurements at different NaCl concentrations in Ref. [14] for alginate cakes formed in feed solutions containing 1 mM $CaCl_2$. The alginate polymer density was modeled as $\rho_A = 1800$ kg/m^3 [63] and the uncompressed gel porosity was estimated as $\phi_u = 0.9889$ based on a polymer mass fraction of 2%, which is within the typical range of alginate gels [63]. The asymptotic flux, at which the rate of foulant advection equals the rate of removal, is taken to be 11 lmh based on experimental measurements under the modeled conditions (refer to Fig. C-1). FO membrane properties, which themselves affect flux decline, are based on our previous measurements of HTI's CTA membranes [14] and are assumed to be independent of pressure.

Figure 4-4 shows that the effect of alginate compression on flux decline depends on NaCl concentration. At low NaCl concentration, compression should increase the initial rate of flux decline, but at higher NaCl concentration, the higher feed osmotic pressure and foulant pore diameter cause the reduction in cake-enhanced osmotic pressure to overcome the increase in hydraulic drag, and the effect of compaction is actually to *mitigate* flux decline. The point at which alginate compaction has no effect on flux decline will vary depending on the feed osmotic pressure, but for the feeds used in this study, which contain alginate and 1 mM calcium ion, the NaCl concentration at which the effect of compaction switches from detrimental to beneficial is approximately 0.11 M.

We will use the theoretical prediction that cake compression should raise the rate of flux decline at 29 mM NaCl to interpret experimental results and determine whether or not foulant compaction by high feed hydraulic pressure occurs. If the flux

[2]Calculations from experimental data [14] suggest that pore diameter rises from approximately 6 nm at 10 mM NaCl to 20 nm at 390 mM NaCl, at which point hydraulic resistance becomes negligible in comparison to cake-enhanced osmotic pressure.

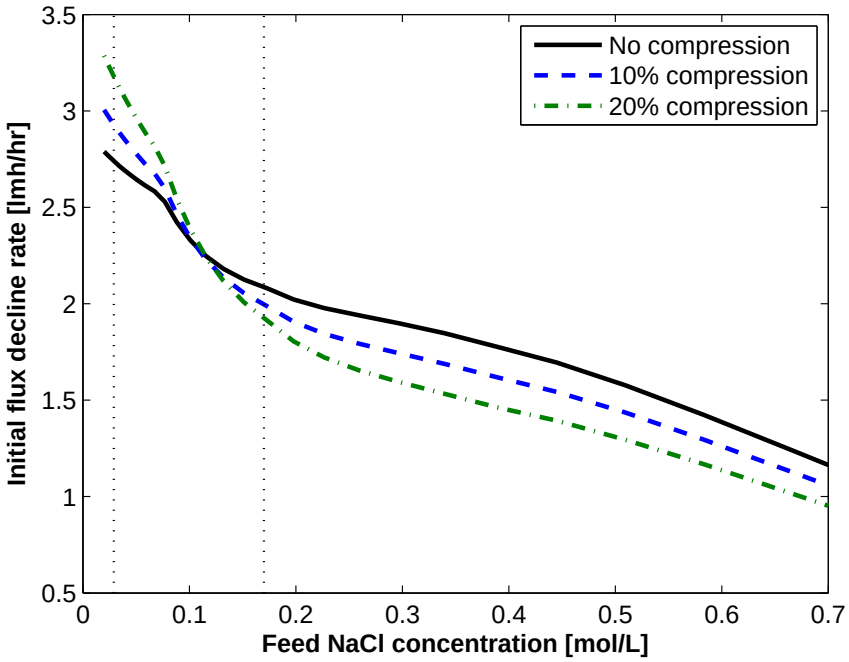

Figure 4-4: Predicted initial flux decline rate as a function of feed NaCl concentration and alginate gel strain due to three hypothetical degrees of compression (including none). The feed solution is modeled as 0.02% wt. alginate and 1 mM $CaCl_2$ and the draw solution is modeled as 5 M NaCl. The NaCl concentrations of the two solutions tested experimentally in this chapter (29 and 174 mM) are marked with vertical dotted lines.

decline rate at a given flux increases with increasing feed hydraulic pressure at 29 mM NaCl, we will conclude that foulant compaction by high feed hydraulic pressure occurs. If flux decline rate is independent of pressure, we will conclude that alginate fouling is (as direct measurements of alginate gels [101] suggest) incompressible and that foulant compaction by high feed hydraulic pressure does not occur.

4.3 Experimental methods

The effect of hydraulic pressure on FO membrane fouling was tested in a custom plate-and-frame FO membrane module that could be pressurized equally on feed and draw sides. Pressure, temperature and flow rate were controlled while changes in flux were measured. Each flow channel was 80 mm long, 30 mm wide, and 1 mm deep. The experimental apparatus is shown schematically in Fig. 4-5; details of measurement, control, and module design are given in Refs. [13, 14]. In situ visualization of foulant removal is enabled by a polycarbonate window in the membrane module (see Ref. [13] for details). Feed and draw pressures are kept equal by connecting the back pressure regulators (Equilibar) in both feed and draw loops to the same pressure-regulated supply of nitrogen gas.

Whereas previous comparisons pressurized only the feed stream [9, 10, 11, 12] and varied draw solution concentration to achieve a fixed initial flux, this apparatus allows feed and draw pressures to be raised together, eliminating the need to vary the draw solution concentration. It also separates feed hydraulic pressure from TMP; by varying the feed and draw pressures together, TMP can be maintained close to zero, as is typical in FO systems.

4.3.1 Feed and draw solutions

The feed solution contained deionized water, 200 mg/L sodium alginate (Sigma-Aldrich A2033, referred to as "alginate" elsewhere in this chapter), 1 mM calcium chloride (Alfa Aesar 99% min.) to induce gelation of alginate (refer to, e.g., [81, 110], for more information on alginate–calcium complexation), and varying concentrations

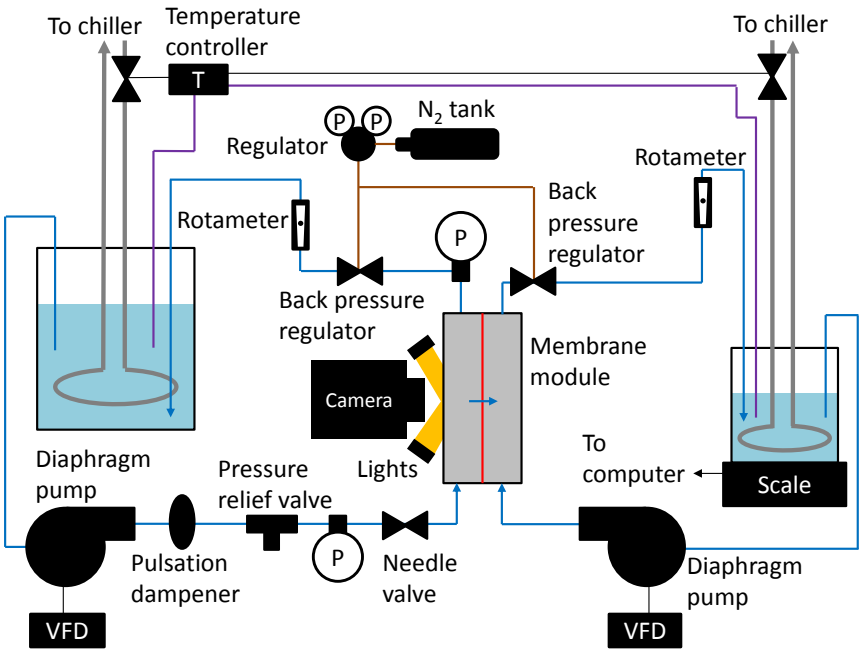

Figure 4-5: Schematic diagram of the experimental high-pressure FO fouling measurement apparatus. Feed and draw streams are pressurized equally. Figure adapted from Ref. [13].

of sodium chloride (Alfa Aesar 99% min.). The sodium chloride concentration was varied in order to capture effects of both cake-enhanced concentration polarization and cake hydraulic resistance. In some trials, 7.6 μM methylene blue (Alfa Aesar), which was previously shown to be a benign dye that does not affect fouling rate or cleaning effectiveness in RO [13], is used in the feed to dye the alginate gel for visualization of foulant removal.

A nearly-saturated sodium chloride solution (approximately 5 M) in deionized water was used as the draw solution at a cross-flow velocity of 4.3 cm/s. The draw solution was partially degassed before use to prevent accumulation of air in the draw loop and associated flux measurement error. The highly-concentrated draw, though not practical for real FO desalination systems, was used in this experiment to drive a high water flux (similar to fluxes used in RO) and accelerate fouling.

4.3.2 Membranes and spacers

Asymmetric cellulose triacetate (CTA) membranes (Hydration Technology Innovations) were used with the active layer facing the feed. Properties of these membranes were previously characterized in Ref. [14]. Membranes were soaked in a solution of 50% ethanol and 50% deionized water for approximately 5 minutes and then rinsed in deionized water before being installed in the membrane module. They were then equilibrated with foulant-free feed and draw solutions (with feed velocity at least 16.7 cm/s during equilibration to discourage premature fouling) at the final pressure for at least 90 minutes and until flux stabilized.

Two layers of 0.43 mm-thick spacer (Sterlitech 17 mil) were used to maintain the draw channel at the appropriate depth and increase the mass transfer coefficient. Where noted, one 0.79 mm-thick spacer (Sterlitech 31 mil) was used in the feed channel to reduce the rate of fouling. The higher velocity of the feed relative to the draw created a slight pressure difference between the feed and draw channels such that the membrane lay flat against the draw spacers.

4.3.3 Fouling and cleaning procedures

After equilibrating the membranes with the draw solution and foulant-free feed, concentrated alginate and calcium chloride solutions were added sequentially and the feed velocity was reduced from 16.7 cm/s to 8.3 cm/s to initiate fouling. Fouling was carried out for 8 h before cleaning.

For the cleaning step, the feed cross-flow velocity was increased by a factor of three to 25 cm/s and osmotic backwashing was carried out for 60 minutes. In this case, osmotic backwashing involved substituting Cambridge, Massachusetts tap water (which is acceptable to use with the chlorine-tolerant CTA membranes) in place of the draw solution so that the direction of permeation reversed. Permeation direction was reversed to enhance cleaning by both changing the direction of the viscous drag force and changing the ionic composition of the solution within the gel to encourage swelling and gel detachment [13]. After 60 minutes, the feed velocity was returned

to 8.3 cm/s, the draw solution was re-introduced, and the draw tank salinity was re-measured to account for any water added during the transition from the cleaning step. Pressure was maintained throughout the entire cleaning step at the value used during the fouling period.

Fouling and cleaning trials were repeated three times under each of six sets of conditions. In six trials (one under each set of conditions), video of the fouled membrane was recorded during the cleaning process. The resulting videos are provided in the supplementary materials of Ref. [89].

4.4 Results

4.4.1 Flux decline

In this section, rates of flux decline are compared across trials at different pressures, demonstrating the absence of anticipated effects of compaction on flux decline. Although the experimental design aimed to decouple feed hydraulic pressure from flux, significant variation in initial flux occurred. There was no strong relationship between initial flux and feed pressure, as demonstrated by correlation coefficients of 0.02 and -0.08 for the low-salinity and high-salinity trials, respectively. Each trial began with near-saturated NaCl draw solutions whose variation in concentration should lead to initial fluxes within approximately ± 0.75 lmh if all membrane samples had identical properties, according to the FO membrane transport model of Ref. [14]. However, the actual initial fluxes varied ± 5.7 lmh, suggesting a significant variation in membrane properties between coupons. To account for the effects of initial flux on fouling and flux decline, we present not only the measured flux but the relationship between flux decline rate and flux (Figs. 4-7 and 4-10) and the normalized flux over time (see App. C.1).

Figure 4-6 shows measured flux decline for three trials each at 0, 4, 20, and 40 bar with a feed solution of 29 mM NaCl, 1 mM $CaCl_2$, and 200 mg/L alginate,

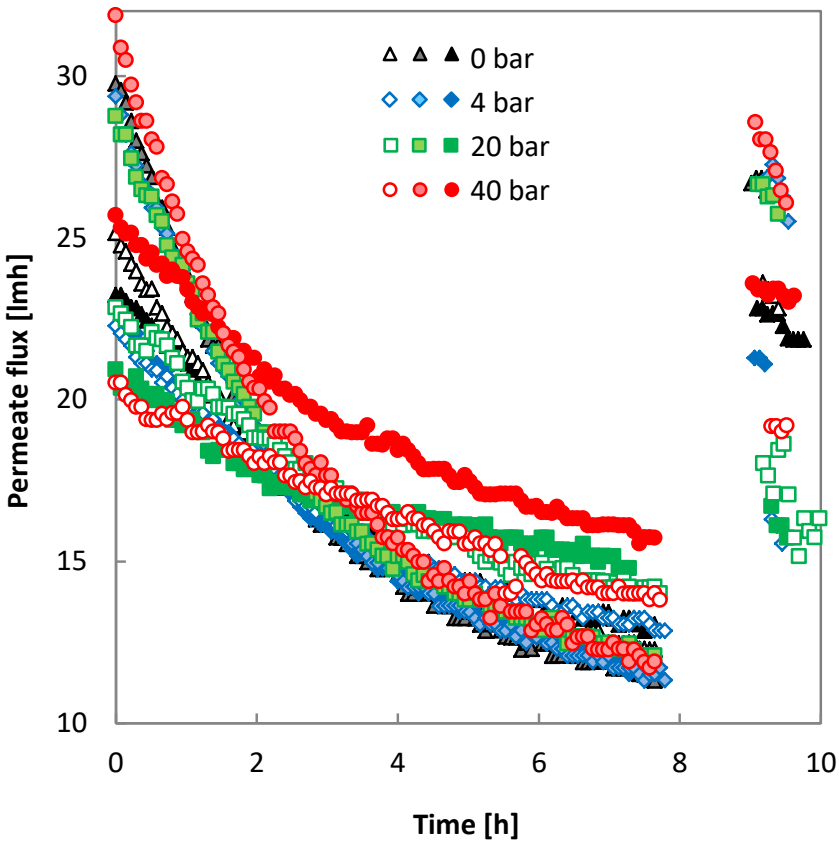

Figure 4-6: Experimental flux decline curves for FO fouling at various pressures with a low-salinity feed (29 mM NaCl, 1 mM $CaCl_2$, and 200 mg/L alginate) and no feed spacer. Repeated trials are denoted by symbols of the same shape and outline color.

without a feed spacer[3]. Duplicate trials are denoted by symbols of the same shape and outline color with different fill colors. The gap after 8 h is the cleaning step; cleaning effectiveness is discussed in Sec. 4.4.2.

The theory developed in Sec. 4.2 dictates that, for the low-salinity trials shown in Fig. 4-6, cake-enhanced osmotic pressure is negligible and foulant compaction should lead to faster flux decline at higher pressure due to the increase in hydraulic resistance of a more dense fouling layer. Although the initial fluxes vary, the four trials (one at each of the four pressures) that began at high flux (28-32 lmh) exhibit nearly identical flux decline profiles, suggesting that hydraulic pressure does not affect flux decline. Trials with higher initial flux generally exhibit more rapid flux decline, and the flux

[3]An earlier subset of the data shown in Fig. 4-6 are reported in Ref. [111] by the same authors.

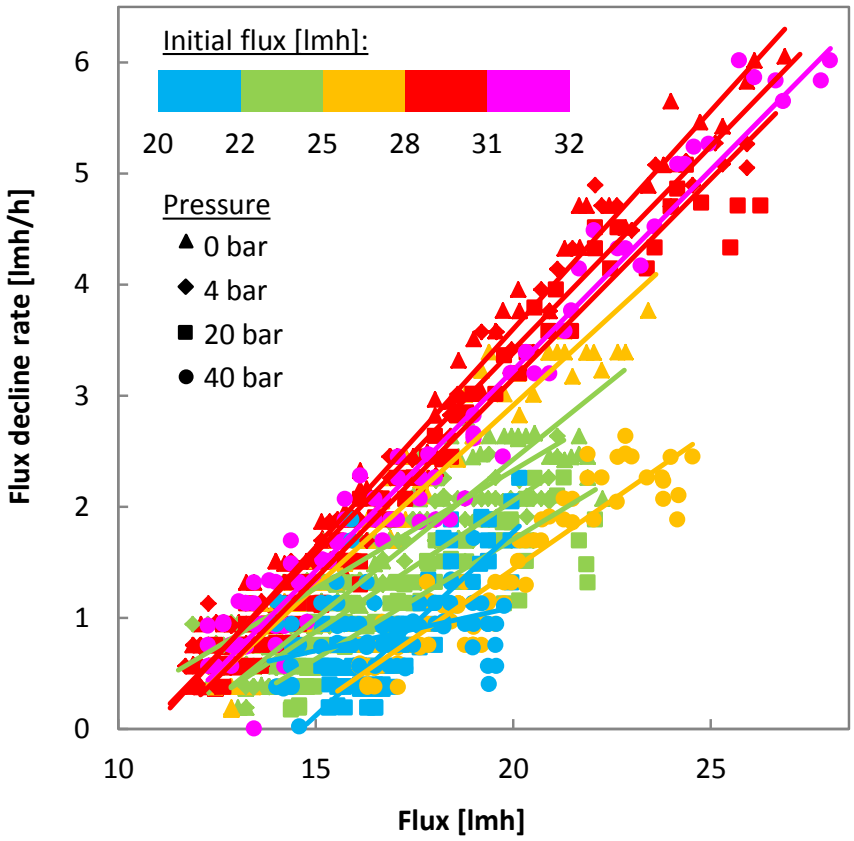

Figure 4-7: Flux decline rate (averaged over 2 h) plotted against flux for the data shown in Fig. 4-6. Symbol shape denotes operating pressure; color denotes initial flux. Lines are linear fits of the data from each trial.

decline profiles of most trials cross around 3 h.

To untangle the effects of pressure, flux, and initial flux, we plot flux decline rate (averaged over 2 h periods) versus flux (at the middle of the time period) in Fig. 4-7. The relationship between flux decline and flux is roughly linear due to the convection of foulants to the membrane [88], and linear fits were applied to the data. Although the asymptotic flux (at which the rate of flux decline reaches zero) is comparable between all trials, the rate of flux decline at a given higher flux varies significantly. In Fig. 4-7, shapes correspond to operating pressure and colors correspond to initial flux. No correlation is evident between pressure and flux decline rate. However, it seems that the flux decline rate at a given flux increases with increasing initial flux.

The dependence of flux decline rate on not only the current flux but also the

initial flux arises from the effects of further foulant accumulation on the existing foulant cake, as illustrated in Fig. 4-8. When new gel forms on the membrane at the onset of fouling, it increases concentration polarization and imposes drag on the water flowing through it. This leads to increased concentration and decreased pressure at the membrane and, as a result, decreased flux. When additional gel forms on the surface of the existing gel, it creates additional drag and increases the pressure drop through the gel, compressing the existing gel. As discussed in Sec. 4.2, porous gels can be compressed due to the drag-induced pressure difference across the gel layer, which increases as new gel is deposited. This pressure difference across the gel depends on the gel properties and permeate flux and does not depend on feed hydraulic pressure or TMP. As shown in Ref. [12], gel compressibility ($\nu < 0.5$) is not required for compression by water permeation through the gel. When the gel pore size and feed solution are small enough that compression accelerates flux decline (true in the case of the low-salinity trials; see Fig. 4-4), then the rate of flux decline at a given flux should increase with initial flux, as it does in Fig. 4-7.

To more accurately simulate membrane fouling in real treatment systems, we also tested the effect of pressure with a feed spacer and a more saline feed solution (174 mM NaCl, 1 mM $CaCl_2$, and 200 mg/L alginate)[4]. With this feed solution, the model of Sec. 4.2 shows that both hydraulic resistance and cake-enhanced concentration polarization should contribute to flux decline, and the net effect of compaction is expected to mitigate flux decline, but only slightly (refer to Fig. 4-4). No independent effect of pressure on flux decline rate is discernible from flux measurements (Fig. 4-9), even when normalized (Fig. C-2).

The effect of pressure, flux, and initial flux on flux decline rate are presented in Fig. 4-10 for the trials using the moderate-salinity feed solution (174 mM NaCl, 1 mM $CaCl_2$, and 200 mg/L alginate) and a feed spacer. As in Fig. 4-7, symbol color and shape correspond to hydraulic pressure and initial flux, respectively. Flux decline rate clearly increases with increasing flux, but there is no clear relationship between flux

[4]Flux data for one trial at atmospheric pressure was also presented in comparison with a spacer-free trial in Ref. [13].

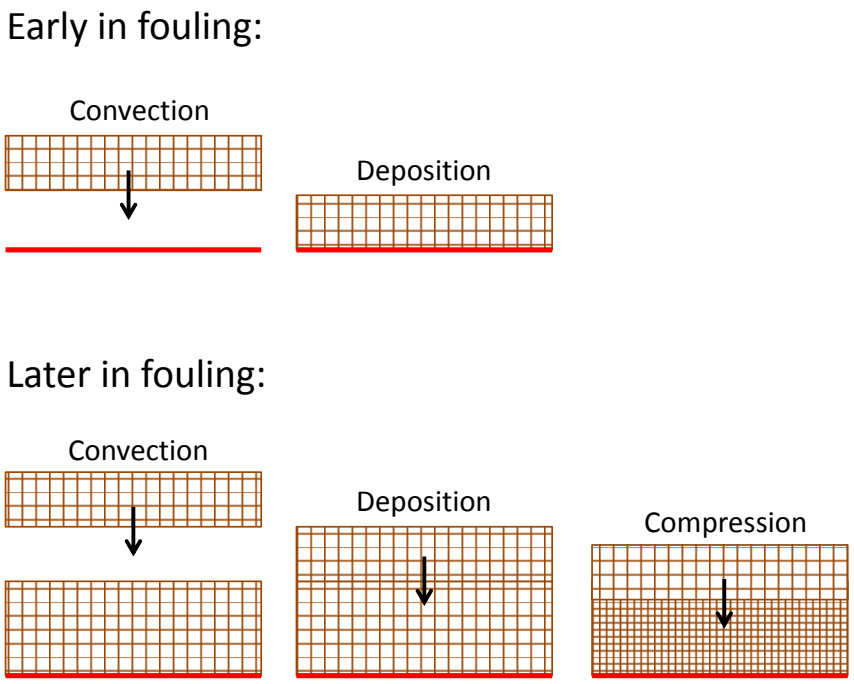

Figure 4-8: Illustration of the effect of existing foulant on the flux decline that results from further fouling. When foulant deposits on top of existing foulant, it increases the thickness of the foulant cake as well as the drag-induced pressure drop across it, leading to foulant compression regardless of feed hydraulic pressure or TMP.

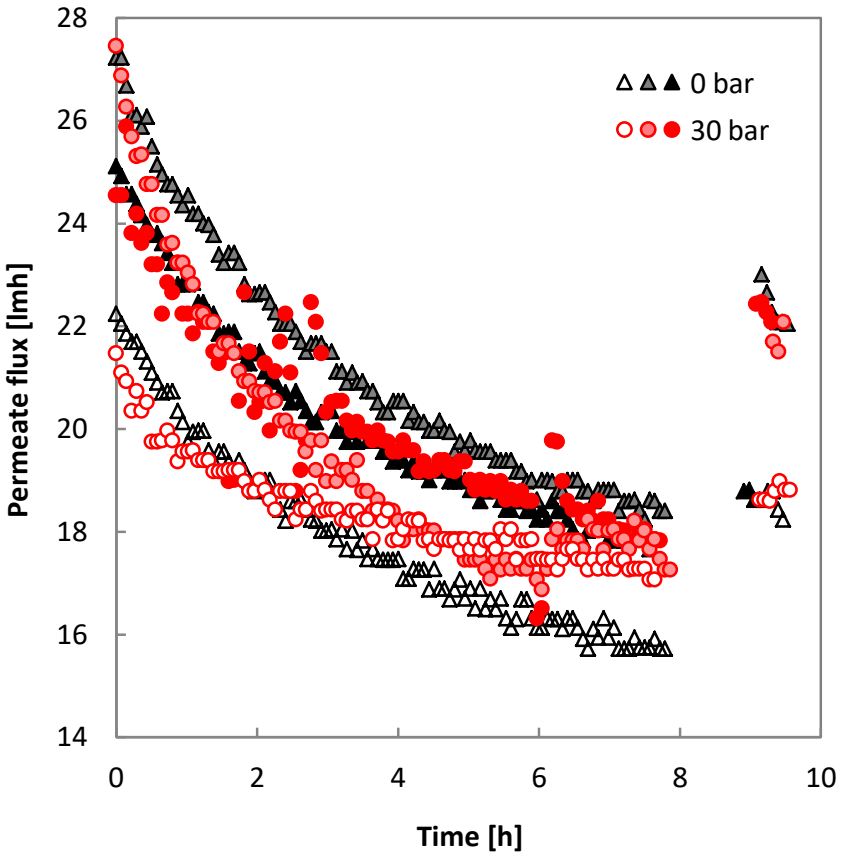

Figure 4-9: Experimental flux decline curves for FO fouling with a feed spacer at various pressures with a medium-salinity feed (174 mM NaCl, 1 mM $CaCl_2$, and 200 mg/L alginate). Flux is normalized by 21.5 lmh. Repeated trials are denoted by symbols of the same shape and color.

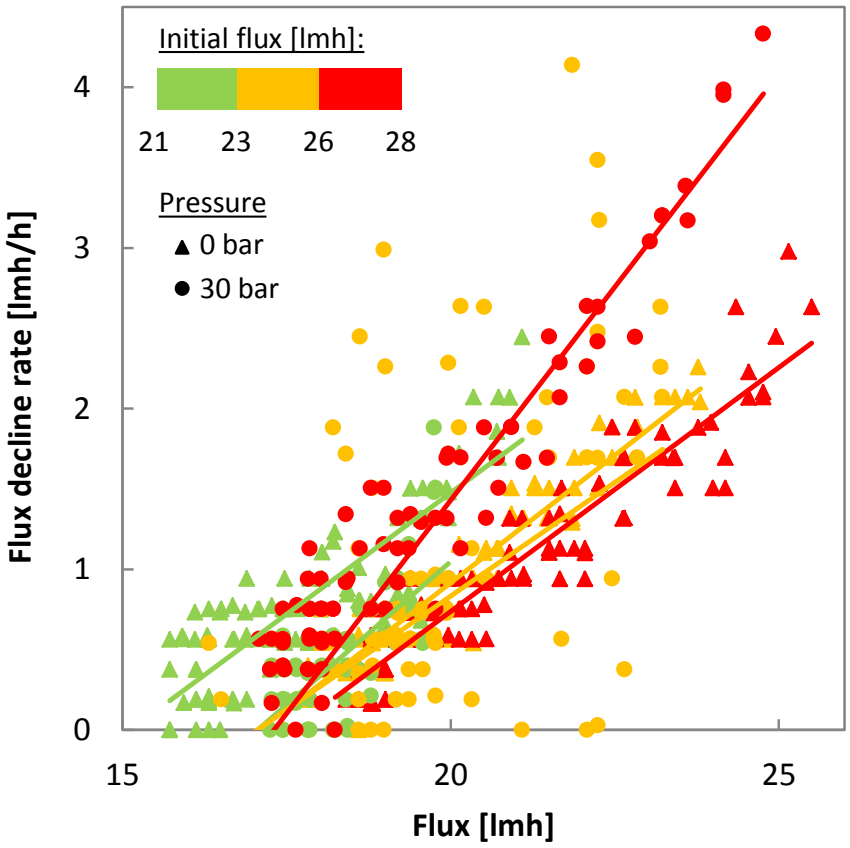

Figure 4-10: Flux decline rate (averaged over 2 h) plotted against flux for the data shown in Fig. 4-9. Symbol shape denotes operating pressure; color denotes initial flux. Lines are linear fits of the data from each trial.

decline rate and pressure or initial flux. This is expected, as the effect of compaction (due to either high feed hydraulic pressure or flux through the foulant layer) on flux should be minimal for alginate fouling at 174 mM NaCl and 1 mM $CaCl_2$ (see Fig. 4-4).

The dependence of flux decline rate on initial flux at low salinity (and lack thereof at moderate salinity) shows that this experiment did capture the effect of foulant compression on flux; however, the dependence of flux decline rate on initial flux only relates to compression by water flow through the foulant layer. The lack of any effect of feed hydraulic pressure on flux decline rate at low salinity (Fig. 4-7), where foulant compression should accelerate flux decline, shows that feed hydraulic pressure did not compact foulants.

4.4.2 Cleaning effectiveness

In this section, we examine the effect of pressure on the ease of foulant removal. Even though the fouling trials in Sec. 4.4.1 do not validate the theory of foulant compaction, previous studies (Refs. [9], [10], [11], [12], and [13]) have shown substantial disparities in cleaning effectiveness between FO and RO fouled at the same initial flux under identical hydrodynamic conditions. However, by isolating absolute feed pressure from draw solution concentration and TMP, we find that feed pressure alone does not have a strong effect on cleaning effectiveness, even over a larger pressure range than tested previously.

Figure 4-11 shows the calculated cleaning effectiveness (defined in App. C.2) for all experimental trials. Significant variability in cleaning effectiveness occurs even under replicated conditions, which is not surprising, given the large size of sloughed alginate gel pieces (see Fig. 4-12). Due to the peeling mechanism of gel removal by osmotic backwashing, the cleaning effectiveness is almost binary in the absence of feed spacers. With feed spacers, the gel breaks into much smaller pieces (roughly the size of the spacer grid; see Ref. [13]), and the average cleaning effectiveness was closer to 50% at both 0 and 30 bar.

Figure 4-11 does not reveal a strong correlation between fouling reversibility and pressure. Cleaning was consistently effective at 40 bar, the highest pressure tested, demonstrating that low pressure is not a requirement for effective membrane cleaning. Contrasting the significant difference in fouling reversibility between RO and FO identified by previous studies (Fig. 4-2) with the relative indifference to pressure demonstrated in Fig. 4-11, it would appear that the cause of the superior fouling reversibility of FO is something other than its low pressure.

Because previous reports [9, 10] have postulated that feed pressure affects cleaning effectiveness by altering the mechanism of foulant removal, we captured video of the cleaning process at each pressure and salinity tested. The six videos are available in the supplementary materials of Ref. [89]. In the moderate-salinity trials with a feed spacer, the feed spacer obscures the video sufficiently that we chose not to include

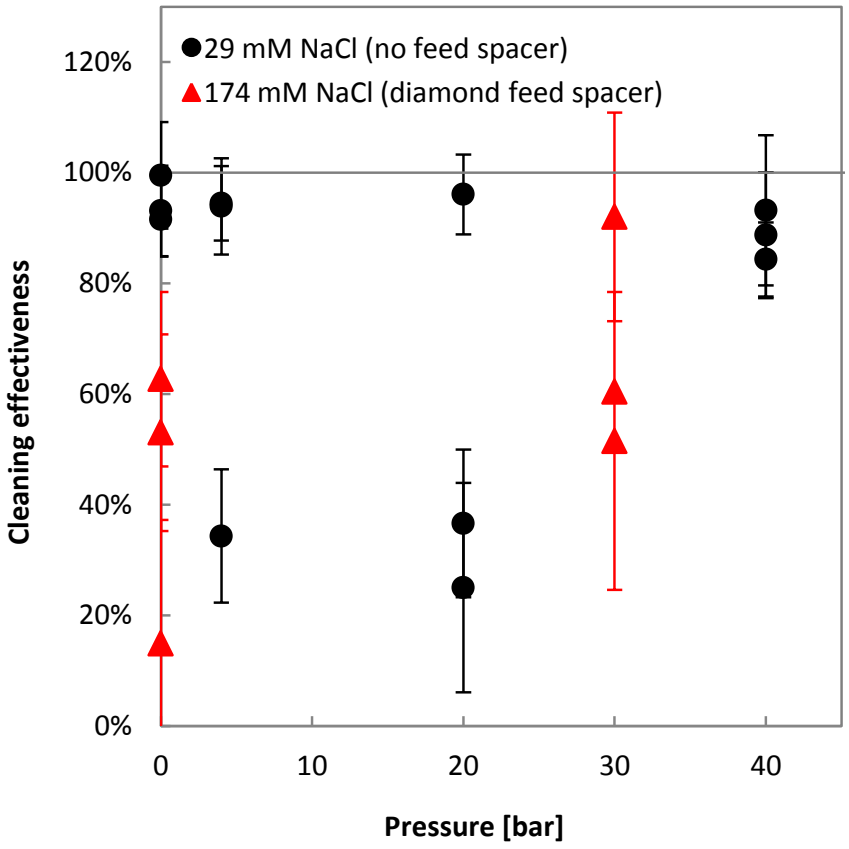

Figure 4-11: Cleaning effectiveness as a function of pressure for all trials shown in Figs. C-1 and C-2. Error bars represent 95% confidence intervals calculated as described in App. C.3.

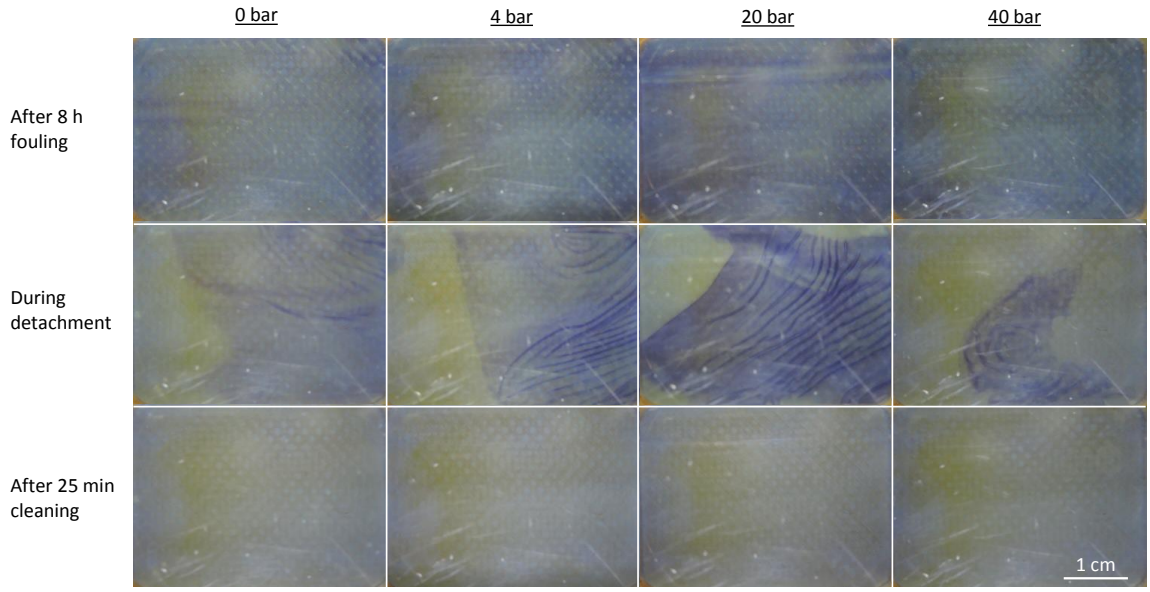

Figure 4-12: Stills from video of cleaning FO membranes fouled with low-salinity feed (29 mM NaCl, 1 mM $CaCl_2$, 200 mg/L alginate, and 7.4 μM methylene blue). In each case, the sheet of gel detached from the membrane and was swept away in the flow (left to right).

still images here. However, no clear difference exists between cleaning processes at 0 and 30 bar; in either case, small pieces of foulant detach, flow along the direction of one set of spacer filaments, and largely remain in the channel. The foulant removal process is easier to see in the low-salinity trials without a feed spacer, so stills at key points (before, during, and after the foulant layer peels off) are provided in Fig. 4-12. The mechanism of foulant removal is consistent across feed pressures from 0–40 bar: The foulant layer wrinkles, stretches, tears, and then completely detaches from the membrane.[5] Previous assertions that unpressurized alginate gel is more susceptible to breakup by shear forces are not supported by these results.

4.5 Discussion: fouling resistance in FO

Although high feed pressure is typically blamed for the difficulty of removing fouling in RO, this study provides evidence that feed hydraulic pressure does not affect fouling or

[5]The same behavior was observed in RO as well as FO in our in situ visualization study [13] and can be explained by alginate gel swelling due to reduced ion concentration during the cleaning step.

foulant removal. No effect of feed pressure on flux decline was observed, and there was no clear relationship between feed pressure and cleaning effectiveness. Furthermore, in situ visualization of the cleaning process demonstrated that the mechanisms of fouling removal did not vary with feed pressure. The results of this study regarding the effect of pressure on fouling likely differ from the results of previous studies due to the variation of draw pressure, rather than draw concentration, to maintain initial flux across trials at different feed pressures.

Significant differences in cleaning effectiveness after fouling at different feed pressures and draw solution concentrations in previous studies is likely influenced by the draw solutions or TMP. The presence of a draw solution could increase fouling reversibility in FO through solute back-diffusion or increasing the spatial variation in permeate flux. TMP could directly affect cleaning effectiveness by causing changes in membrane texture that hinder cleaning. In this section, we discuss these three possible causes for the difference in fouling propensity between RO and FO that are unrelated to foulant compaction by high feed pressure.

Future research should explore these and other possible explanations, identify the cause of high organic fouling reversibility in FO, and use this knowledge to enhance the fouling resistance of FO. Because this study has shown that low pressure is not necessary for high fouling resistance, it is possible that the cause of FO's fouling resistance can also be adapted to improve the fouling resistance of RO.

4.5.1 TMP

It is possible that TMP could have affected fouling reversibility in previous studies for reasons unrelated to foulant compaction by high feed hydraulic pressure. For example, without high TMP pressing a membrane against a permeate carrier, an FO membrane that has accumulated a foulant layer has the potential to "shake it off" [112] during cleaning. Membrane vibration has been used to remove fouling from RO membranes [113], so it is possible that FO membrane movement during normal cleaning could similarly enhance foulant removal. Additionally, TMP increases membrane roughness, as demonstrated by SEM and CLSM images of fouled FO membranes used with and

without TMP [98]. Increasing membrane roughness raises the contact area between foulant and membrane, and could potentially hinder foulant removal.

4.5.2 Solute back-diffusion

Diffusion of NaCl from the draw solution to the feed, which can significantly affect cake layer ion concentration [9, 97], may lead to differences in gel properties between FO and RO tests with alginate fouling and an NaCl draw due to the ion exchange reaction between sodium and calcium ions in alginate gels [114]. LeRoux et al. [115] measured compressive and shear moduli of alginate gels in calcium chloride solutions with and without sodium chloride and found that compressive and shear moduli decrease by 63% and 84%, respectively, due to the addition of 0.15 M sodium chloride. However, a difference in cleaning effectiveness between FO and RO has been observed even with a glucose draw solution [12], so NaCl back-diffusion alone cannot explain the disparity in fouling reversibility observed between FO and RO.

4.5.3 ICP and foulant heterogeneity

Fouling layers formed in FO tend to be more bumpy than those formed in RO. CLSM images show spatial heterogeneity in foulant thickness of both alginate fouling [12] and *Pseudomonas aeruginosa* biofouling [98] in FO alongside uniform-thickness layers formed in RO on the same membrane under identical hydrodynamic conditions. In another example of heterogeneous fouling in FO, optical micrographs of latex particle deposition on FO membranes (refer to Fig. 2b in [66]) show a pattern of particulate deposition with gaps where the membranes's support mesh filaments cross.

The reason for foulant layer heterogeneity in FO has not been previously explained, but could potentially result from spatially-varying local flux. Spatial variations in support layer mass transfer resistance may occur due to the heterogeneous pore structure and, where present, the embedded support mesh. Where the support layer mass transfer resistance is greater (e.g., where two mesh filaments cross), the local transmembrane flux will be smaller in FO. When the same membrane is used in

RO, the hydraulic resistance of the support layer is negligible relative to the resistance to flow through the active layer, and the local flux depends only on the properties of the active layer. Because of the influence of the support layer on flux in FO, the same membrane may have greater spatial variation in flux when used in FO than in RO. Higher local flux leads to greater convection of foulants (and, in the case of biofouling, nutrients) to the membrane and a locally thicker fouling layer. The potential for higher spatial variation in flux in FO may explain the observed heterogeneity of fouling layers formed in FO.

Fouling layer heterogeneity has the potential to affect ease of removal in several ways. A foulant layer with some thinner regions may break up more easily. Increased foulant layer roughness may allow high-velocity feed flow to create more lift. Variations in foulant layer thickness may create regions of stress concentration when the foulant layer swells or shrinks (e.g., due to changing ion concentration [13]) during a cleaning procedure, which may hasten detachment from the membrane. Further study is required to determine whether any of these proposed mechanisms have a significant effect on foulant removal.

4.6 Chapter conclusions

The effect of foulant compression on flux decline depends on the foulant cake pore size and feed osmotic pressure. According to the model developed here, compression of alginate foulant layers would be expected to increase the rate of flux decline at low salinity; however, at high salinity, compression would be expected to retard flux decline by reducing cake-enhanced concentration polarization. Model predictions were used to interpret the results of FO fouling experiments with both feed and draw streams at elevated pressure and determine the role of hydraulic pressure on fouling.

Higher hydraulic pressure did not result in the more rapid flux decline that was expected of compressible gels at the low feed salinity tested. In contrast to the trend identified by previous studies, which varied feed pressure and draw solution concentration together, the present study showed no effect of feed hydraulic pressure

on cleaning effectiveness. Furthermore, in situ visualization revealed no difference in foulant removal mechanisms over the range of pressures tested (0–40 bar). These results do not support the theory that high feed pressure compacts foulants and impedes membrane cleaning in RO.

Based on these results, foulant compaction by high pressure should no longer be considered the cause of the low fouling resistance of RO in comparison to FO. Several other differences between FO and RO may be responsible for the difference in these systems' fouling propensity. Future research should aim to pinpoint the cause of FO's fouling resistance and to apply this knowledge to improving the fouling resistance of both FO and RO.

Chapter 5

Comparison of fouling propensity between reverse osmosis, forward osmosis, and membrane distillation

This chapter is based on a paper by Tow et al. [116].

5.1 Introduction

Membrane fouling propensity is an important consideration in the development and operation of membrane desalination systems. Membrane distillation (MD) and forward osmosis (FO) are often claimed to be more fouling resistant than the widely used reverse osmosis (RO) desalination process. Fouling resistance is often used to justify the development and use of desalination processes with lower energy efficiency, particularly when desalinating water sources considered to have high fouling potential (see, e.g., Ref. [1]). Therefore, it is important to directly compare different desalination systems and understand how (and how much) their fouling behaviors differ. While fouling has been studied extensively in RO, FO, and MD systems individually, the present study undertakes the first direct comparison of MD against RO and FO operated under identical hydrodynamic conditions.

Figure 5-1 illustrates the working principles of RO, FO, and MD systems, all of

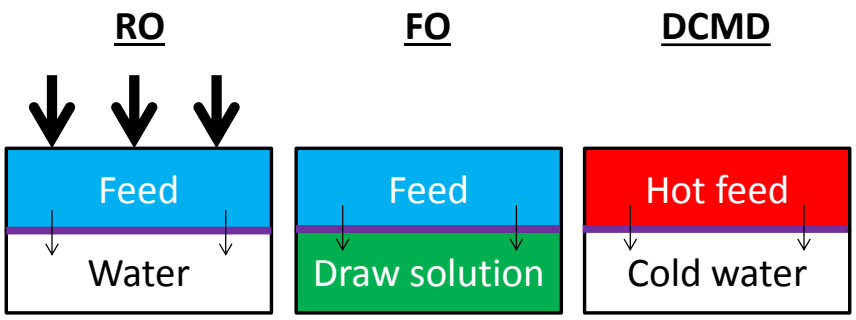

Figure 5-1: Schematic diagram of the operating conditions of desalination membranes in the systems considered: reverse osmosis (RO), forward osmosis (FO), and direct contact membrane distillation (MD). Thick arrows indicate high hydraulic pressure in RO.

which have the potential to suffer from fouling. RO desalination uses high hydraulic pressure (typically around 10–70 bar) that exceeds the osmotic pressure of the feed to drive nearly-pure water through a semipermeable membrane whose pores have radii on the order of 0.25 nm [106]. FO desalination uses membranes that are similar to RO membranes, but FO uses a draw solution of high osmotic pressure to pull water through the membrane without the application of high hydraulic pressure to the feed. For an FO system to produce pure water, an energy-intensive draw regeneration step is required [23]. Direct contact MD (DCMD) is a configuration of MD in which a microporous, hydrophobic membrane is in direct contact with both the feed and the permeate, as described in Ref. [117]. Water evaporates on the feed side of the MD membrane's pores and condenses on the permeate side. Of all the MD configurations, DCMD was chosen to represent MD in this study because, as in RO and FO, the membrane is in contact with liquid on both sides. In each system, water flows from the feed through the membrane, dragging with it microbes, dissolved solutes, and suspended solids that tend to accumulate near the membrane and form a fouling layer that degrades membrane performance.

MD and FO are generally thought to be more fouling resistant than RO, but no experiments have been conducted to directly compare MD to either RO or FO. A recent review [25] demonstrates that concerns about fouling on MD membranes

have historically been dismissed because of low system pressure, relatively large pore size and membrane hydrophobicity. MD is also frequently portrayed as a fouling-resistant process without specifying a physical reason [118, 119]. FO has been directly compared to RO in several studies including Refs. [9, 10, 11, 12, 13, 14, 97, 120], which have generally found that FO exhibits slower flux decline and is easier to clean. The smoothness and surface chemistry of cellulose triacetate (CTA) membranes as well as the low-pressure operation of FO are typically associated with its high fouling resistance. The effects of physical differences between RO, FO, and MD, including both membrane properties and operating conditions, on the fouling behavior of these systems are explored in Sec. 5.2.

In this study, we experimentally compare the fouling propensity of RO, FO, and DCMD using a single cross-flow desalination cell that can be configured for any of the three systems. Flow rates and initial permeate fluxes are kept constant across trials, but each system is operated at a typical operating temperature and pressure. Calcium sulfate is used as a model inorganic foulant and sodium alginate is used as a model organic foulant. Our findings indicate that FO tolerates a significantly higher calcium sulfate concentration without scaling than RO or MD. When scaling does occur, MD exhibits the most rapid flux decline. MD shows significant resistance to organic fouling with alginate relative to FO and RO, both of which perform similarly. Observed differences in fouling behavior are discussed in relation to the differing membrane properties and operating conditions of RO, FO, and MD desalination systems.

5.2 Differences in fouling propensity of RO, FO, and MD

RO, FO, and MD all use polymer membranes, but these membranes differ in chemical composition, surface roughness, pore size, support structure, and solvent transport mechanism. Effects on fouling of membrane surface properties are discussed in Sec. 5.2.1. The more subtle effects of the support layer structure and mechanism of solvent

transport are discussed in Sec. 5.2.4.

Differences in standard operating conditions between RO, FO, and MD may also affect fouling behavior. Transmembrane flux is a major driver of fouling due to its advection of foulants toward the membrane and compression of some foulant cakes. For that reason, initial flux is kept constant within each set of trials (inorganic and organic fouling) conducted in this study. However, fouling propensity may also be affected by two other operating conditions that inherently differ between these desalination processes: pressure and temperature. The effects of pressure and temperature on fouling are discussed in Secs. 5.2.2 and 5.2.3, respectively.

5.2.1 Effect of membrane surface properties

Membrane scaling risk depends on the nucleation induction time of supersaturated solutes in the feed and the residence time of the feed in the desalination system [121]. Nucleation induction time is related to the degree of supersaturation as well as the surface energy of the solution–membrane, solution–crystal, and crystal–membrane interfaces [122]. More hydrophobic surfaces such as MD membranes are more resistant to gypsum nucleation [122] than surfaces like thin-film composite (TFC) RO membranes, which are hydrophilic [123]. Mi and Elimelech [120] showed that CTA FO membranes are more easily cleaned of gypsum scaling than RO membranes. They also find that the adhesion energy between gypsum and cellulose acetate is lower than that of gypsum and polyamide (the active layer membrane material of most RO membranes), a difference which they attribute to complexation of Ca^{2+} with the carboxyl groups present on the surface of polyamide membranes. They hypothesize that this difference in adhesion energy leads to crystallization directly on polyamide membranes under the same conditions that lead to crystal formation in the bulk when using cellulose acetate membranes. These studies indicate that surface chemistry plays a role in the scaling resistance of FO and MD membranes relative to RO membranes.

The existence of macroscopic pores in MD membranes may also affect fouling. It has been claimed that the large pore size of MD membranes inhibits pore clogging

[124, 125, 126]. However, larger MD membrane pores also encourage pore wetting [124, 127] due to their lower liquid entry pressure. Pore wetting, which occurs when the feed solution enters the pores, can lead to solute permeation and significantly diminished permeate quality. In addition to cake layer formation, which affects RO and FO membranes, MD membranes are also susceptible to fouling inside their pores, which can both reduce water permeability and encourage pore wetting.

5.2.2 Effect of pressure

MD and FO are often considered to be less prone to fouling than RO because of their low operating pressure. However, theoretical modeling has shown that pressure alone does not affect fouling with incompressible foulants [12] such as inorganic scalants (e.g., gypsum) or hydrogel-forming polysaccharides (e.g., alginate [101]). Direct experimental comparisons at fixed flux between RO, FO, and pressurized FO have shown that operating these membrane systems at lower feed hydraulic pressure and higher draw osmotic pressure improves the susceptibility of the membranes to cleaning [9, 10, 11, 12]. However, a similar comparison of FO operated at low and high hydraulic pressure with the same flux and draw solution concentration showed no effect of pressure on flux decline rate or cleaning effectiveness [89, 111]. Previous studies [9, 10] have also hypothesized that the low operating pressure of FO allows the foulant layer to be more easily broken up during cleaning. However, recent studies have shown through in situ visualization that feed hydraulic pressure does not significantly affect mechanisms of alginate fouling removal [13, 89].

5.2.3 Effect of temperature

Temperature affects scaling by altering solubility, crystallization kinetics, and mass transfer. The solubility of a given salt in water depends on temperature, and calcium sulfate is often considered to have an inverse solubility (solubility that decreases with temperature). However, the strong inverse solubility does not begin until above approximately 60 °C, when crystallization of anhydrite ($CaSO_4$) outpaces crystallization

of gypsum ($CaSO_4 \cdot 2H_2O$) [128]. Gypsum increases in solubility with temperature until around 50 °C, after which its solubility decreases [129]. Increasing temperature also decreases the nucleation induction time at a given saturation index (see Eq. 5.2) [128, 130, 131], thus accelerating scaling. For this reason, the maximum calcium sulfate concentration that MD can tolerate without scaling has been shown, through modeling and experiments, to decrease with increasing feed temperature [121]. Finally, diffusion coefficients increase with increasing temperature, reducing concentration polarization and leading to a lower concentration (and less supersaturation) at the membrane.

Temperature also affects organic fouling. Kim et al. [132] experimentally tested the effect of feed and draw temperature on alginate fouling in FO, and they found that high feed temperature improves fouling performance by raising the diffusion coefficient of alginate, thereby facilitating alginate transport away from the membrane. High temperatures may also affect organic fouling through denaturation of proteins or depolymerization of polysaccharides, but alginate does not appear to depolymerize at temperatures up to 80 °C [133].[1]

5.2.4 Effect of solvent transport mechanism

Mechanisms of water transport determine the effect of fouling on each membrane's performance.[2] In FO and RO, water transport is driven by the hydraulic–osmotic pressure difference, $\Delta P - \Delta\pi$, where ΔP is the difference in pressure between the feed and draw or permeate sides of the active layer, and $\Delta\pi$ is the difference in osmotic pressure between the feed and draw or permeate sides [61]. RO has high hydraulic pressure on the feed side and has atmospheric pressure and negligible osmotic pressure on the permeate side. In FO, pressure is typically atmospheric in both feed and draw solutions, and the draw osmotic pressure is high. The porous support layer of the

[1] At the temperatures used in this study (up to 70 °C at the membrane module inlet), alginate gelation should therefore be possible. We determined that alginate gel does not melt in the MD temperature range used in this study by immersing a piece of alginate gel in water hotter than 70 °C for 10 minutes and boiling the gel for 5 minutes.

[2] Refer to She et al. [27] for details of transport in FO and RO and Summers et al. [134] for an explanation of water transport in DCMD.

FO membrane has significant mass transfer resistance [62], which causes internal concentration polarization (ICP) and limits the osmotic pressure differerence across the active layer of the membrane. Flux in MD is driven by a vapor pressure difference across the hydrophobic membrane's pores, which have a higher vapor pressure on the feed side due to the elevated temperature of the feed. The vapor pressure is also influenced by the feed solute concentration and the feed hydraulic pressure [135].

She et al. [27] review mechanisms flux decline due to membrane fouling in osmotic membrane desalination processes, including RO and FO. Although MD does not involve osmosis, some of their findings apply to MD fouling because MD membranes are also salt-rejecting. The formation of a porous cake on the surface of any desalination membranes causes flux decline through cake-enhanced concentration polarization, which raises the osmotic pressure at the membrane, as well as hydraulic drag, which lowers the hydraulic pressure at the membrane. At the low feed concentrations used in this study, the dominant driver of flux decline due to alginate fouling is hydraulic drag [14]. In the case of MD fouling, both cake-enhanced concentration polarization and hydraulic drag have the effect of reducing the vapor pressure at the membrane. Because a temperature difference exists between the feed and permeate, MD is also susceptible to cake-enhanced temperature polarization [25], i.e., fouling layer thermal resistance.

The effect on flux of a particular foulant cake depends on the mass transfer resistance through all layers of the membrane. Flux tends to decline more slowly in FO than in RO, even at the same initial flux, due to the effect of ICP on the overall mass transfer resistance of an FO membrane [14, 27, 97]. Heat and mass transfer through a fouled MD membrane has not, to our knowledge, yet been modeled, but we expect that the effect of foulant accumulation on flux decline in MD will differ from RO and FO because of the different transport mechanisms and resistance of the membrane. In particular, the effect of hydraulic pressure drop through the foulant layer on transport driving force is different in MD than in RO or FO. Based on Raoult's law and the Kelvin equation, Lee and Karnik [136] give an equation for the vapor pressure of water at a curved meniscus in a nanopore. Applying their equation to the pressure

drop created by viscous flow through a hydrophilic, nanoporous alginate gel, the ratio between the change in vapor pressure, ΔP_v, and the drop in hydraulic pressure across the gel layer, ΔP, is:

$$\frac{\Delta P_v}{\Delta P} = \frac{P_v V_m}{RT}, \tag{5.1}$$

where V_m is the molar volume of liquid water, R is the universal gas constant, and T is the meniscus temperature. At 25 °C, $\Delta P_v/\Delta P = 2.3 \times 10^{-5}$, so the change in vapor pressure at the membrane due to fouling is much smaller than the hydraulic pressure drop through the foulant. In MD, the vapor pressure difference that drives permeation is on the order of 0.1 bar, so a pressure drop of 1 bar through the foulant layer would lead to a change in vapor pressure driving force of <0.1%. On the other hand, the driving forces in RO and FO are on the order of tens of bars, so each bar of hydraulic pressure drop through the fouling layer has a significant effect on flux in RO and FO.

5.3 Methods

Fouling behavior was compared between the RO, FO, and DCMD processes using the same membrane module at the the same initial flux and cross-flow velocity. Each process was operated at a temperature (20–25 °C for RO and FO; for MD, 60 °C in the feed and 20 °C in the permeate loop, except where noted) and pressure (0 bar for FO and MD; 13.75–27.5 bar for RO) that is within the normal range for that technology. To compare the systems' tolerance of supersatuated solutions without scaling, the calcium sulfate feed concentrations at which scaling began to occur in each system were identified by conducting separate 36 h trials with different feed concentrations. Concentration and saturation index at the membrane were estimated from bulk properties using the heat and mass transfer models summarized in Sec. 5.3.3. The organic fouling propensity of the three processes was compared by recording the rate of flux decline during 18 h of operation with the same concentrations of sodium alginate and calcium chloride. The conditions of all experimental trials are listed in App. D.

5.3.1 Apparatus

Membranes were held in a plate-and-frame module within an experimental apparatus (Fig. 5-2) that could be operated as RO, FO, or DCMD. Both the feed and draw/permeate channels of the membrane module were 1 mm deep, 80 mm long, and 30 mm wide. Transmembrane flux was driven by high feed pressure in RO, high draw solution osmotic pressure in FO, and high feed temperature (and thus vapor pressure) in DCMD. Temperature, cross-flow velocities, and feed pressure were controlled while permeate mass was recorded to calculate flux and determine extent of fouling. Feed concentration was not actively controlled, but the feed volume was maintained within $\pm 5\%$ of the set point by periodically diluting the feed as it became concentrated. In FO, draw concentration declined over time due to permeation into the draw. The draw concentration and expected flux in the absence of fouling were calculated as a function of time from measurements of draw mass using the method described in [14].

The RO and FO configurations of the apparatus used in this study have been described in detail elsewhere [14]. The DCMD configuration was similar to FO, except that the draw was replaced with a cold permeate flow loop, and the feed temperature was raised by means of a heater to drive flux through the MD membrane. In DCMD, the permeate flow loop was initially filled with deionized water that had been partially degassed to prevent disruption of the flux measurement by outgassing. Feed temperature was controlled using an in-line cartridge heater based on a thermocouple reading just downstream of the membrane module. Permeate temperature was controlled using a cooling coil and thermocouple submerged in the permeate tank. After each MD experiment, the cartridge heater was removed and any accumulated scale was scraped off.

In all configurations, a 2 μm (nominal) cartridge filter was used to prevent large crystals from entering the membrane module and causing premature scaling, as demonstrated in Ref. [137]. Flux was calculated from the change in draw/permeate mass over time, which was measured with an Ohaus Scout Pro digital scale, using the RealTerm software package for data aquisition. The mass displaced by the submerged

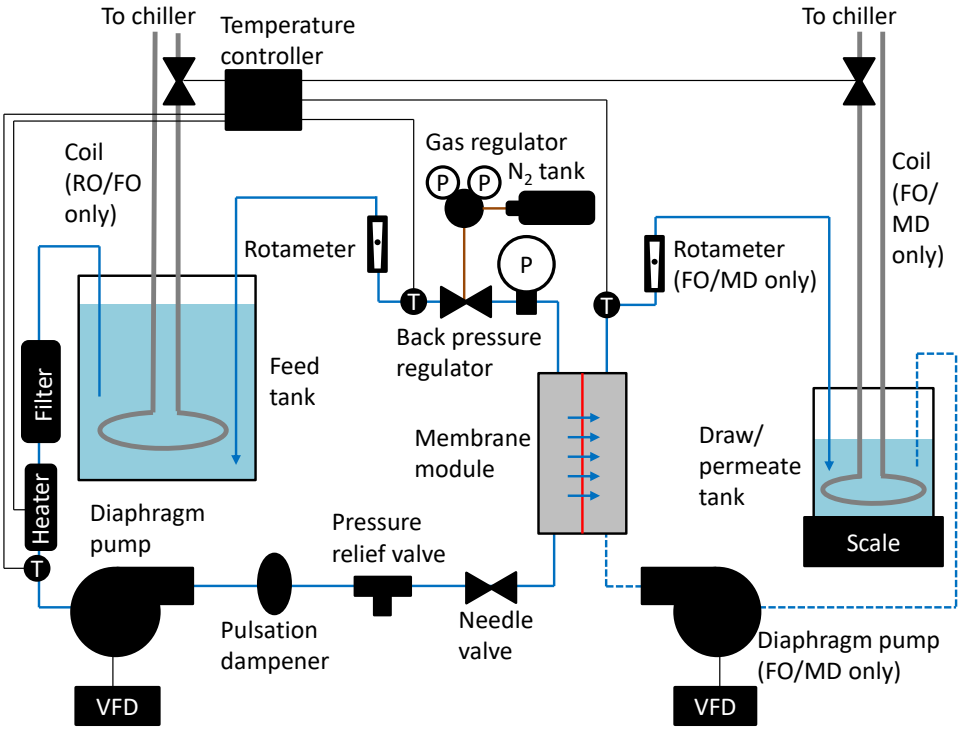

Figure 5-2: Schematic diagram of experimental apparatus that can be operated as RO, FO, or DCMD. Blue, black, and brown lines represent aqueous solutions, electrical wires, and nitrogen gas, respectively. Dashed lines represent flows present only in FO or DCMD. Figure adapted from Ref. [14] to reflect the apparatus used in this study.

cooling coil and draw/permeate inlet and outlet were accounted for in the FO and MD flux measurement. Flux is reported in Sec. 5.4 every 15 minutes from the change in draw/permeate mass during that time, except in MD. In MD, fluctuations in permeate production necessitate a fairly long flux measurement period of 30 minutes; however, flux is still reported every 15 minutes (in other words, the measurement periods in MD overlap by 50%).

Although the FO and DCMD configurations lack some external components required to produce water in real desalination systems, they are designed to simulate realistic conditions in the vicinity their respective desalination membranes for the purpose of studying fouling. A real FO desalination system would require a draw regeneration (and water production) system such as reverse osmosis. A real DCMD system would require a separate regenerator to recover heat from the permeate for feed preheating. However, these missing external components are not necessary for studying membrane fouling, which occurs where the desalination membrane contacts the feed solution.

Commercially-available membranes were used in all three systems. A new membrane sample was used for each trial. RO trials used polyamide thin film composite membranes (Dow FILMTEC SW30HR) designed for seawater applications. In FO, a cellulose triacetate FO membrane (Hydration Technology Innovations CTA-ES) was used. RO and FO membranes were prepared by soaking in 50% ethanol, 50% water mixture for 5 minutes and in deionized water for at least 30 minutes. The MD membranes were hydrophobic PVDF (Millipore ISEQ00010) with a nominal pore size of 0.2 μm and a water contact angle of 125° [121].

5.3.2 Fouling procedure

First, the system (RO, FO, or DCMD) was allowed to run free of foulants until reaching a steady permeate flux. Feed velocities were initially maintained above 10 cm/s. For the organic fouling tests, 50 mM sodium chloride was added to the feed tank to provide a baseline feed salinity. In DCMD, the feed stream was raised to the desired temperature (60 °C at the feed channel outlet) while the cold stream was

maintained at 20 °C. In RO, the pressure was adjusted to achieve the desired initial flux. In FO, a draw solution of sodium chloride in deionized water is used to drive flow, and the sodium chloride concentration is adjusted until the desired initial flux is achieved. Each system was run for at least 2 h and until a steady flux was reached before adding foulants.

To instigate inorganic fouling, the feed was caused to be supersaturated with calcium sulfate. As in Ref. [121], supersaturated calcium sulfate feed solution was prepared by adding concentrated calcium chloride solution and concentrated sodium sulfate solution (both mixed by mass from ACS grade powders from Sigma-Aldrich and EMSURE, respectively) at least ten minutes apart. As a result of the salts used, the Na^+ and Cl^- concentrations in each feed solution were equal to twice the calcium sulfate concentration. After chemical addition, the feed cross-flow velocity was reduced to 5 cm/s to encourage fouling; for the same reason, no feed spacer was used. A pulsation dampener was used in the feed loop to smooth the feed flow rate. In FO and DCMD, the draw/permeate stream was also maintained at 5 cm/s and the channel was filled with two stacked non-woven spacers (Sterlitech 17 mil diamond). The use of a pulsation dampener in the draw and MD permeate streams would have disrupted the flux measurement; however, without a pulsation dampener, the reciprocating diaphragm pump caused fluctuations in draw/permeate flow rate in FO and MD at a frequency of approximately 3 Hz. Once foulants were added, the apparatus maintained constant temperatures, pressures, and (time-averaged) flow rates for 36 h or until flux decline indicated that fouling had clearly occurred. Feed concentration was maintained within approximately ±5% of the desired concentration by periodically diluting it to its initial volume. However, in a few highly supersaturated trials, some crystallization occurred in the feed tank, reducing the feed concentration. For the purpose of comparing RO, FO, and MD, scaling was determined to have occurred if flux declined to 80% of initial flux (90% in FO, which generally exhibits slower flux decline while fouling [14, 97]) within the 36 h trial period.

To instigate organic fouling, concentrated sodium alginate solution (mixed from powdered sodium alginate, Sigma A2033) was added to bring the feed up to a final

concentration of 200 mg/L after the system reached a steady flux. Calcium chloride was then added to bring the feed concentration to 1 mM and encourage gelation of the alginate as it concentrated at the membrane (see, e.g., [81]). Fouling was carried out for 18 h at constant temperature, pressure, and flow rate to enable comparison of flux decline rate. After 18±0.5 h, the membrane was removed and a small (approximately 6 cm^2) panel was cut from the active area and lightly blotted with a tissue, using only surface tension to hold the tissue to the fouled membrane panel. Once blotted, the gel was then peeled off the membrane wth the aid of a razor blade and weighed to determine the gel mass per unit area. After weighing, the gel was air-dried and weighed again to determine the dry mass.

5.3.3 Predicting conditions at the membrane

Crystals have the potential to form when the solution is supersaturated with respect to any salt anywhere in the feed, but crystallization is likely to occur first near the membrane where, due to concentration polarization, the solution is most concentrated. Therefore, estimating conditions close to the membrane is necessary to interpret results of the inorganic fouling trials. With the $CaCl_2$–Na_2SO_4 mixtures used in this study, calcium sulfate is the most likely scalant [37]. Gypsum (calcium sulfate dihydrate) is the most likely form of calcium sulfate to crystallize in the range of temperatures used in this study (20–60 °C), although anhydrite precipitation could also occur at the higher temperatures used in the MD trials [128]. The concentration of calcium sulfate with respect to gypsum saturation is quantified with the saturation index, SI, which is defined in Eq. 5.2:

$$\mathrm{SI} = \log_{10}\left(\frac{a_{Ca^{2+}}\, a_{SO_4{}^{2-}}\, a_w^2}{K_{sp}}\right), \tag{5.2}$$

where $a_{Ca^{2+}}$, $a_{SO_4{}^{2-}}$, and a_w denotes the activity of calcium, sulfate, and water, respectively, and K_{sp} is the solubility product for calcium sulfate dihydrate. When SI $= 0$, the solution is saturated with respect to gypsum, and when SI > 0, the solution is supersaturated.

Gypsum saturation index is calculated from ion concentrations (including sodium and chloride) and solution temperature using PHREEQC (USGS) with the PHREEQC database[3]. For calculation of the saturation index near the membrane, where the concentration is highest and crystallization is most likely, the concentration and temperature near the membrane are determined as described in the following two sections.

Concentration polarization

The calcium sulfate concentration at the membrane can be estimated from from film theory. The recovery ratio (defined as the ratio of permeate flow rate to feed flow rate) of the module is very low ($< 1\%$), so the bulk concentration can be considered to be constant throughout the length of the module. Assuming that calcium and sulfate diffuse together (i.e., neglecting the effects of sodium and chloride transport on calcium and sulfate transport) and that the membrane rejection is perfect, the average calcium sulfate concentration at the membrane, $\overline{C}_m$, can be expressed as a function of the concentration of the feed at the module inlet, C_f, average (measured) permeate flux, $\overline{J}_w$, and average mass transfer coefficient in the feed, $\overline{k}_f$, using stagnant film theory (see, e.g., [62]):

$$\overline{C}_m = C_f \exp(\overline{J}_w/\overline{k}_f). \tag{5.3}$$

Although the mass transfer coefficient varies along the length of the membrane as the mass diffusion boundary layer develops, we use an average mass transfer coefficient to characterize the concentration at the membrane in each coupon-scale test. The average mass transfer coefficient is calculated from a mass transfer analogy of a Nusselt number correlation [138] for hydrodynamically fully-developed flow between parallel plates with a uniform wall temperature:

$$\overline{\mathrm{Sh}}_{D_h} = 7.54 + \frac{0.03(D_h/l)\mathrm{Re}_{D_h}\mathrm{Sc}}{1 + 0.016((D_h/l)\mathrm{Re}_{D_h}\mathrm{Sc})^{2/3}}, \tag{5.4}$$

[3]We also calculated SI using the Pitzer database, and the SIs calculated using the two databases were within 10% of one another.

where $\overline{\mathrm{Sh}}_{D_h} = \overline{k}_f D_h / D_s$ is the average Sherwood number, D_h is the hydraulic diameter (approximated as twice the channel thickness due to this channel's large width:thickness ratio), D_s is the calcium sulfate diffusion coefficient, $\mathrm{Re} = vD_h/\nu$ is the Reynolds number, u is the bulk velocity, ν is the kinematic viscosity of the solution, l is the channel length, and $\mathrm{Sc} = \nu/D_s$ is the Schmidt number. The diffusion coefficient of calcium sulfate at infinite dilution (used here because of the low feed concentrations used in these experiments) is calculated from ion diffusion coefficient data from Li and Gregory [139] as 9.11×10^{-10} m^2/s at 25 °C. Diffusion coefficients at 20 °C and 58.5 °C (the temperatures at the membrane on the feed side in the gypsum scaling tests; see Sec. 5.3.3) are calculated using the Stokes-Einstein equation as 7.96×10^{-10} m^2/s and 1.89×10^{-9} m^2/s, respectively.

Membrane temperature

In RO and FO, the temperature at the membrane is approximately equal to the feed temperature. However, in DCMD, a temperature difference exists between the bulk liquid and the liquid at the membrane due to heat transfer through the membrane. Additionally, evaporation of water from the feed causes a streamwise temperature drop. Gypsum saturation concentration is not strongly dependent on temperature in the 60 °C ± 10 °C range, so approximate values of average temperature are sufficient to predict saturation indexes in MD trials.

Near-membrane temperature is modeled with a simplified version of the DCMD model developed by Summers et al. [134], utilizing the measured average permeate flux rather than a fitted membrane permeability. In the present, simplified model, both permeate flux and heat transfer coefficients are treated as uniform along the length of the module, and the calculated temperatures represent approximate average temperatures of the bulk feed and the feed at the membrane.

Heat is considered to transfer from the feed to the membrane surface by convection, through the membrane by conduction, and then to the permeate stream by convection. Heat transfer rates inside and outside the membrane are unequal due to the evaporation of water at the feed side of the membrane and condensation at the

permeate side, as described by Eq. 5.5:

$$\overline{h}_f(\overline{T}_{f,b} - \overline{T}_{f,m}) = \overline{h}_p(\overline{T}_{p,m} - \overline{T}_{p,b}) = \rho_p \overline{J}_w h_{fg} + \frac{k_m}{\delta_m}(\overline{T}_{f,m} - \overline{T}_{p,m}) \tag{5.5}$$

where $\overline{h}$ is the average heat transfer coefficient, $\overline{T}$ is the average temperature, ρ is the liquid density, h_{fg} is the latent heat of vaporization of water, k is the thermal conductivity, δ is the thickness, and subscripts f, p, b, and m denote feed, permeate, bulk, and membrane, respectively. The equations above can be solved for the average temperature at the membrane on the feed side by eliminating $\overline{T}_{p,m}$:

$$\overline{T}_{f,m} = \frac{\overline{h}_f(1 + \frac{k_m}{\delta_m \overline{h}_p})\overline{T}_{f,b} + \frac{k_m}{\delta_m}\overline{T}_{p,b} - \rho_p \overline{J}_w h_{fg}}{\overline{h}_f(1 + \frac{k_m}{\delta_m \overline{h}_p}) + \frac{k_m}{\delta_m}}. \tag{5.6}$$

The membrane thermal conductivity k_m is estimated to be 0.06 W/m-K using a porosity of 0.8 [134] and assuming 1-D conduction through a PVDF slab with straight-through pores containing air. Average heat transfer coefficients in the feed and permeate ($\overline{h}_f$ and $\overline{h}_p$) are calculated using a Nusselt number correlation for hydrodynamically-developed, laminar flow between flat plates at constant temperature [138]:

$$\overline{\mathrm{Nu}}_{D_h} = \frac{\overline{h} D_h}{k_w} = 7.54 + \frac{0.03(D_h/l)\mathrm{Re}_{D_h}\mathrm{Pr}}{1 + 0.016[(D_h/l)\mathrm{Re}_{D_h}\mathrm{Pr}]^{2/3}}, \tag{5.7}$$

where $\overline{\mathrm{Nu}}_{D_h}$ is the Nusselt number, k_w is the thermal conductivity of water, and Pr is the Prandtl number of water. Because saturation index is not strongly temperature dependent in the 60 °C range and thus a precise calculation of membrane temperature is not required, the effect of the non-woven spacers in the permeate channel on permeate-side heat transfer coefficient is neglected in this analysis.

The axial temperature changes in the hot and cold channels (ΔT) are also calculated to relate the average bulk temperatures in Eq. 5.6 to the known feed outlet and permeate inlet temperatures. The flow rates of feed and permeate were set equal in this experiment; for the purpose of this estimation, we neglect small changes in channel cross-flow rate due to permeation, differences in density or heat capacity be-

tween channels due to temperature and concentration differences, and heat exchange with the environment through the module walls. Therefore, the axial decrease in feed temperature, ΔT, is approximately equal to the increase in permeate temperature. Approximating the heat transfer rate per unit width into the permeate channel as $\dot{Q}' = \overline{h}_f(\overline{T}_{f,b} - \overline{T}_{f,m})l$, the permeate temperature increase is:

$$\Delta T = \frac{\dot{Q}'}{\delta_c v \rho_p c_p} = \frac{\overline{h}_f(\overline{T}_{f,b} - \overline{T}_{f,m})L}{\delta_c v \rho_p c_p}, \tag{5.8}$$

where $\delta_c = D_h/2$ is the channel thickness and c_p is the specific heat capacity of water. The average bulk feed and permeate temperatures can then be estimated from the measured values at the feed outlet ($T_{f,\text{out}}$) and permeate inlet ($T_{p,\text{in}}$):

$$\overline{T}_{f,b} = T_{f,\text{out}} + \Delta T/2 \tag{5.9}$$

$$\overline{T}_{p,b} = T_{p,\text{in}} + \Delta T/2 \tag{5.10}$$

Equations 5.6–5.10 are solved simultaneously in MATLAB to estimate average feed temperatures in the bulk and near the membrane. For the experiments conducted in this study, the estimated average feed temperatures in the bulk and near the membrane were 63.9–64.6 °C and 58.4–58.6 °C, respectively. In this temperature range, the saturation concentration (calculated using PHREEQC) varies less than 0.4 %/°C, which indicates that differences in SI throughout the channel are primarily driven by concentration polarization, not temperature variation.

5.4 Results and discussion

5.4.1 Inorganic fouling

RO, FO, and DCMD were operated at typical temperatures (20, 20, and 60 °C, respectively[4]) with feeds of various concentrations to determine the maximum calcium

[4]Exception: One MD trial (27 mM $CaSO_4$) had a particularly low initial flux, so the permeate-side temperature was reduced from 20 °C to 18 °C to slightly augment flux without significantly

sulfate concentration and gypsum saturation index that each system can tolerate without fouling. RO pressure and FO draw concentration were adjusted before fouling to match, as closely as possible, the initial fluxes measured in the MD trials. Operating parameters for all trials are included in App. D.

Flux decline measurements for the RO trials at various feed calcium sulfate concentrations are shown in Fig. 5-3. Flux measurements are normalized by initial flux. The 29 mM trial exhibited rapid flux decline and the 24 mM trial showed a transition to rapid flux decline after approximately 13 h. The delay in rapid fouling at 24 mM may relate to the induction time for calcium sulfate nucleation (see, e.g., [128]), which increases with decreasing SI. In trials with concentrations of 22 mM and lower, flux declined gradually during the 36 h of operation. The slow flux decline was most likely due to membrane compaction over time, which has been previously recorded by McGovern et al. [140]. To check for signs of fouling in these lower-concentration trials, the membrane from the highest-concentration trial that did not have rapid flux decline (22 mM) was removed after the experiment and allowed to dry, revealing needle-like crystals around the edges of the membrane where it is clamped into the module. However, the active area of membrane appeared to be free of crystals except for small patches of crystal growth near stagnation points at the channel outlet, and this was considered to be a non-fouling result. The set of RO experiments shown in Fig. 5-3 shows that the transition to fouling occurred between feed calcium sulfate concentrations of 22 and 24 mM.

Figure 5-4 shows the normalized flux for all FO trials with calcium sulfate. Here, flux is normalized by the predicted flux in the absence of fouling using the method outlined in [89] to account for dilution of the draw solution over time. Flux declined significantly in trials with at least 36 mM $CaSO_4$ in the feed, whereas no fouling occurred in trials with up to 29 mM $CaSO_4$ in the feed. Fouling results determined from flux decline were corroborated by visual inspection of the membranes, which were covered with a loosely-attached layer of crystals in the 36 mM and 43 mM trials. In the 43 mM trial, which was significantly supersaturated in the bulk feed,

changing feed-side conditions.

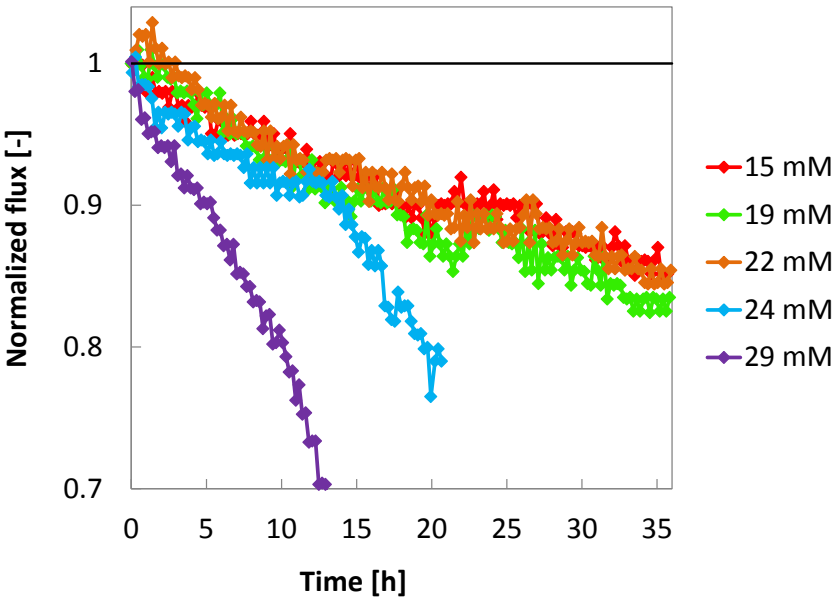

Figure 5-3: Flux decline in RO with various feed concentrations of calcium sulfate (given in the legend). Initial flux was 19.5±0.2 lmh.

crystallization occurred not only on the membrane, but in the feed tank, tubing, and instrumentation, clogging a rotameter and causing a spike in feed hydraulic pressure and the rise in flux around 10 h; when the feed was returned to atmospheric pressure around 16 h, flux dropped rapidly. From these trials, we determined that the transition to fouling in FO occurred between 29 and 36 mM.

Figure 5-5 shows the measured flux decline for all MD trials conducted with calcium sulfate. Flux is normalized by initial flux. Trials with feeds of 29 and 36 mM calcium sulfate exhibited a dramatic decline in flux within the first few hours, whereas trials with 24 and 27 mM declined less than 10% during the 36 h test period. As with RO, the membrane was removed after the most supersaturated non-fouling trial (27 mM) and dried; again, crystals were largely confined to the clamped region outside the active area and, to a lesser extent, the channel outlet stagnation point. A few individual needles were scattered throughout the active area; these may have formed during the trial without significantly affecting flux, or they may have formed while the membrane dried in air after removal from the membrane module. In contrast, the fastest-fouling membrane was carpeted in crystals when it was removed after just

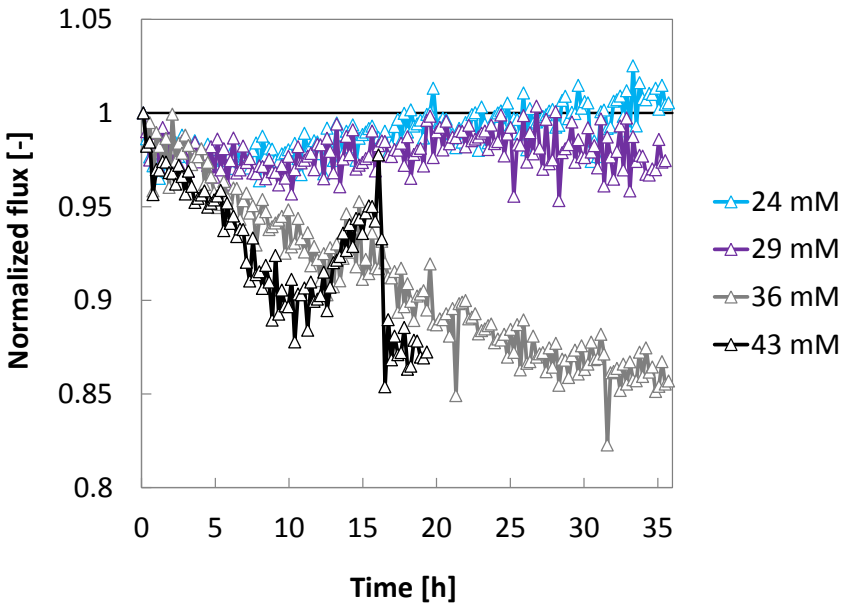

Figure 5-4: Flux decline in FO with various feed concentrations of calcium sulfate (given in the legend). Initial flux was 19.6±0.6 lmh in all trials.

3 h. The stark difference in fouling behavior (in terms of both crystal accumulation and flux decline rate) places the transition to fouling between feed concentrations of 27 and 29 mM for MD.

Figure 5-6 shows the relative resistance to calcium sulfate fouling of RO, FO, and MD. The maximum concentration tolerated by each system without fouling was determined from the experiments shown in Figs. 5-3 through 5-5. The error bars show the range between the highest concentration that did not foul and the lowest concentration that did foul. Saturation indexes were calculated with PHREEQC. The concentration and saturation index at the membrane, which are larger due to concentration polarization, were estimated as described in Sec. 5.3.3. Because channel thickness and length have been shown to affect scaling propensity [121] in MD, the values of concentration and saturation index that can be sustained without fouling are specific to this experimental apparatus with its particular channel dimensions. However, these results allow us to discuss the relative performance of these three processes.

Figure 5-6 shows that FO tolerated a significantly higher calcium sulfate concen-

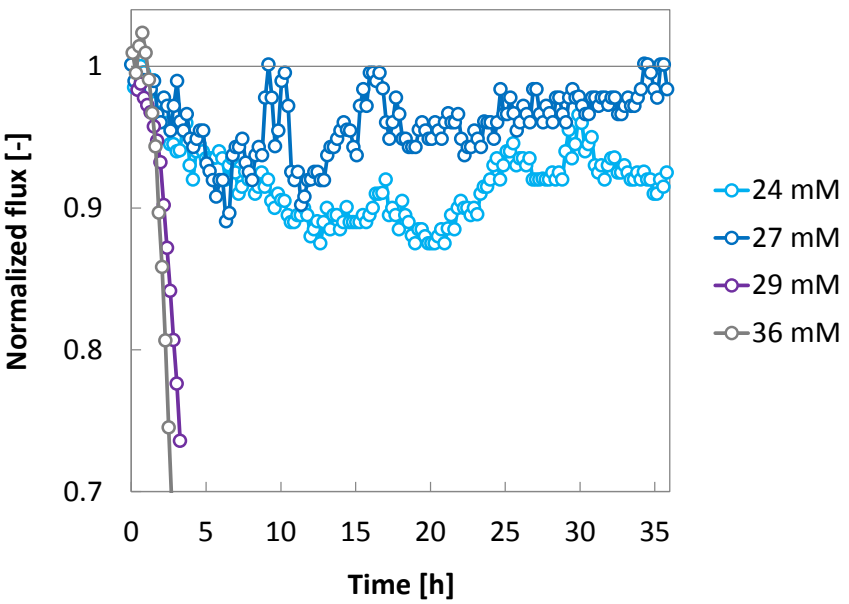

Figure 5-5: Flux decline in MD with various feed concentrations of calcium sulfate (given in the legend). Initial flux was 18.6±2.3 lmh in all trials.

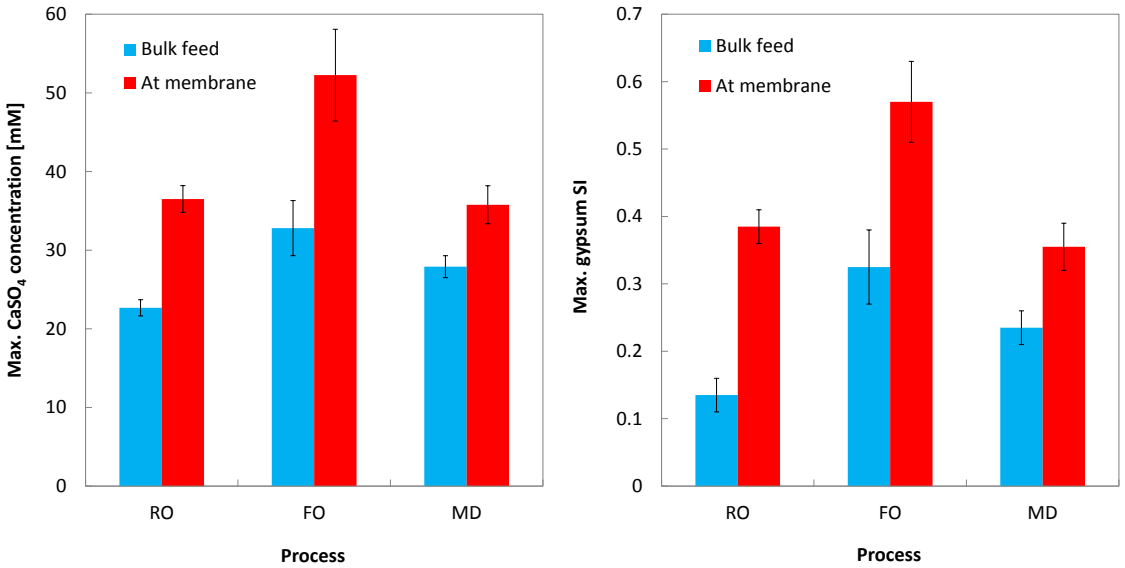

(a) Concentration

(b) SI

Figure 5-6: Maximum (a) calcium sulfate concentration and (b) gypsum SI without fouling in RO, FO, and MD. SI is defined in Eq. 5.2 and SI > 0 indicates a supersaturated solution. MD tolerates a slightly more concentrated (and more supersaturated) feed without fouling. Error bars represent the range between the lowest concentration that caused fouling and the highest concentration that did not.

tration and gypsum SI both in the feed and at the membrane than either RO or MD. MD tolerated a slightly higher feed concentration than RO, but the maximum concentration at the membrane was roughly the same between these two systems. Because gypsum saturation concentration is not strongly dependent on temperature in the 20–70 °C range, saturation indexes (shown in Fig. 5-6b and defined in Eq. 5.2) show the same trend as concentrations (Fig. 5-6a). Notably, all three systems tolerated a somewhat supersaturated feed for 36 h without scaling.

Differences in supersaturation tolerance between systems shown in Fig. 5-6 may be explained by the differences in membrane chemistry between FO, RO, and MD systems as well as the effect of temperature on nucleation induction time, as discussed in Sec. 5.2. Based on surface chemistry alone, FO and MD would be expected to have better fouling resistance than RO [120, 122]. However, the high temperature of the MD feed reduces the nucleation induction time for a given supersaturation, significantly reducing the SI at which fouling occurs [121]. MD's high temperature does reduce concentration polarization, allowing MD to tolerate a slightly more supersaturated feed than RO, even though their tolerance of supersaturation at the membrane is approximately equal. Overall, favorable surface chemistry and low-temperature operation give FO a significant advantage in gypsum scaling resistance relative to both RO and MD.

Because shifts in water composition or operating conditions may trigger fouling, the response of a membrane to fouling is an important aspect of its fouling behavior. Figure 5-7 highlights differences in fouling behavior between the three systems by comparing flux decline data shown in Figs. 5-3 through 5-5 at three calcium sulfate concentrations. At 24 mM, only the RO membrane fouled. At 29 mM, both RO and MD membranes fouled; however, even though MD tolerated a higher concentration than RO without fouling, the rate of flux decline at 29 mM was much greater in MD than in RO. At 36 mM, both FO and MD membranes fouled[5], but the rate of flux decline was significantly higher in MD than in FO. The severity of MD's performance decline after the onset of fouling should be taken in to consideration when choosing

[5]RO was not tested at 36 mM because it began fouling at a much lower concentration of 24 mM.

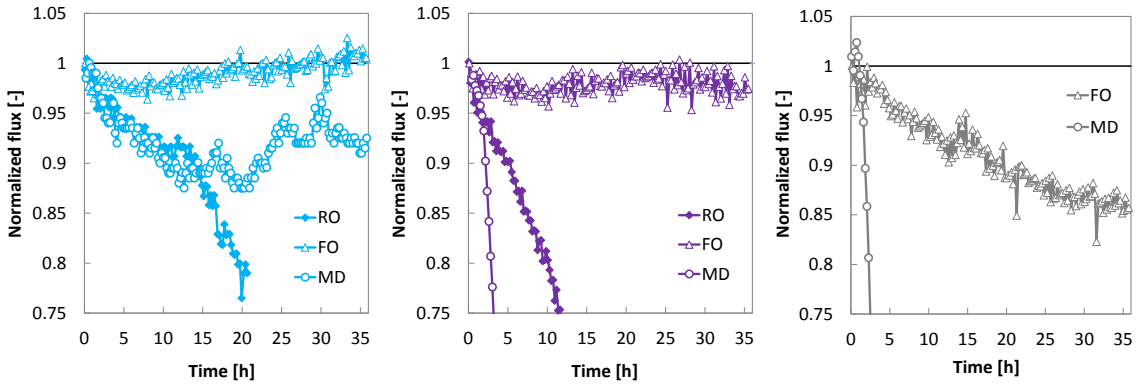

(a) 24 mM (b) 29 mM (c) 36 mM

Figure 5-7: Comparison of flux decline behavior between different processes at three calcium sulfate feed concentrations. Initial flux was 19.5±0.7 lmh.

a desalination process to treat supersaturated water sources.

Disparities in flux decline rate after fouling between MD and the osmotic membrane systems can be attributed to differences in operating temperature and fouling mechanisms, as previously discussed in Sec. 5.2. In contrast to multi-stage flash (MSF) and multi-effect distillation (MED), which minimize scaling by separating the evaporating interface from solid surfaces, MD places the evaporating interface in direct contact with the most sensitive part of the membrane: the pore. Scale formation at the pore entrance is therefore likely. The effect of scale formation at the MD pore entrance may also differ from the effect of scale on top of an RO or MD membrane due to the different water transport mechanisms of these processes. The faster crystallization kinetics at high temperature (see, e.g., [128]) may also contribute to the rapid flux decline of scaled MD membranes.

The low rate of flux decline in FO after fouling appears to be primarily related to the FO membrane's scaling-resistant surface chemistry. The rate of flux decline in FO at 36 mM $CaSO_4$ (Fig. 5-7c) is lower than in RO at 29 mM (Fig. 5-7b), even though the foulant concentration in the FO trial is higher. FO and RO differ in their response to the accumulation of equivalent foulant layers [14] due to different levels of membrane mass transfer resistance, and it is expected that RO flux would decline slightly more for the same accumulation of crystals, but the stark difference in flux

decline rate is well beyond what can be explained by the ICP self-compensation effect. However, slow flux decline may be related to the FO membrane's resistance to crystal nucleation, which was demonstrated by Mi and Elimelech [120]. The crystallization-resistant FO membrane surface may reduce the area fraction of crystal–membrane contact when scaling does occur, keeping more of the membrane surface active and perhaps even enhancing removal of loosely-attached crystals through shear-induced diffusion or inertial lift (see, e.g., [141]).

5.4.2 Organic fouling

Measurements of the flux decline resulting from alginate fouling in RO, FO, and MD are presented in Fig. 5-8a along with exponential fits of flux decline (Eqs. 5.11, 5.12, and 5.13 for RO, FO, and MD, respectively).

$$J^*_{\mathrm{RO}} = 1 - 0.46\Big[1 - \exp\Big(\frac{t}{12600\ [\mathrm{s}]}\Big)\Big] \tag{5.11}$$

$$J^*_{\mathrm{FO}} = 1 - 0.48\Big[1 - \exp\Big(\frac{t}{18000\ [\mathrm{s}]}\Big)\Big] \tag{5.12}$$

$$J^*_{\mathrm{MD}} = 1 - 0.14\Big[1 - \exp\Big(\frac{t}{4500\ [\mathrm{s}]}\Big)\Big] \tag{5.13}$$

J^* is the normalized flux, or ratio of flux to initial flux. The exponential flux decline is derived from a deposition-minus-removal model of heat exchanger fouling that has been applied to reverse osmosis fouling [88]; validation of this model for fouling in FO and MD are not known to the authors, but the agreement with the shape of the experimental flux decline curves is reasonable.[6]

Figure 5-8a and Eqs. 5.11–5.13 show that the three systems foul with different time constants and approach different normalized fluxes. Although the initial rate of flux decline is fairly similar between all three systems, MD quickly reaches an asymptotic flux of 14.5 lmh, whereas RO and FO have longer time constants and end at similar fluxes of 9.2 lmh and 9.9 lmh, respectively. The slower flux decline of RO

[6]The exponential flux decline seen with organic fouling of all three membranes (Fig. 5-8) does not match the progression of gypsum scaling shown in Figs. 5-3–5-5.

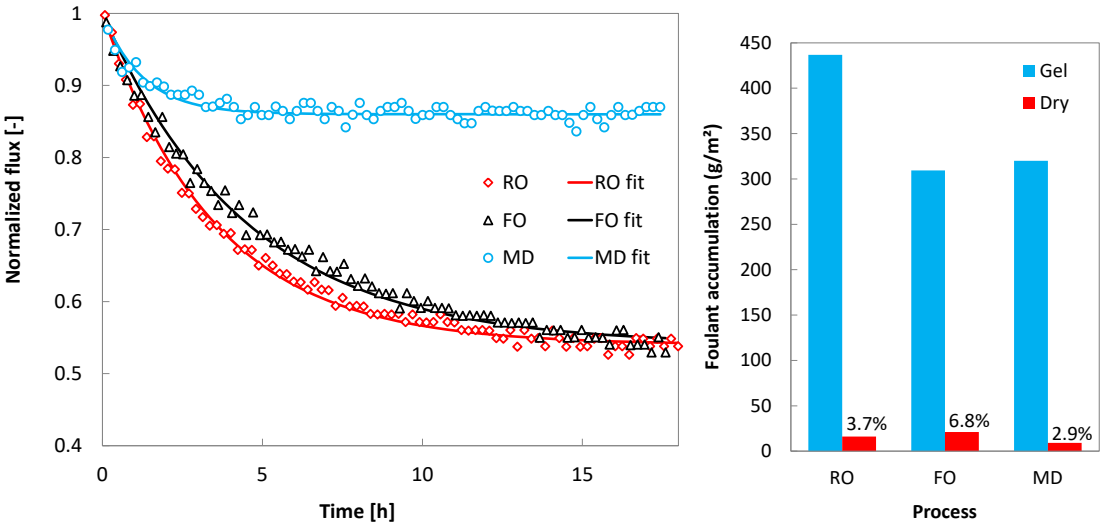

(a) Flux (b) Accumulation

Figure 5-8: Comparison of (a) flux decline (with exponential fits, Eqs. 5.11–5.13) and (b) foulant accumulation in RO, FO, and MD due to alginate fouling in the presence of calcium (1 mM $CaCl_2$) with 50 mM NaCl. Initial flux was 17.7±1.0 lmh.

relative to FO is expected based on FO's ICP self-compensation effect [14, 27, 97], and the comparable asymptotic flux is expected given the identical feed composition, temperature, and hydrodynamic conditions according to the critical flux model [100].

The significant increase in asymptotic flux in MD relative to RO and FO trials with the same feed composition (and thus the same foulant advection rate at a given flux) requires a larger foulant removal rate in MD. Given the small size (on the scale of nm [141]) of organic macromolecules such as alginate, Brownian diffusion is likely to be the dominant removal mechanism [141]. Therefore, high temperature contributes to a larger foulant removal rate by increasing the diffusion coefficient of alginate. Using the Stokes-Einstein equation and the temperature dependence of the viscosity of pure water, the diffusion coefficient of alginate can be estimated to increase by a factor of 2.08 between 25 °C and 58.5 °C, which are the temperatures in the feed close to the membrane in FO/RO and MD, respectively. According to Ref. [141], this difference in diffusion coefficient should lead to an increase in Brownian diffusion rate by a factor of 1.75 between 25 °C and 58.5 °C, assuming constant alginate concentration in the gelled foulant layer. This estimate corresponds to an increase in asymptotic flux from

9.2 lmh in RO to 16.0 lmh in MD, which is close to the 14.5 lmh asymptotic flux measured in MD.

Figure 5-8b shows the mass of alginate gel deposited on the membranes as well as the dry mass of that gel measured after several weeks of air drying. The dry mass of the gel collected in the FO trial was greater than that of the RO trial, as would be expected given its slower flux decline and higher average flux, which brings more alginate to the membrane [14]. However, the measured mass of gel on the FO membrane was the smallest of the three membranes. Our method of measuring foulant accumulation is not very accurate in the FO process, as the time spent blotting the foulant may allow the draw solution contained in the support layer to pull water from the gel by osmosis. For this reason, the gelled foulant thickness measurement in FO may not be meaningful. The quantity of foulant accumulation (both as gel and dry mass) was almost as high in MD as in RO, despite the high asymptotic flux of MD. Accumulated alginate gel does not affect water flux as much in MD as in RO or FO because of the limited effect of hydraulic pressure drop through the foulant on vapor pressure, as shown in Eq. 5.1. However, the cake thickness in the MD trial (estimated from gel mass) was comparable to the thermal boundary layer thickness (estimated using Eq. 5.7), and so cake-enhanced temperature polarization [142, 143] contributed significantly to the observed flux decline in MD.

5.5 Chapter conclusions

The fouling propensity of RO, FO, and MD were compared using a single membrane module to simulate each type of desalination under identical hydrodynamic conditions. When filtering solutions containing sodium alginate, MD membranes exhibited significantly less flux decline (14%) than RO or FO membranes (46% and 47%, respectively) due to the increase in diffusion coefficients with temperature. When calcium sulfate solutions were used, all three systems operated under somewhat supersaturated conditions for 36 hours without scaling. Scaling began at significantly higher concentrations in FO (46–58 mM at the membrane) than in RO or MD (35–38 mM

in RO and 33–38 mM in MD), which may be explained by the low surface energy of CTA membranes and effect of temperature on crystallization kinetics. When gypsum scaling did occur, it triggered a much more rapid flux decline in MD than in RO or FO.

Relative to RO, both FO and MD exhibited a significant advantage in fouling resistance when exposed to a particular type of foulant. MD performed very well with alginate and FO tolerated a significantly supersaturated calcium sulfate solution. However, most water and wastewater streams are complex, and desalination systems must be able to tolerate a range of potential foulants. The observed differences in fouling behavior should be considered when choosing desalination processes for specific applications, but they should not outweigh considerations of energy consumption and overall cost.

Chapter 6

In situ visualization of organic fouling and cleaning mechanisms in reverse osmosis and forward osmosis

This chapter is based on a paper by Tow, Rencken and Lienhard [13].

6.1 Introduction

Understanding mechanisms of fouling and cleaning in membrane desalination is crucial for improving membrane technology and designing more targeted pretreatment and cleaning strategies. Both low salinity and seawater desalination applications suffer from organic fouling, which includes fouling with gel-forming polysaccharides [78]. Sodium alginate is often used as a model polysaccharide because of its similarity to extracellular polymeric substances (EPS) found in membrane fouling [79]. Alginate fouling has been studied extensively, particularly in terms of flux decline and cleaning effectiveness, but few studies have investigated mechanisms of foulant removal. Therefore, in this work, we study mechanisms of alginate fouling accumulation and removal in reverse osmosis (RO) and forward osmosis (FO) through both flux measurement

and in situ visualization.

Visualization of membrane fouling serves two main purposes: to quantify fouling and to enhance understanding by complementing quantitative measurements. Methods such as nuclear magnetic resonance imaging have been used to measure fouling in situ, but the choice of imaging methods is limited by the materials compatible with the high pressures of RO [144]. Ultrasonic time-domain reflectometry (UTDR) can work through a thick enclosure and has been successfully used to monitor inorganic fouling of RO membranes in situ [144]. Changes in the ultrasonic response of the membrane can be used to calculate foulant thickness [145]. Such quantitative visualization methods have the potential to monitor fouling in real desalination plants, but they have limitations. UTDR, for example, can only provide the foulant thickness at the measurement location, but no information about morphology or patterning. In contrast, qualitative imaging can demonstrate or confirm fouling mechanisms that underlie predictive models.

Several previous studies have used in situ visualization specifically to elucidate mechanisms of fouling and cleaning. Li et al. [146] visually demonstrated the phenomenon of critical flux in microfiltration using latex beads of 3-11.9 μm diameter, while also showing that the critical flux was less pronounced in microfiltration of yeast. Thompson et al. [147] visualized combined biofouling and scaling in RO at pressures up to 25 bar to show that biofouling enhances scaling due to biofilm-enhanced concentration polarization. Microscopic observation of fouling has also been conducted in FO with latex particulates [66], showing that the rapid particle deposition that occurs beyond the critical flux occurs only between the embedded mesh filaments.

In situ visualization of alginate fouling is particularly challenging because the hydrogel formed in the presence of divalent cations is typically clear and, due to its high water content, has a refractive index close to that of water. Xie et al. [12] captured images of alginate fouling layers formed in FO, pressurized FO, and RO, before and after cleaning, using a polysaccharide-selective fluorescent dye and confocal laser scanning microscopy (CLSM) on samples cut from fouled membranes. The images are used to determine the thickness and quantity of foulant accumulation.

However, because the fouled membrane was observed ex situ and the area imaged was less than 1 mm^2, mechanisms of fouling and cleaning that are only observable during operation or that occur over macroscopic areas could not be identified. In this work, we highlight alginate fouling on FO and RO membranes with methylene blue and observe the membranes in situ to identify centimeter-scale fouling and cleaning mechanisms.

By visualizing alginate fouling in situ without magnification, this study identifies several previously undocumented mechanisms of flux decline and foulant removal: Osmotic backwashing leads not to gel dissolution, but the sloughing of macroscopic chunks. Gel swelling and wrinkling due to changes in ionic composition are powerful drivers of gel delamination and removal. Feed spacers, though effective at slowing flux decline, can reduce cleaning effectiveness by impeding removal of gel pieces. Finally, in FO with membranes oriented in PRO mode, increased membrane reflectance points to vapor formation due to low pressure within the membrane.

6.2 Experimental methods

Membranes are fouled with dyed alginate during RO and FO operation while transmembrane flux and photographs or videos are recorded. Methylene blue is used to dye the alginate and enable visualization of the deposition and removal of this otherwise clear gel. Cleaning steps are performed to elucidate foulant removal mechanisms.

6.2.1 Apparatus

Fouling and cleaning of RO and FO membranes are performed in a plate and frame membrane module. Pressure, temperature, and flow rate are controlled while permeate mass (or draw mass, in FO) is recorded, as detailed in our previous report [14]. A camera records fouling and cleaning through a window in the membrane module. Figure 6-1 shows the experimental apparatus.

Flux in lmh (L/m^2-hr) is calculated from the change in permeate volume over 15 minute intervals and the active membrane area. The mass of permeate or draw is

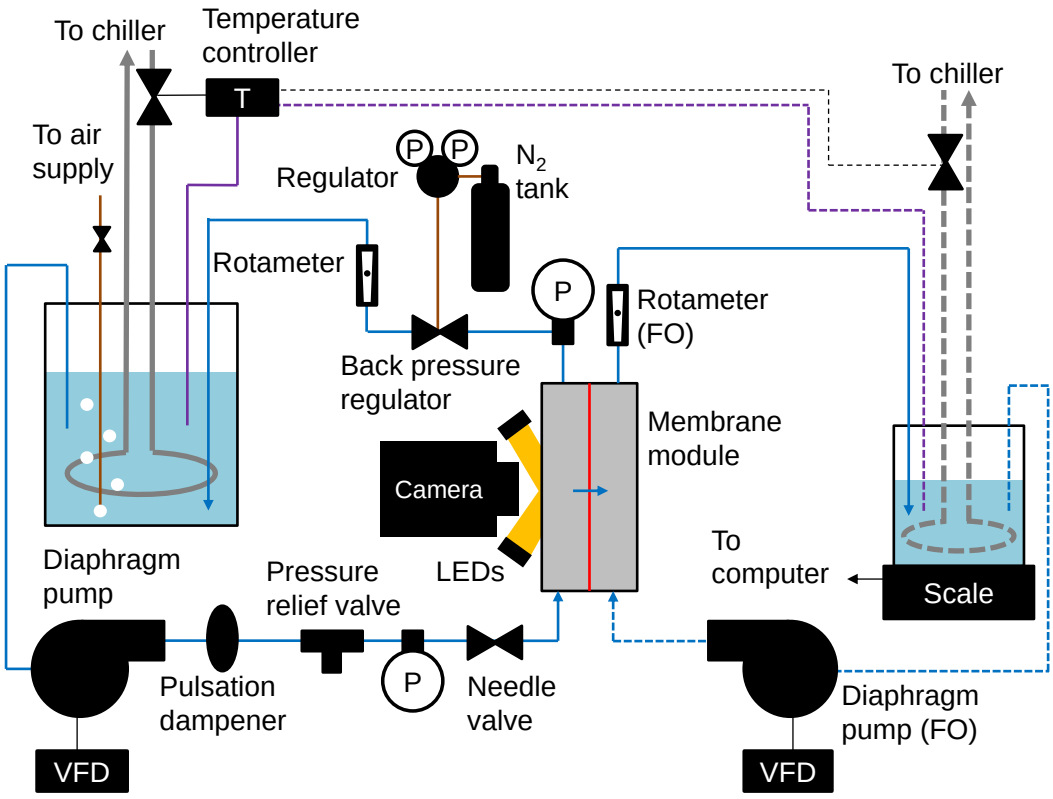

Figure 6-1: Schematic diagram of experimental fouling visualization and flux measurement apparatus that can be operated as RO or FO. Dashed lines represent flows only present in FO operation. VFD stands for variable frequency drive. Figure adapted from our previous report [14].

recorded every second with an Ohaus Scout Pro digital scale, which has a capacity of 6 kg and a repeatability of 0.1 g, and RealTerm software. In RO, permeate enters the tank through a rigid 1/8 in. (3.2 mm) tube submerged in the liquid, which displaces a negligible volume. In FO experiments, the volume displaced by the immersed cooling coil, draw inlet, and draw outlet is accounted for in the data analysis.

6.2.2 High pressure fouling visualization module

The module that holds the membrane is designed to withstand high pressure (up to 69 barg) and enable viewing of the membrane surface. For the module body, 316 stainless steel was chosen for its corrosion resistance. Polycarbonate was chosen as the material for the portal for its water tolerance, strength, and machinability. Figure

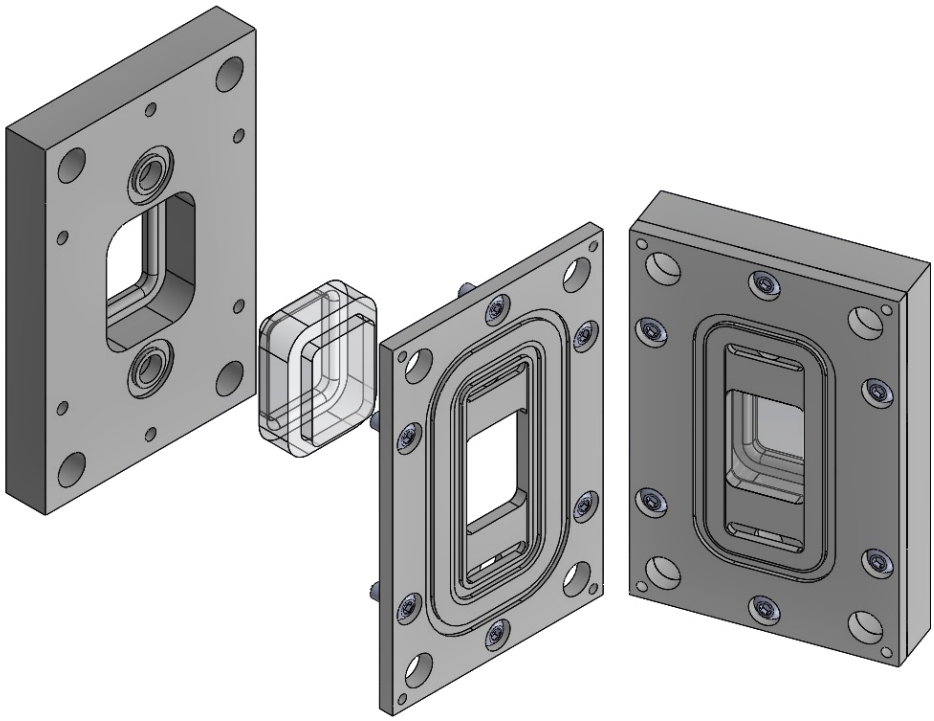

Figure 6-2: CAD rendering of the high pressure fouling visualization module with the feed side disassembled.

6-2 shows a rendering of the membrane module.

Inside the membrane module, the feed channel is cut 1 mm deep to approximate flow conditions in spiral-wound RO elements. The draw/permeate channel is also 1 mm deep. The channels are 8 cm long and 3 cm wide. Manifolds were designed to minimize entrance/exit effects. In RO operation, the draw/permeate channel contains five layers (for a total thickness of 1 mm) of permeate spacer mesh from a low pressure RO module. In FO operation, a 0.79 mm-thick, non-woven mesh feed spacer (Sterlitech 31 mil diamond) is used in the draw channel. The feed channel is left empty to encourage fouling except in three trials, in which either a coarse feed spacer identical to the draw spacer or a fine feed spacer (0.43 mm thick, Sterlitech 17 mil diamond) is placed in the feed channel.

The transparent polycarbonate portal shows the full width of the membrane but only the middle 4 cm in the length direction. The polycarbonate sits flush with the metal on the channel side so that the flow is not disturbed. The membrane is

illuminated from the feed side using two white LED arrays placed on either side of the camera, each illuminating the opposite half of the membrane. (Back-lighting the fouled membranes was also attempted, but the image quality was inferior.) Unlike RO membranes, the FO membrane is translucent, so white paper is placed on draw side window in FO operation to block light from behind the module.

O-ring grooves were designed to seal against high pressures while minimizing force on the membrane. Design details are included to enable replication. Three concentric O-rings (nitrile rubber in size 3/32) seal the module halves to each side of the membrane and to each other. Unlike some commercial membrane modules, the cross-sectional area of each O-ring is just 75% that of the the groove. The groove depth is 65% of the O-ring cord diameter. The gap outside the grooves is limited to 50 μm to prevent O-ring extrusion at high pressure. As a result, the module can be pressurized to at least 69 bar without leaking and the membrane damage by the O-rings is limited, as demonstrated by the closeness of measured RO salt rejection to membrane specifications [14].

6.2.3 Membranes

High-rejection thin-film composite polyamide membranes (Dow FILMTEC SW30HR) are used in RO tests. For FO tests, asymmetric cellulose triacetate (CTA) membranes with a woven support layer (Hydration Technology Innovations) are used in FO mode (active layer facing the feed) except where noted. The RO membrane has a permeability of approximately 3×10^{-12} m/s-Pa to 4.4×10^{-12} m/s-Pa according to the included specifications. In our previous report [14], the FO membrane was shown to have a water permeability of 1.9×10^{-12} m/s-Pa, support layer structural parameter of 5.7×10^{-4} m, and support layer dispersivity (which describes the enhancement of diffusion by convection through the porous support) of 1.65×10^{-4} m. Salt permeation coefficients of 2.38×10^{-8} m/s in RO and 5.32×10^{-8} m/s in FO and were calculated from membrane specifications to avoid measurement error resulting from the small size of our membrane module and the potential for salt leakage at the edges.

6.2.4 Feed and draw solutions

Sodium alginate is used as a model organic foulant at a concentration of 200 mg/L in all trials. Sodium alginate (Sigma-Aldrich A2033, denoted by "alginate" from here on) is a polysaccharide with a molar mass of 80,000-120,000 g/mol (as indicated on the supplier website). In all trials, 1 mM calcium chloride is added to the prepared feed solution to initiate fouling through complexation with the polyguluronates in alginate (see, e.g., [80, 81, 110]). Due to this complexation and the convection of solutes toward the membranes during operation, the alginate forms a hydrogel on the membrane.

Methylene blue (Alfa Aesar), a monovalent cationic dye, is used to dye the foulant. At sufficiently low salt concentrations, it colors the gel more intensely than the feed solution. Concentration of dye in the gel layer by cake-enhanced concentration polarization (see, e.g., [60]) also contributes to foulant layer visibility. Concentrated (1% wt.) methylene blue is added to the feed solution during membrane equilibration to reach a concentration of 7.6 μM.

Sodium chloride (Alfa Aesar 99% min.) is used in the feed and draw solutions. D-(+)-glucose (Alfa Aesar 99% min., denoted as "dextrose" in what follows) is also used to raise the feed osmotic pressure in one trial. Sodium chloride concentration is determined with a Hach conductivity meter and interpolation of tabulated NaCl conductivity data in Ref. [73]. Deionized water is used as the solvent throughout this experiment to prevent membrane damage by the chlorine in tap water. The draw solution is degassed before use to minimize outgassing, which displaces draw and affects the flux measurement. The feed solution is not degassed, but the membrane module is oriented vertically with upward flow to prevent air accumulation.

6.2.5 Fouling and cleaning procedure

Membranes are equilibrated and compacted as detailed in our previous report [14] before the concentrated alginate and calcium chloride solutions are sequentially added. To minimize differences in fouling rate and cleaning effectiveness due to variations in

flux, the initial flux before fouling is kept as close as possible to 23 L/m^2-hr (lmh) by choosing the feed pressure in RO and the draw solution's concentration in FO. In all trials, the feed cross-flow velocity is 8.3 cm/s during fouling and 25 cm/s during cleaning. After approximately eight hours of fouling, the cleaning step is performed for one hour (except where noted). Cleaning is either performed with forward flux, which only involves increasing the cross-flow velocity, or with reverse flux, which also involves reducing the feed pressure to atmospheric in RO or replacing the saline draw solution with deionized water in FO.

A Nikon P530 camera captures photographs every 30 seconds during fouling and videos during cleaning. The camera is manually focused on the membrane at the beginning of each experiment.

6.2.6 Data analysis

Flux decline (given in Sec. 6.4 as normalized flux) quantifies the response of a membrane and process to fouling. Normalized flux is calculated as a ratio of measured flux to the flux that would be predicted for an unfouled membrane under the same conditions. As in past studies (e.g., [9]), feed and draw concentrations are allowed to change gradually as water crosses the membrane. Here, these changes are accounted for in the prediction of foulant-free flux. Foulant-free predictions are made using the foulant-free models for RO and FO in [14], which are comparable to standard models except for the addition in [14] of dispersive salt transport in the FO support layer. The 95% confidence interval for flux decline for the present experimental apparatus operating at the same initial flux range is ± 0.036 in RO and ± 0.054 in FO [14].

Photographs and videos are used to identify mechanisms of fouling and foulant removal that have not been observed previously. Where noted, the contrast of individual colors was adjusted in MATLAB to improve clarity, but these adjustments were uniform within each image and throughout each video or set of images.

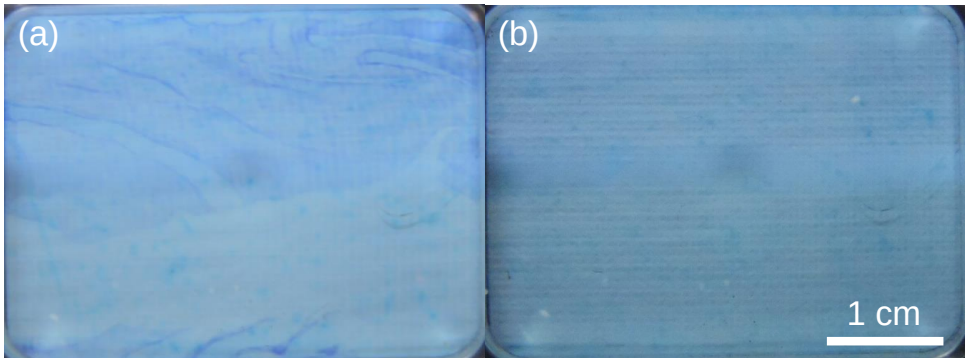

Figure 6-3: Video stills of alginate gel cakes with methylene blue on RO membranes during cleaning with 1 mM $CaCl_2$, 200 mg/L alginate, and (a) 0.17 M NaCl and (b) 0.52 M NaCl.

6.3 Validation of visualization method

6.3.1 Foulant visibility

To validate the visualization method, we first test the ability of methylene blue to dye alginate foulant in saline solutions. Ideally, as a layer of alginate gel forms, the cationic dye should preferentially bind to the negatively-charged alginate gel over the dilute alginate solution. However, other cations compete with the dye. Figure 6-3 shows video stills of fouled RO membranes during cleaning at two NaCl concentrations. As in all trials reported on here, the feed contains 1 mM $CaCl_2$ and 200 mg/L alginate. In Fig. 6-3a, the sodium concentration in the feed is 0.17 M, and it is possible to make out edges where the gel sheet has torn off as well as wrinkles in the sheet. In Fig. 6-3b, the NaCl concentration is three times as high, and although the image is uniformly blue because of the dye in the feed solution, no edges are visible. As we will show, digitally enhancing contrast improves visibility when there is contrast to begin with, but it appears that methylene blue is not able to dye alginate foulant at high salinity (e.g., seawater salinity). For high salinity studies, it may be worthwhile to test the visibility of alginate gel with other cationic dyes such as thionine acetate and pinacyanol chloride. For now, we will limit the scope of our investigation to fouling and cleaning at relatively low salt concentrations that might be found in brackish water desalination.

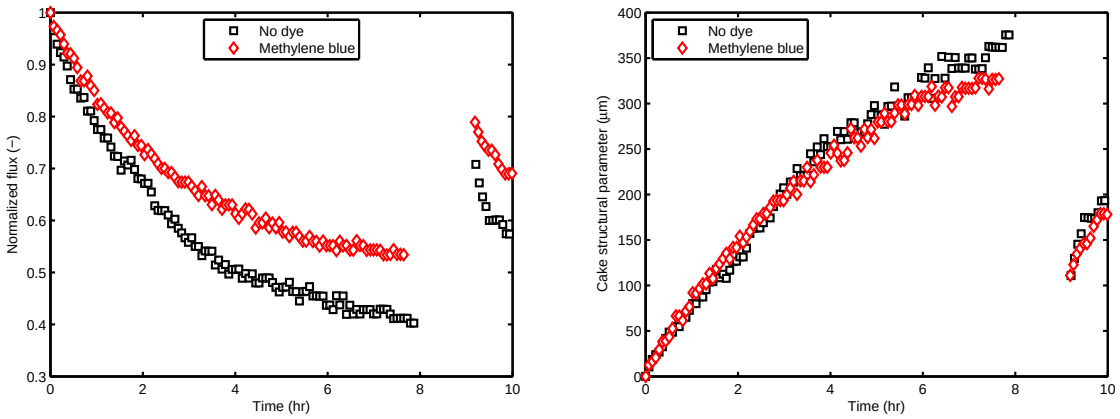

(a) Flux

(b) Accumulation

Figure 6-4: (a) Flux decline and (b) foulant accumulation in RO with 0.17 M NaCl, 1 mM $CaCl_2$, and 200 mg/L alginate, with and without methylene blue dye, at feed pressures of 39 and 27.3 barg, respectively. Initial flux was 21.7±0.2 lmh. No feed spacer was used. Gap in data indicates mechanical cleaning at atmospheric pressure. Uncertainty in normalized flux is ±0.036 and uncertainty in structural parameter is ±60 μm at the end of the fouling step.

6.3.2 Effect of dye on fouling rate and reversibility

To demonstrate the viability of methylene blue for fouling visualization, we next confirm that a low concentration of the dye does not affect fouling rate or susceptibility to cleaning. RO fouling and cleaning trials with the same initial flux and the same feed solution with and without methylene blue are compared in Fig. 6-4. Figure 6-4a shows the flux decline in both trials, from which it appears that methylene blue inhibits fouling. However, permeability varies between membrane samples, as evidenced by the different pressures needed to achieve the same initial flux (39 barg for the trial with dye and 27.3 barg for the trial without). Membrane permeability has been shown by the layered membrane model developed in our previous report [14] to affect flux decline for a given amount of foulant accumulation. In both cases, cleaning at atmospheric pressure with high cross-flow velocity (25 cm/s) for one hour partially restores the flux, but it is difficult to claim that the cleaning step was equally effective in the two cases.

To isolate the effect of the dye from the effect of varying membrane permeability,

the foulant accumulation rate and cleaning effectiveness are compared by analyzing the cake structural parameter using the layered model of transport in fouled RO membranes presented in our previous report [14]. Figure 6-4b shows that the cake structural parameter (the effective foulant thickness, Eq. 3.1), which is approximately equal to the actual thickness of accumulated gel because of the high porosity and low tortuosity typical of alginate gels [63], increases almost identically in the two trials to an effective thickness of about 350 μm. After cleaning, the effective cake structural parameter ("effective" because the remaining foulant layer is uneven and/or detached from the membrane) returns to approximately the same value, which shows that the dye does not substantially affect the susceptibility of the foulant to cleaning. We conclude that methylene blue does not affect foulant accumulation or removal and is therefore a suitable dye for visualization studies at low salinity.

6.4 Results

6.4.1 Swelling detachment mechanism

In some trials, swelling and wrinkling of the foulant were observed prior to complete detachment. This phenomenon, which occurred in both RO and FO, has the potential to be leveraged in membrane cleaning protocols.

To visualize mechanisms of foulant removal at high pressure, a feed solution of 0.17 M NaCl, 0.58 M dextrose, 1 mM $CaCl_2$, and 200 mg/L alginate was subjected to RO at a feed pressure of 69 barg. Dextrose was used to raise the osmotic pressure because, as shown in Fig. 6-3, methylene blue does not sufficiently dye the foulant gel at high sodium chloride concentrations. After fouling, the pressure was reduced to atmospheric, and the feed pump was stopped so that the foulant could be filmed undisturbed. This video is provided in the supplementary materials of Ref. [13]; several frames are highlighted in Fig. 6-5. Figure 6-5(a) shows that the foulant layer wrinkles in response to the reduction in pressure and Fig. 6-5(c-e) show the subsequent removal of the foulant layer when the cross-flow velocity is increased to 25 cm/s.

Initially, many small wrinkles form across the membrane, mostly aligned with the texture of the membrane that results from pressing against the permeate spacer. As the wrinkles grow, some join while others disappear, indicating that the gel sheet is detaching from the membrane. By the time the cross-flow velocity is increased, the sheet is almost completely detached. However, the edges of the foulant are still attached due to edge effects in the small membrane module, so the gel sheet flaps in the flow until it tears. Large sections of the gel sheet are then torn away.

Gel swelling and wrinkling as a precursor to detachment of the entire gel sheet was also seen in an FO trial with cross-flow during cleaning. In this trial, foulant was accumulated in FO orientation (feed facing the active layer, denoted as "FO mode" hereafter) using a 4.8 M NaCl draw solution and a feed of 0.17 M NaCl, 1 mM $CaCl_2$, and 200 mg/L alginate at 8.3 cm/s with no feed spacer. Cleaning with reverse permeation was performed by replacing the draw solution with tap water and increasing the feed velocity to 25 cm/s. Despite the high cross-flow velocity, which was absent during most of the wrinkle growth in the RO test described above, one wrinkle formed after two minutes of cleaning and grew for approximately six seconds before the entire gel sheet detached from the active area of the membrane. However, the sheet was still pinned at the edges of the channel, as it was in the RO trial above, and it peeled off 37 seconds later. Figure 6-5(e-g) shows the wrinkling and detachment of the gel sheet in FO.

Wrinkle formation can be explained by isotropic swelling[1] of the gel when the direction of permeation is reversed. Swelling leads to wrinkling when the elastic energy of the swollen gel, which is under compression in the plane of the membrane to which it is attached, is enough to overcome adhesion to the membrane. The proposed mechanism is illustrated in Fig. 6-6. A similar wrinkling instability forms when a thin film under compressive stress is adhered to a thick substrate [148], in

[1]The height of the wrinkles in Fig. 6-5 and the degree of swelling can be estimated by looking at the double shadows of the wrinkles in the center of the channel that are illuminated by both LEDs. From the distance between the shadows and the placement of the light sources, and estimating the refractive index of the water-based feed solution as 1.33 (roughly that of water), the height of the central wrinkles can be estimated as 0.9 mm, or 90% of the channel height. Approximating the number of horizontal wrinkles across the 3 cm channel width as three, the magnitude of linear swelling can then be estimated to be around 18%.

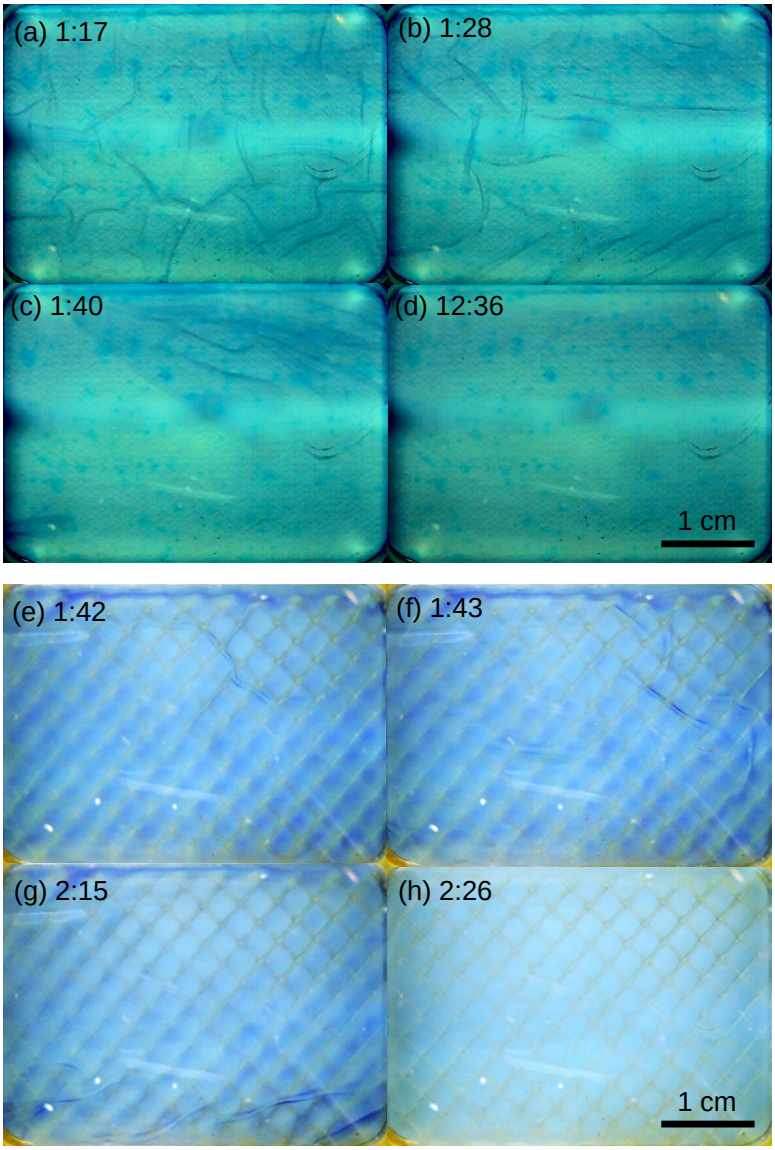

Figure 6-5: Video stills of wrinkle formation during cleaning of (a-d) RO and (e-h) FO membranes without feed spacers. Feed contained 0.17 M NaCl, 1 mM $CaCl_2$, and 200 mg/L alginate, plus 0.58 M dextrose in the RO trial. RO fouling was performed at a feed pressure of 69 barg. In the RO trial, feed pressure was reduced to atmospheric during the period -0:55 to 0:00 and held at 0 barg thereafter. Feed velocity was reduced from 8.3 cm/s (left to right) to 0 cm/s from 0:18 to 0:22, held at 0 cm/s until 1:27, raised to 25 cm/s between 1:27 to 1:32, and maintained a 25 cm/s thereafter. (a) Wrinkles begin to form under stagnant conditions. (b) As the velocity is increased, the wrinkled sheet deforms with the flow. (c) Partially-cleaned membrane. (d) The cleaned membrane. In the FO trial (e-h), fouling was performed with a draw solution of 4.8 M NaCl and a coarse draw spacer. Cleaning was performed with 25 cm/s feed cross-flow and tap water in the draw channel. (e) Wrinkles form in the upper-right quadrant. (f-g) The sheet detaches, but is pinned at the edges of the channel. (h) The cleaned membrane. Image contrast was enhanced uniformly within (a-d) and (e-h). Time stamps are in minutes and seconds beginning at the start of cleaning.

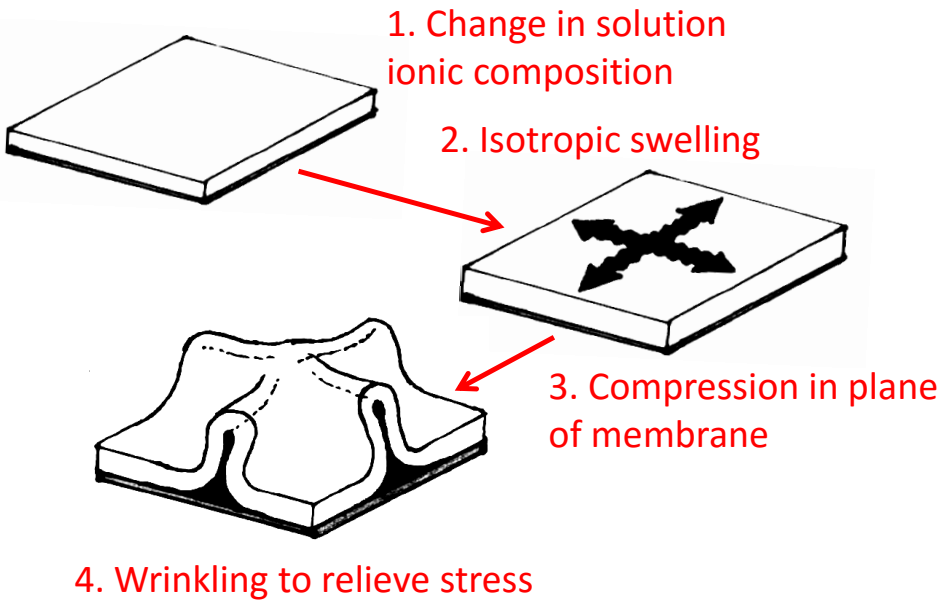

Figure 6-6: Proposed mechanism of foulant gel wrinkling and detachment.

which case thicker films with a lower adhesion energy are more prone to wrinkling.

The swelling itself can be explained by the change in ion concentration in the gel layer when the pressure is released during cleaning in RO or the draw solution is changed in FO. Although it has been proposed that pressure itself compacts alginate gels, this is only physically explained if alginate is compressible, which measurements show that it is not [12]. Additionally, the formation of wrinkles during cleaning of the FO membrane in Fig. 6-5 cannot be explained by a decrease in pressure because pressure was not changed during cleaning. However, the reduced pressure during RO cleaning and reduced draw solution concentration during FO cleaning both cause water to flow back through the membrane into the feed by osmosis[2]. Whereas during fouling, concentrative cake-enhanced concentration polarization caused the ion concentration in the gel to exceed that of the feed, reverse water permeation by osmosis during the cleaning step causes dilutive concentration polarization in the gel layer and ion concentration in the gel becomes lower than that of the feed. In addition, the lower diffusion coefficient of calcium chloride causes the sodium:calcium mole ratio to

[2]This is sometimes termed "osmotic backwashing," particularly when the feed concentration is increased.

increase when the concentration polarization in the gel is switched from concentrative to dilutive.[3] Moe et al. [99] show that alginate gels in sodium chloride solutions swell when the concentration in the surrounding fluid is decreased, which is consistent with the swelling seen in Fig. 6-5. However, the same study shows that alginate gels in calcium chloride solutions exhibit hysteresis: although they shrink when the concentration is increased, they do not re-swell when the concentration is decreased because bound calcium ions are not released. However, gels in mixed Na–Ca–Cl solutions may exhibit less hysteresis than those in pure $CaCl_2$ solutions because of the ion-exchange reaction [110] between bound calcium and sodium in alginate gels. Further research is needed in this area to fully characterize and manipulate the foulant gel swelling phenomenon. However, our preliminary experiments in alginate gel swelling indeed show that gel volume increases with decreasing ionic strength and also increases with increasing sodium:calcium mole ratio.

Swelling helps remove alginate fouling by instigating detachment of the gel from the membrane and lowering the energy barrier to foulant removal. Swelling by introduction of calcium-free sodium chloride solutions has previously been reported to cause alginate fouling removal [72]. In the absence of visual observations, the removal mechanism after introduction of a more concentrated NaCl feed solution was theorized to be swelling of the gel, dissolution of the gel by breaking the bonds between calcium and alginate, and finally "layer-by-layer removal" of the foulant by "mass transfer" [72]. However, at least in the present study, it is clear that alginate gel removal occurs not by diffusion but by the release of macroscopic sheets. The present observations suggest that cleaning processes can be designed to instigate foulant layer detachment and rapid, macro-scale removal by including a step designed to cause swelling of the foulant.

[3]In FO, the ionic strength still decreases, but the sign of the change in sodium:calcium ratio depends to some extent on the draw solute and membrane solute permeation coefficient.

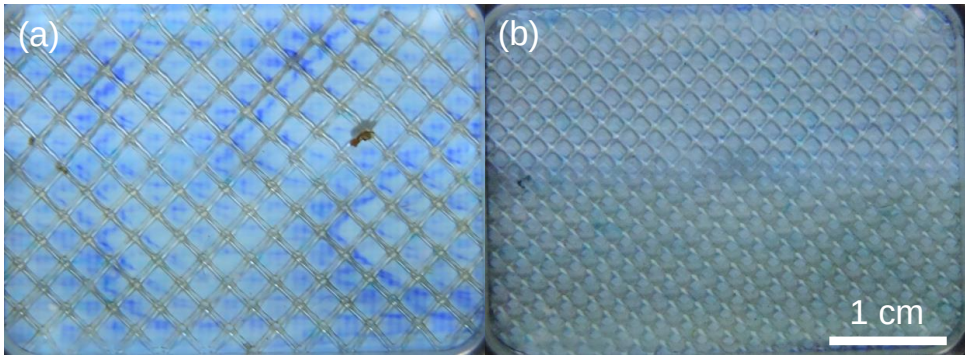

Figure 6-7: Photographs of the fouled RO membrane with (a) coarse and (b) fine spacers.

6.4.2 Effects of feed spacers

To investigate the effect of feed spacers on foulant deposition and removal, RO and FO trials were conducted with and without feed spacers. The feed spacers used are described in Sec. 6.2.2. Although feed spacers do reduce the rate of flux decline, we find that they also reduce the cleaning effectiveness by impeding the flow of detached foulant pieces.

Figure 6-7 shows the fouled RO membrane with the coarse and fine feed spacers. The standard feed solution of 0.17 M NaCl, 1 mM $CaCl_2$, and 200 mg/L alginate was used. The pattern of fouling is less uniform with the coarse spacer than without a spacer (e.g., Fig. 6-5a). The color is generally darker between the filaments of the spacer, but the intensity also varies across the membrane, suggesting that the spacer (which is 0.21 mm narrower than the channel) did not lay flat. This spatial variability highlights the complexity of spacer design for fouling control: minute changes in spacer geometry can affect fouling. Unfortunately, the foulant visibility with the fine spacer is poor and the presence of either feed spacer makes it difficult to detect the edges of the foulant and see what occurs during cleaning. Photos of the cleaning process are therefore not included here.

Changes in RO flux due to fouling and cleaning with and without spacers are shown in Fig. 6-8. Flux decline is most severe in the case with no spacer, and similar between cases with different spacers. After cleaning at atmospheric pressure, the flux

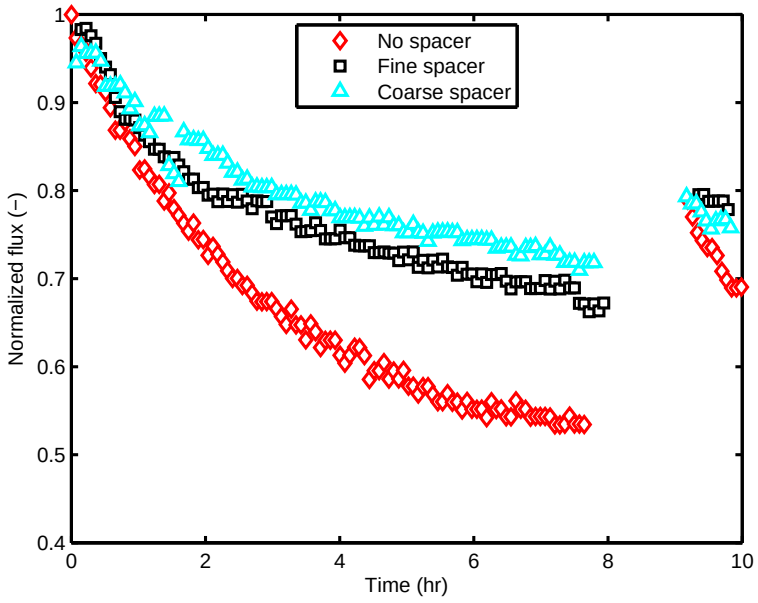

Figure 6-8: Flux decline in RO with fine, coarse, and no feed spacer at feed pressures of 35.2, 37.5, and 39 barg, respectively. Feed contained 0.17 M NaCl, 1 mM $CaCl_2$, and 200 mg/L alginate and initial flux was 21.5±0.6 lmh. Gap in data indicates mechanical cleaning at atmospheric pressure. Uncertainty in normalized flux is ±0.036.

recovers to roughly the same level for all three cases, although the fractional flux recovery is better without the spacer.

Figure 6-9 shows the spatial pattern of fouling in an FO trial with an identical feed solution to the RO trials shown in Figs. 6-7 and 6-8. Foulant is more visible than in the RO cases, and a change can be clearly seen during the first 2.5 minutes of cleaning. Before cleaning, the pattern of the fine draw spacer behind the membrane is visible, suggesting that draw spacer design can influence fouling patterns through their effect on the spatial variation in draw-side mass transfer coefficient and transmembrane flux.

During cleaning, the gel detaches from the membrane, but its movement through the channel is hindered by the presence of the spacer. A video of this cleaning process, from which the stills in Fig. 6-9 are taken, is provided in the supplementary materials of Ref. [13]. Because the macroscopic pieces of detached gel are prevented from flowing downstream by the diamond spacer, they instead move diagonally, tangent to one set of spacer filaments. Once enough gel travels in this way and accumulates at the edge of the channel, some of it changes direction and moves diagonally tangent to the other set of spacer filaments. As shown in Fig. 6-10, the result is a very low cleaning effectiveness similar to that seen with the same spacer in RO under similar conditions in Fig. 6-8. In contrast, in the case of FO with no spacer, the cleaning step was only run for 15 minutes because it was clear that the entire sheet of foulant had been removed[4].

Figures 6-8 and 6-10 show that, in both FO and RO fouling, spacers reduced flux decline but also reduced the fraction of the flux decline recovered by cleaning. Clearly, spacers can improve the fouling resistance of RO and FO systems, but spacers used in systems with gel-forming foulants should ideally be designed to minimally impede the flow of foulant pieces once those pieces are detached from the membrane.

[4]In fact, it came off in one piece and clogged the downstream back pressure regulator, causing the feed pressure to climb to 2 barg temporarily. The pressure spike may have stretched the membrane, which would explain why the normalized flux slightly exceeded 1 after cleaning.

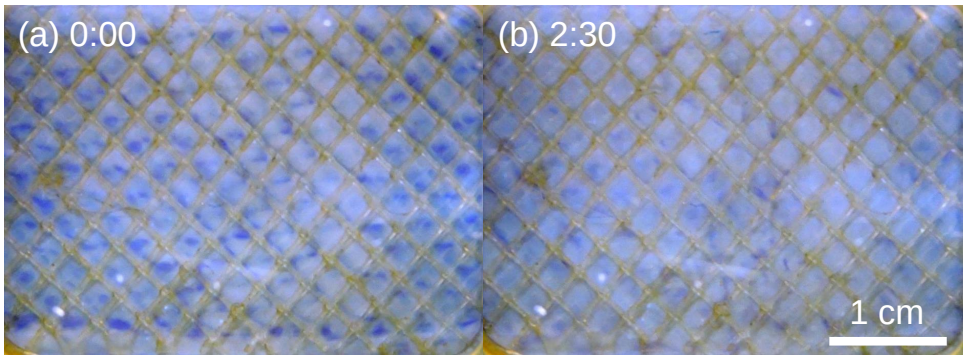

Figure 6-9: Video stills of fouled FO membrane with a coarse feed spacer (a) before and (b) during cleaning with 25 cm/s cross-flow velocity and tap water draw.

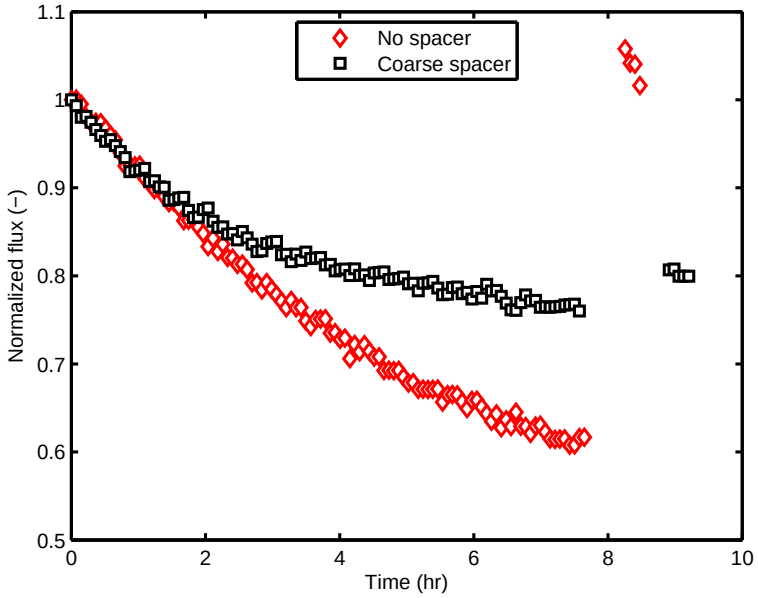

Figure 6-10: Flux decline in FO (FO mode) with and without a coarse feed spacer at draw concentrations of 4.9 and 4.8 M NaCl, respectively. Feed contained 0.17 M NaCl, 1 mM $CaCl_2$, and 200 mg/L alginate and initial flux was 25.1 lmh in both cases. Draw velocity was 4.3 cm/s in the trial with a feed spacer and 16.7 cm/s in the trial without. In the case with no spacer, cleaning was stopped after 15 minutes because it was clear that the entire foulant layer had been removed.

6.4.3 Effect of permeation direction on cleaning

Flux recovery and foulant removal are affected by the direction of permeation during cleaning. In this study, the direction of permeation during RO cleaning is determined by the feed pressure: for forward-flux cleaning, the pressure is maintained so that permeation continues as usual; for reverse-flux cleaning, the feed pressure is reduced to atmospheric, causing permeate to flow by osmosis back into the saline feed. Cleaning with reverse permeation was found to be more effective at removing foulant and recovering flux.

Figures 6-11 and 6-12 show video stills from cleaning fouled RO membranes with forward and reverse permeation, respectively. In both, the membrane exhibits a fouling pattern aligned with the texture the membrane takes on from being pressed against the permeate spacer. The finer (sub-mm) patterning corresponds to the texture of the spacer; the coarser pattern that is more visible in Fig. 6-12a corresponds to a moiré pattern from the imperfectly-aligned stack of permeate spacers. These patterns of foulant (and dye) accumulation may occur due to variations in flux, shear stress and/or mass transfer coefficient on the rough surface. As the cleaning step progresses, different processes govern foulant removal depending on the direction of permeation. When the foulant cake detaches from the membrane during forward permeation, cake-enhanced concentration polarization is reduced because solute flow is no longer confined to the direction perpendicular to the membrane, resulting in lower concentration of methylene blue. The lighter color in Fig. 6-11b suggests that the gel sheet has separated from the membrane in the case with forward permeation. The gel appears to bend in the direction of flow, forming wrinkles along the sides of the channel and tearing in multiple places. Eventually, a large section of the gel sheet tears off and flows away. The majority of the sheet remains in place for the remainder of the cleaning step. The detachment of the gel sheet cannot be explained by swelling or shrinking of the gel, because the ionic environment was not changed; the actual cause remains unclear.

Figure 6-12 shows the progression of the cleaning step when the direction of

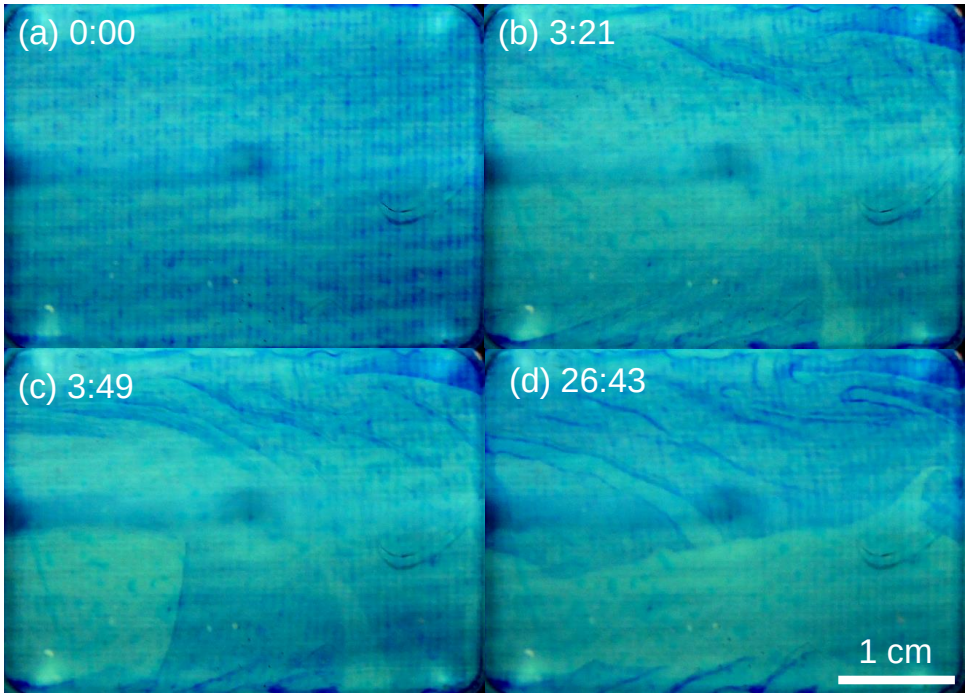

Figure 6-11: Video stills of cleaning an RO membrane at high feed pressure (35 barg) with a feed of 0.17 M NaCl, 1 mM $CaCl_2$, and 200 mg/L alginate. Contrast was enhanced uniformly. (a) is the fouled membrane before cleaning, which shows the pattern of the spacer. In (b), the foulant cake wrinkles in the upper right and tears in the lower right corner when the membrane is subjected to cross flow; (c) shows further wrinkling and tearing. (d) shows the state of the cake at 26 minutes, which does not change significantly during the rest of the hour of cleaning.

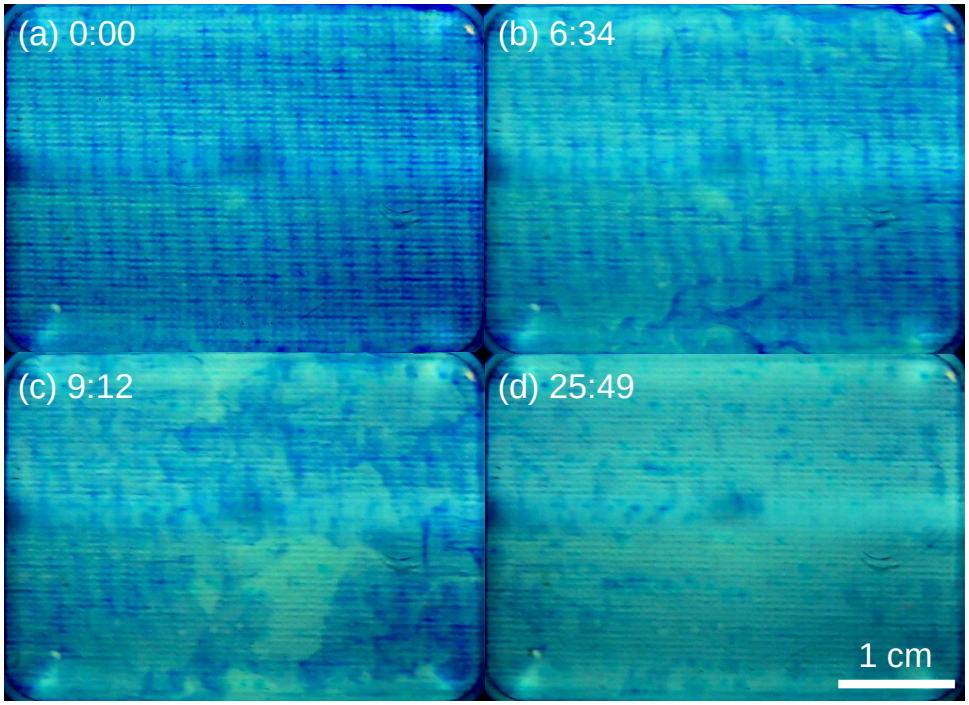

Figure 6-12: Video stills of cleaning an RO membrane at atmospheric pressure. The feed, which was pressurized to 39 barg during fouling, contained 0.17 M NaCl, 1 mM $CaCl_2$, and 200 mg/L alginate. Image contrast was enhanced uniformly. (a) shows the fouled membrane before cleaning. (b) shows some wrinkling of the cake near the edges; (c) shows further wrinkling and patches where the gel has been removed. (d) shows the state of the membrane at 26 minutes, which does not change significantly during the rest of the hour of cleaning.

permeation is reversed by reducing the feed pressure to atmospheric. As in Fig. 6-11, the initial reduction in color intensity can be attributed to reduced concentration polarization of the dye in the gel, but in this case the flow of dye is back toward the feed because the direction of permeation is reversed. Gradually, small wrinkles form, and then pieces of gel break off and are removed with the flow.

Figures 6-13 shows that the cleaning step with reverse permeation was more successful. Cleaning involving reverse permeation ("backwashing") is common, and the improvement is typically attributed to the change in direction of drag force on the porous cake [149]. However, the relationship between permeation direction and foulant removal effectiveness is not entirely straightforward. One study showed that osmotic backwashing in FO was effective at removing alginate gel or silica nanoparti-

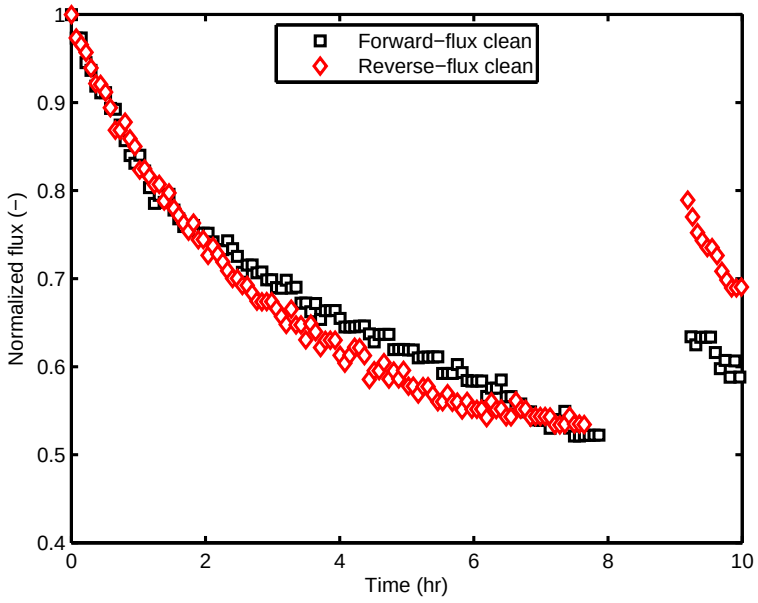

Figure 6-13: Normalized flux in RO with 0.17 M NaCl, 1 mM $CaCl_2$, and 200 mg/L alginate with forward-flux cleaning at RO pressure and reverse-flux cleaning at atmospheric pressure, each beginning at 8 hours. RO feed pressures were 35 and 39 barg, respectively. Initial flux was 21.6±0.3 lmh. Gap in data indicates cleaning. Uncertainty in normalized flux is ±0.036.

cles, but not humic acids [149]. In the salt cleaning experiments of Lee and Elimelech [72], better RO flux recovery when cleaning with NaCl solutions was achieved with a high forward permeation rate of 20 μm/s than when reverse permeation was allowed. The salt solution was then forced into the foulant layer and concentrated there by cake-enhanced concentration polarization. In both the Lee and Elimelech study and the present comparison, regardless of the pressure or direction of permeation, the cleaning step was more effective when the change in the ionic environment of the alginate gel was larger.

6.4.4 Effect of FO membrane orientation

The cleaning mechanisms observed thus far (wrinkling, peeling, hindrance by spacers) have been identical between FO and RO trials with the feed facing the active layer. The typically higher susceptibility to cleaning of FO has previously been attributed to a looser foulant layer formed in the absence of "compaction" by hydraulic pressure [10], but the present results do not indicate that cleaning proceeds differently in FO and RO. However, we have identified one previously undocumented mechanism of fouling that is unique to FO membranes in PRO orientation (feed facing the support layer, denoted as "PRO mode" hereafter). The PRO mode is important to consider because it achieves higher flux in applications with low-concentration feeds, such as personal hydration packs and fertigation, and yet is often avoided because of its typically worse fouling propensity [54]. In this section, we present evidence of vapor formation inside the FO membrane in PRO mode.

Alginate fouling in forward osmosis (both FO mode and PRO mode) with a feed NaCl concentration of 0.17 M is shown over time through unaltered photographs in Fig. 6-14. In the FO mode test, the draw solution was 4.8 M and the initial flux was 25.1 lmh. In the PRO mode test, the draw solution was 4.1 M and the initial flux was 23.6 lmh. In both cases, there is no feed spacer and a coarse draw spacer is used with a draw solution velocity of 16.7 cm/s. In FO mode (Fig. 6-14a-c), fouling results in almost no visible change despite the significant flux decline shown in Fig. 6-15. In PRO mode (Fig. 6-14d-f), the image begins almost uniformly blue except for a few

patches of lighter blue with with a faint texture of the woven support layer, whose fibers are around 100 μm apart [51]. These pale patches appear to indicate regions where the support layer is not fully wetted, causing reflections from inner air–water or air–polymer interfaces. After five hours of fouling (Fig. 6-14b), the total area of the pale regions has increased. By eight hours (Fig. 6-14c), the pale regions cover a significant fraction of the membrane, and the texture of the woven support layer is clearly visible in those regions.

In Fig. 6-15, flux decline rates are compared between FO membranes in FO and PRO modes as well as RO membranes fouled under similar conditions. In RO and FO-mode FO, flux declines in a similar shape toward what appears to be a similar asymptote, but the FO flux decline is slower. As explained in Ref. [27], FO flux decline is mitigated by the balancing effect of internal concentration polarization (ICP). Because of this effect, termed "ICP self-compensation" [27], FO flux is expected to decline more slowly, especially in FO mode because the support layer is facing the more concentrated draw. FO flux decline is expected to be greater in PRO mode than in FO mode because of the more pronounced ICP self-compensation effect when the support layer is facing the draw. However, PRO-mode flux decline is not expected to be greater than in RO, as it is shown to be in Fig. 6-15, unless there are additional mechanisms of flux decline unique to PRO-mode FO. Enhanced flux decline in PRO mode over FO mode has previously been attributed to the smaller ICP self-compensation effect and pore clogging by foulants [150], but this visualization study shows that internal fouling due to vapor formation may be an additional driver of flux decline in PRO mode.

Gas or vapor may accumulate in FO membranes due to pressure drop through the foulant or pressure drop across the solution–active layer interfaces. The buildup of a foulant cake with a fine pore structure causes a pressure drop through the cake when water permeates through it, resulting in a sub-atmospheric pressure at the FO membrane [14]. In cases where the membrane is in FO mode and the pores of the foulant cake are very fine, hydrophilic, and free of defects, the pressure can get very low or even negative in the absolute sense–that is, the water inside the cake could

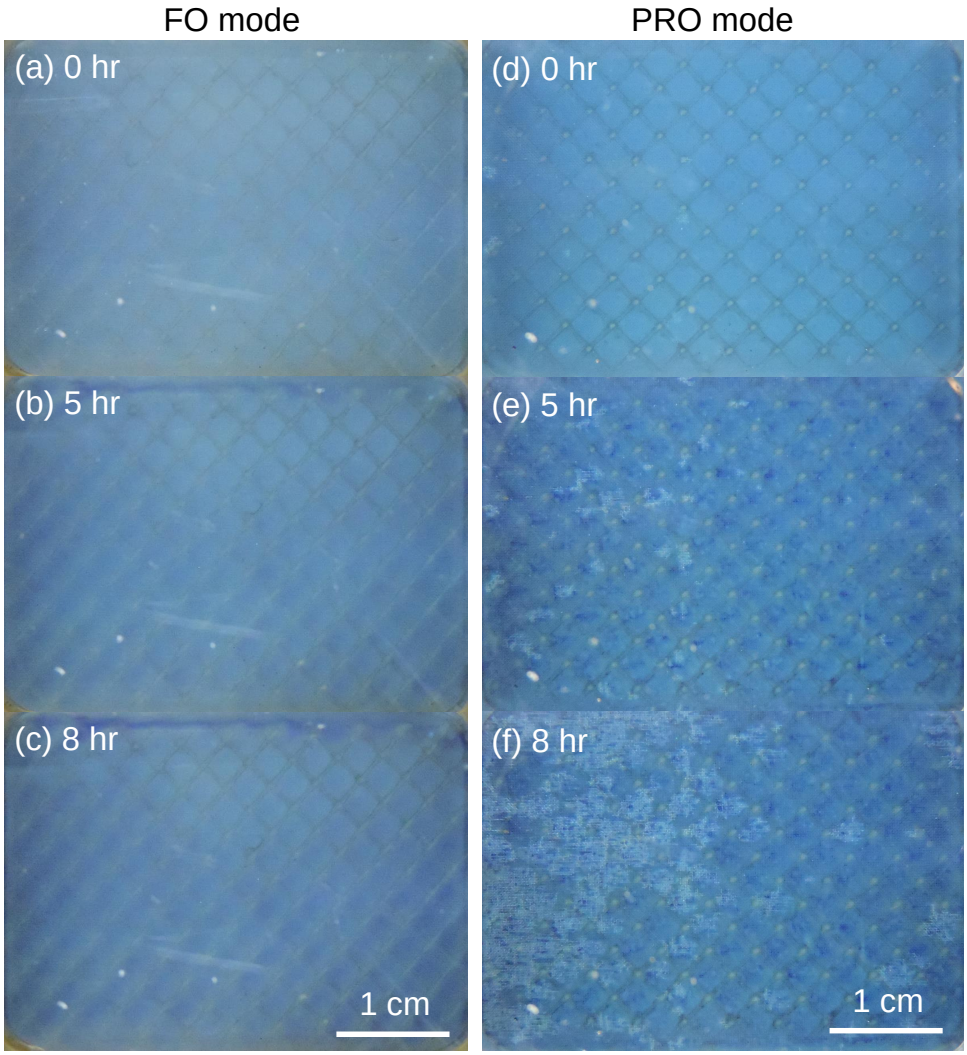

Figure 6-14: Photographs of FO membrane during fouling in FO mode and PRO mode with a feed of 0.17 M NaCl, 1 mM $CaCl_2$, and 200 mg/L alginate with no feed spacer (the draw spacer is visible through the membrane). Fouling in FO mode (a-c) is barely visible, indicating relatively uniform accumulation. Before fouling in PRO mode, the image (d) is uniformly blue, except for a few lighter patches. In (e) and (f), fouling has resulted in expansion of the lighter regions.

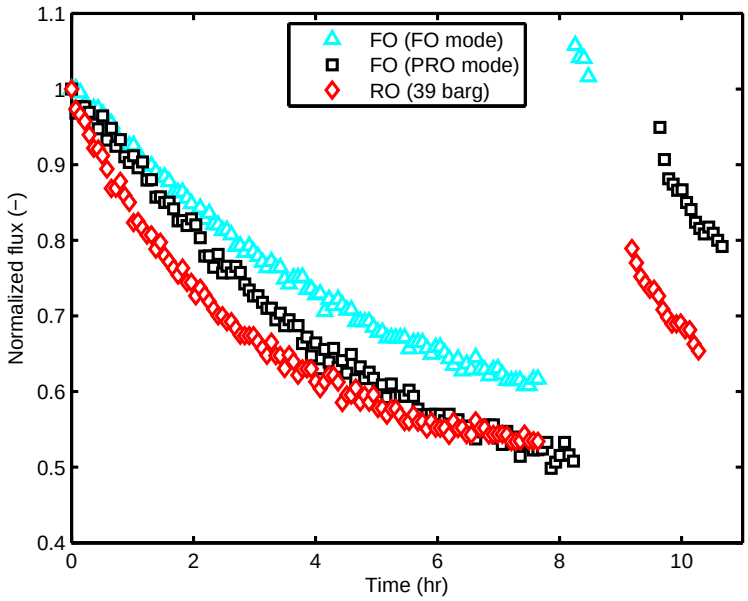

Figure 6-15: Flux decline and recovery in FO and RO: FO in FO mode with 4.8 M draw at 25.1 lmh initial flux, FO in PRO mode with 4.1 M NaCl draw and 23.6 lmh initial flux, and RO at 39 barg feed pressure with 21.9 lmh initial flux. Identical feed solutions of 0.17 M NaCl, 1 mM $CaCl_2$, and 200 mg/L alginate are used. Cleaning was performed with reverse flux in all trials, but for only 15 minutes in the FO-mode FO trial because it had already achieved complete foulant removal. Uncertainty in normalized flux is ± 0.054 for FO and ± 0.036 for RO.

be in tension–without nucleating bubbles of air or water vapor because of the small size (in nanometers) of the available nucleation sites in the gel or active layer [14]. In real foulant cakes, defects may be present that are large enough to allow nucleation of dissolved air or, at lower pressures, water vapor inside the cake or at the cake-membrane interface. In PRO mode, nucleation could also occur in the micrometer-scale pores in the feed-facing support layer. In a study by Wang et al. [66], optical microscope images of the support layer of HTI's CTA FO membranes show pores of roughly 10-50 μm in diameter, and SEM images appear to show some pores that are closed. The closed pores will not fill with foulant, and could allow the formation of stable air bubbles at only slightly subatmospheric pressures (e.g., roughly -0.14 barg in 20 μm-diameter pores[5]). Therefore, the pressure drop across the foulant may be sufficient to cause vapor formation in the support layer in PRO mode.

Alternatively, the vapor phase may appear due to a pressure drop across the solution–active layer interface on both sides of the active layer, which is predicted by an osmotic pore flow model for semipermeable membranes [151]. To maintain thermodynamic equilibrium across the entrance to pores in the active layer (which have been shown to exist at diameters of 0.4-0.58 nm in RO membrane active layers by multiple positron annihilation spectroscopy studies [106]), the osmotic pore flow model of Anderson and Malone [151] predicts that the pressure inside the pores drops to approximately the hydraulic pressure minus the osmotic pressure outside the membrane. In PRO orientation, the active layer can contact solutions with osmotic pressures in the hundreds of bars, possibly resulting in highly negative pressures inside the active layer that may be low enough to generate stable vapor bubbles inside nanometer-scale pores. Based on the osmotic pore flow model and the draw solution, pressure, and temperature used in the PRO test reported here, a stable vapor phase could form in internal spaces with diameters as low as 8 nm diameter near the draw side of the active layer. This mechanism of internal vapor formation has the potential to occur regardless of foulant accumulation outside the membrane. However, it is

[5]This pressure estimate assumes feed water is saturated with dissolved air, air bubbles are spherical with diameters (confined by the pore) up to 20 μm, and water-air surface tension of 70 mN/m.

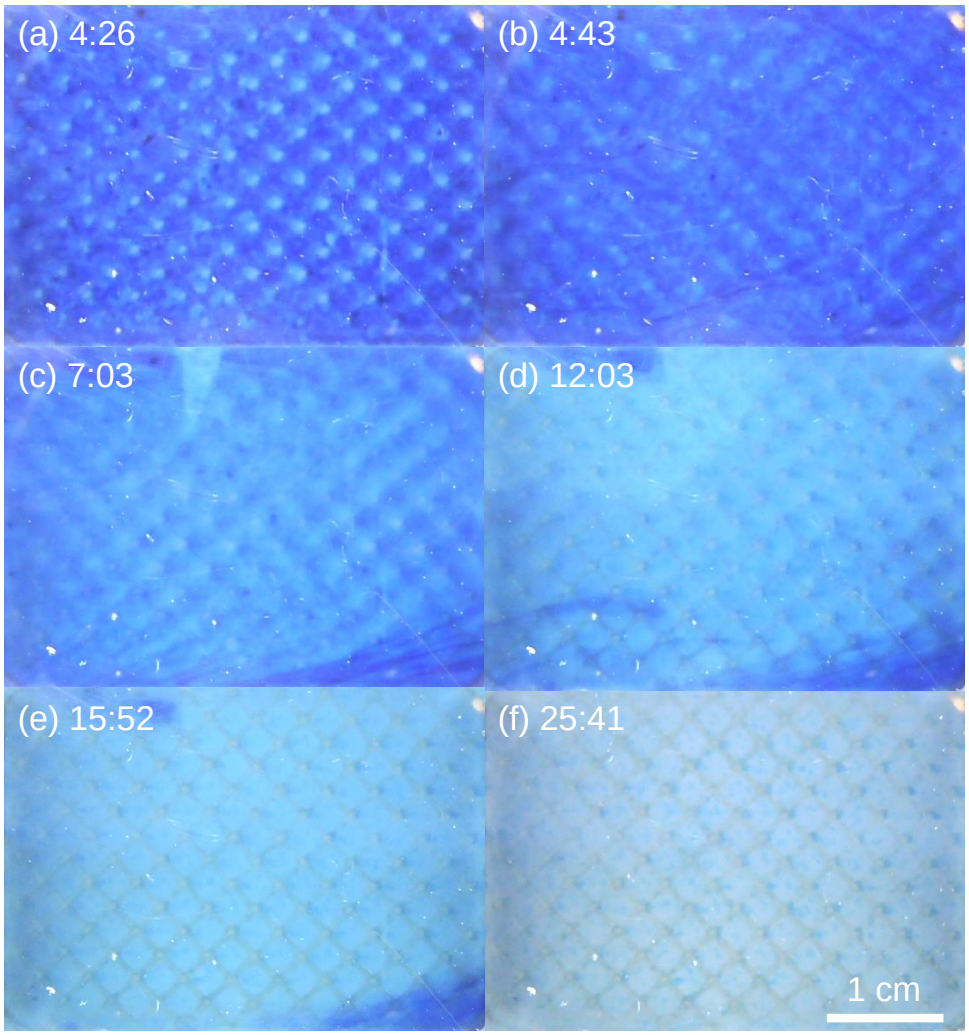

Figure 6-16: Video stills of cleaning the PRO-mode FO membrane shown in Fig. 6-14d-f. (a) After deionized water is introduced into the draw channel to reverse the direction of flow, the textured patches seen in Fig. 6-14 disappear. (b) The gel sheet detaches in the center and flaps in the flow. (c) The sheet rips. (d-e) Pieces of gel tear away. (f) The clean membrane.

unclear if a gas phase actually appears. The color change may also be some other response of the polymeric active layer to the highly-concentrated draw solution.

Despite the optical changes to the membrane observed during fouling in PRO mode, the subsequent cleaning process appears to proceed similarly to the other trials in this study. A video of the fouled PRO-mode FO membrane during cleaning is provided in the supplementary materials of Ref. [13], and highlights are shown in Fig. 6-16. This cleaning step is performed with reverse flux. Initially, the textured patches disappear, which should occur when the permeation direction is reversed because the pressure in the support layer rises to atmospheric, causing vapor to condense and trapped air to shrink according to the ideal gas law. After several minutes, the entire gel sheet becomes detached from the membrane except at the edges, and the sheet flaps in the cross-flow and is gradually torn apart. As shown in Fig. 6-15, flux recovery in PRO mode was substantial but not complete. The visual record of the cleaning process (Fig. 6-16 and video) appears to show complete foulant removal, at least in the visible section of membrane, but the incomplete flux recovery could indicate that the internal vapor formation resulted in irreversible damage to the membrane.

6.5 Chapter conclusions

In this study, mechanisms of alginate gel fouling and cleaning in RO and FO were studied using methylene blue dye in a high-pressure membrane fouling visualization module. Methylene blue was effective in that it did not affect fouling rate or cleaning effectiveness, but it only preferentially stained the foulant in low-salinity feeds ($\leq$1% wt. NaCl).

Centimeter-scale visualization of alginate fouling and cleaning revealed several mechanisms of foulant removal that were common to RO and FO:

- When cleaning alginate fouling with high cross-flow velocity, foulant removal occurs by break-away of macroscopic chunks.

- Swelling and wrinkling of the alginate gel sheet due to locally changing ionic

composition are powerful mechanisms of gel detachment and may contribute to the effectiveness of osmotic backwashing.

- Although feed spacers reduce the rate of fouling, they also hinder cleaning by preventing pieces of detached gel from flowing downstream.

Additionally, one internal fouling mechanism was identified that is unique to FO membranes: vapor phase formation within the membrane.

Understanding these mechanisms is a step toward predictive modeling of the effectiveness of cleaning processes and better design of membranes, spacers, and cleaning cycles for long-term control of membrane fouling in desalination systems.

Chapter 7

Conclusion

In this thesis, experimental and modeling approaches were used to better understand the factors governing fouling in membrane desalination processes. After comparing the energy efficiency of different desalination processes in Chapter 2, three membrane-based processes (RO, FO, and MD) were compared in terms of their fouling behavior (Chapters 3 and 5). To understand the effect of pressure on fouling, hydraulic pressure was isolated through a new experimental methodology (Chapter 4). Finally, in situ visualization of membrane cleaning processes was used to elucidate mechanisms of foulant removal (Chapter 6). In addition to the findings summarized at the end of each chapter, several major conclusions of this thesis follow:

1. The exergetic efficiency of FO desalination is the product of the FO exchanger and draw regenerator efficiencies, each of which is substantially less than one. This finding motivates the search for a better understanding of the factors contributing to FO's fouling resistance with the goal of replicating those factors in the more efficient RO process.

2. The decline in flux that results from the deposition of a given foulant layer depends on membrane properties and operating conditions. Therefore, flux decline alone should not be used to quantify the extent of fouling. Fair comparisons of fouling propensity between different membranes and processes should therefore consider both flux decline and foulant accumulation. Chapter 3 provides

a method of calculating foulant accumulation from flux decline, which is easily measured.

3. Contrary to what is often reported, we found no effect of hydraulic pressure on alginate fouling. When pressure was isolated from other variables that can affect fouling by the method described in Chapter 4, pressure was found not to affect flux decline rate, cleaning effectiveness, or foulant removal mechanisms.

4. Although both the FO and MD processes exhibited some resistance to specific foulants, they were not immune to fouling. In tests under identical hydrodynamic conditions, FO exhibited similar alginate fouling behavior to RO, and gypsum fouling led to faster flux decline in MD than in RO. These findings demonstrate that low-pressure operation should not be considered a panacea for fouling.

5. Removal of alginate fouling occurred by sloughing of large pieces rather than by dissolution and diffusion. Causing whole foulant layers to swell and buckle through changes in solution composition is a promising approach for low-chemical cleaning of desalination membranes.

7.1 Future directions

Understanding fouling is necessary to guide the development of new membranes, desalination processes, and cleaning protocols. However, much work remains to be done. Future research should aim to develop predictive models of foulant accumulation, membrane performance decline, and system energy consumption based on membrane properties, feed composition, and operating conditions. Future studies should also aim to identify the cause of FO's fouling resistance and use that knowledge to improve the fouling resistance of the energy-efficient RO process. Finally, cleaning protocols targeted toward foulant swelling should be developed and tested with real fouling layers.

Once fouling can be reliably predicted by modeling and removed by cleaning, pretreatment systems can be pared down to a minimum. By combining optimized fouling mitigation with thermodynamically-balanced processes [22] and low-salinity wastewater reuse [152], the desalination systems of the future should be able to produce fresh water at a dramatically reduced energy consumption and environmental footprint relative to seawater desalination today.

Appendix A

Forward osmosis balancing notes

A.1 Efficiency assessment methods

Constructing Fig. 2-2 with data from the open literature required several approximations. In all cases, the permeate was approximated as pure water in the calculation of least work. Also, although water composition varies by application, the feed was assumed to be a sodium chloride solution in the calculation of least exergy and density. Mistry and Lienhard [38] show that only a small error is introduced when calculating the least work of separation of brackish water and seawater as if they were NaCl solutions. Thiel et al. [2] find that NaCl is a reasonable approximation for the osmotic pressure of high-salinity produced water from the Permian Basin, Marcellus, and Nova Scotia shale plays.

Approximations were also made in calculating exergy consumption. The temperature of heat input in the McGinnis et al. [3] system was assumed to be 100 °C (consistent with the use of atmospheric pressure steam for heating) as in [38], and energy and salinity data was taken from the results of the energy consumption trial in [3]. The recovery ratio of the Shuweihat MSF plant is not reported, so a typical value of 33% [41] was used. 33% recovery was also assumed for seawater TVC-MED and MVC, which are evaluated at 3.5% feed salinity. The RO regeneration step in the low-salinity FO-RO pilot was assumed to be 35% efficient (typical of SWRO systems) because of the 4.5% salinity of the diluted draw. The flow rate through the RO unit

was calculated based on conservation of salt and water for the stream salinities given in [1]. The Nicoll seawater FO-RO model [5] assumed a terminal osmotic pressure difference of 1.6 bar, which would require an extraordinarily large membrane area (see Eq. 2.19).

Evaluating the efficiency of the non-regenerating ("osmotic dilution") FO brine concentration system described by Hutchings et al. [4] in such a way that it could be compared to regenerating systems was not straightforward because the plant did not produce pure water. To make this comparison, we borrowed the FO exchanger efficiency defined in Sec. 2.3 (Eq. 2.7) for exchangers within regenerating systems, which relates the least work of separating the feed, as given by Eq. 2.2, to the least exergy required to regenerate the draw (Eq. 2.5) plus the work required to overcome hydraulic losses in the exchanger, $\dot{W}_X$. The osmotic dilution FO efficiency used to compare the Hutchings et al. plant [4] to processes that produce permeate in Fig. 2-2 is given in Eq. A.1:

$$\eta_D = \frac{\dot{m}_{p'} g_{p'} + \dot{m}_c g_c - \dot{m}_f g_f}{\dot{m}_{p'} g_{p'} + \dot{m}_{cd} g_{cd} - \dot{m}_{dd} g_{dd} + \dot{W}_X}. \tag{A.1}$$

Subscripts dc and dd refer to the concentrated and dilute draw solutions, respectively. The subscript p' refers to the water that moves from the stream being concentrated to the draw stream. Under the assumption of no salt permeation, $\dot{m}_{p'} = \dot{m}_f - \dot{m}_c$ and $g_{p'}$ is the pure water Gibbs energy.

A.2 Salt consumption in osmotic dilution

In osmotic dilution systems, reasonably high efficiency is balanced by high salt consumption. Therefore, predicting and minimizing the salt consumption is critical. Although the aforementioned pilot plant consumed a saturated salt solution [1, 4], salt use could be minimized in the osmotic dilution system shown in Fig. A-1, which takes in only solid salt. In a continuous, counterflow system of this type, part of the dilute draw is internally recycled to make the concentrated draw.

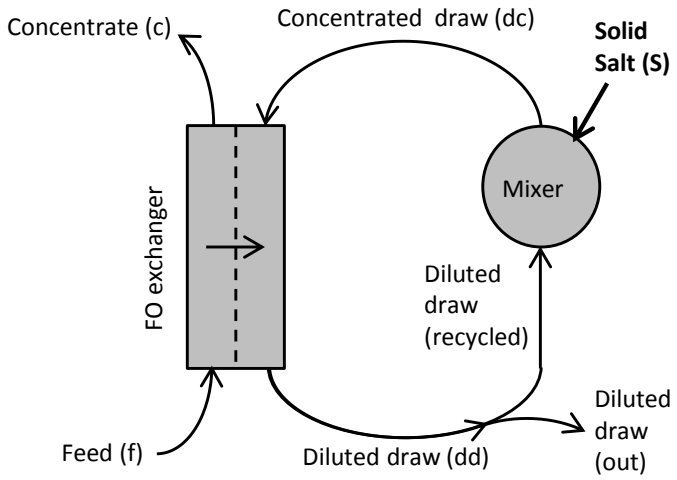

Figure A-1: Osmotic dilution brine concentration system that consumes solid salt

We can define a dimensionless performance parameter, the salt ratio SR, which gives the mass of salt consumed per unit mass of water removed from the feed:

$$\mathrm{SR} \equiv \frac{\dot{m}_S}{\dot{m}_{p'}}. \tag{A.2}$$

Taking conservation of water and salt on the draw side of the system in Fig. A-1, we find that the salt ratio is:

$$\mathrm{SR} = \frac{s_{dd}}{1 - s_{dd}}, \tag{A.3}$$

where s_{dd} is the salinity of the dilute draw stream.

By Eq. A.2, the salt ratio of the osmotic dilution pilot [1] would be 0.075 (75 g NaCl per kg water removed from the feed) based on its dilute draw salinity of 7% [1]. This differs from the system described by Mistry and Lienhard [38] which used the energy of solvation for a salt to power the separation of pure water from saline water. The osmotic dilution system described here consumes less salt per unit water removed from the feed, but it does not produce pure water. Because the salt ratio (Eq. A.3) is only a function of dilute draw salinity, an osmotic dilution system of this type does not benefit from balancing, and only requires that the minimum osmotic pressure difference occurs at the feed side ($\mathrm{MR} \leq \mathrm{MR}^*$).

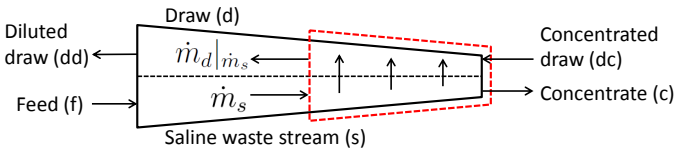

Figure A-2: Schematic diagram of counterflow FO exchanger for balancing analysis

A.3 Salinity profile analysis

Figure A-2 illustrates a control volume analysis of an FO exchanger with a saline stream to be concentrated (subscript s) and a draw stream (subscript d). Mass flow rates and salinities at the feed and concentrated draw inlets are known. Salinities and mass flow rates inside the exchanger are determined as functions of the saline stream mass flow rate, $\dot{m}_s$, at any point in the exchanger, neglecting concentration polarization. These profiles are illustrated in Fig. 2-4.

Making a control volume of the saline side of the FO exchanger in Fig. A-2, conservation of salt determines the salinity as a function of mass flow rate, assuming no salt permeation:

$$s_s|_{\dot{m}_s} = \frac{s_f \dot{m}_f}{\dot{m}_s}. \tag{A.4}$$

Conservation of salt in the draw-side of the FO exchanger, $\dot{m}_d|_{\dot{m}_s}\, s_d|_{\dot{m}_s} = \dot{m}_{dc} s_{dc}$, along with conservation of mass in the control volume with a dashed outline in Fig. A-2, $\dot{m}_s + \dot{m}_{dc} = \dot{m}_c + \dot{m}_d|_{\dot{m}_s}$, leads to the salinity in the draw side as a function of saline stream mass flow rate, Eq. A.5:

$$s_d|_{\dot{m}_s} = \frac{s_{dc}\dot{m}_{dc}}{\dot{m}_{dc} + \dot{m}_s - \dot{m}_c}. \tag{A.5}$$

Evaluating Eq. A.5 at the dilute draw outlet (feed inlet), we find the relationship between dilute and concentrated draw salinities as function of RR and MR, which are defined in Sec. 2.4:

$$\frac{s_{dd}}{s_{dc}} = \frac{\dot{m}_{dc}}{\dot{m}_{dd}} = \frac{\mathrm{MR}}{\mathrm{MR} + \mathrm{RR}} \tag{A.6}$$

Appendix B

Notes on quantifying fouling

B.1 Experimental details

B.1.1 Separating the hydraulic causes from the concentrative causes of flux decline

To separate the hydraulic cause of flux decline (drag) from the concentrative cause (CEOP), the feed solution osmotic pressure was varied for a fixed foulant accumulation in a series of RO tests, allowing both cake structural parameter and pore size to be fit from the experimental data. However, due to the complexation of alginate with calcium and the variation in the complexation type with sodium:calcium ratio [80], varying the osmotic pressure by adding sodium and/or calcium salts could change the size of the pores being measured. Instead, the feed osmotic pressure was varied within individual RO tests by adding glucose, a small, nonionic solute that should not affect alginate structure.

For these tests, an alginate gel cake was formed over a period of four hours on an RO membrane following the procedure described in Sec. 3.3.4, except that the feed spacer is removed to expedite fouling. The feed solution was then replaced with a foulant-free feed solution with the same sodium chloride and calcium chloride concentrations as the initial feed. After the flux was again stabilized, the new flux and feed conductivity were recorded. Glucose was added to reach a concentration of

first 0.05 M, and then 0.1 M. After each addition, stable flux and feed conductivity were measured. The flux and feed conductivity for each glucose concentration were run through the FO model, assuming that the dilute glucose in solution behaves as an ideal solute so that glucose and salt concentration profiles could be superposed. Permeation of glucose through the RO membrane was neglected. The cake structural parameter and pore size were calculated from the best fit of flux at the three glucose concentrations (0, 0.05, and 0.1 M) at each sodium:calcium ratio. The slight decrease in flux that occurs with increasing osmotic pressure may have altered the structural parameter and pore size due to the decreasing cake compression, but this effect was neglected here.

To validate the model, the foulant cake was peeled off the membrane at the end of the test with 0.2 M NaCl and 1 mM $CaCl_2$ and its mass was measured. Assuming the density of the gel is approximately equal to that of water, the thickness was estimated to be 306 μm. This is 9.3% greater than the structural parameter fit with the model for this trial of $S_C = 280$ μm, and given that alginate gels are highly hydrated and thus tend to have porosity and tortuosity near unity (see [63]), a measured thickness that is close to the calculated structural parameter provides some validation for the proposed fouling quantification method for RO. Compression of the cake due to flux through it during structural parameter measurement could have caused the foulant layer to have a structural parameter during RO operation that was smaller than the thickness measured *ex situ*.

The procedure described above was repeated for five sodium chloride concentrations, each with 200 mg/L of sodium alginate and 1 mM of calcium chloride. The pore size and structural parameter for each is fit using the full model (Sec. 3.2) from the flux vs. glucose concentration data, and the average sodium and calcium ion concentrations in the cake layer are calculated. The osmotic pressure increase (CEOP) and hydraulic pressure drop through the gel are also calculated from the model and averaged between the three glucose concentrations to reveal which cause of flux decline dominates. We define the hydraulic loss ratio as the fraction of the change in hydraulic pressure P minus osmotic pressure π across the cake layer that is due to the

difference in hydraulic pressure, $([P_c - P_m]/[P_c - P_m + \pi_m - \pi_c])$, where the subscript c refers to the outer edge of the cake and the subscript m refers to the cake–membrane interface. Although it seems that calcium and sodium concentrations independently influence alginate gel properties, we give pore size and hydraulic loss ratio in terms of sodium:calcium concentration ratio, noting that these values only apply when the calcium ion concentration is on the order of 1 mM.

The calculated pore diameters and hydraulic loss ratios are shown in Fig. B-1. The sodium:calcium ratio is reported as the spatial average ratio within the cake layer, as calculated from the layered model with calcium chloride, sodium chloride, and glucose concentration profiles superimposed, thus neglecting interactions between different solutes. Calculated pore diameters ranged from 4.5 to 20 nm, which is comparable to the range of pore sizes reported for various alginate samples and measurement methods in literature (see Sec. 3.3.3). Pore size increases with increasing sodium:calcium concentration ratio. Hydraulic loss ratio drops from near one at low sodium:calcium ratio to <5% as the sodium:calcium ratio approaches 400, showing that for high sodium concentrations, hydraulic pressure drop can be neglected. The drop in hydraulic loss ratio with increasing sodium concentration at fixed calcium concentration is the result of both increasing pore size, which leads to decreasing hydraulic pressure drop, and increasing feed osmotic pressure, which leads to increasing CEOP.

The cake structural parameter calculated from the model is highly sensitive to pore size when the pore size is low and flux decline is largely due to cake hydraulic drag. To avoid this regime until more precise pore measurements can be made, the minimum feed NaCl concentration considered in this study is 346 mM (2% wt.) so that the hydraulic component of flux decline is less than approximately 10% and the resulting uncertainty in cake structural parameter is minimized. All other concentrations tested are above 400 mM, indicating a hydraulic loss ratio of <5%. Although no higher sodium:calcium ratios were tested, the hydraulic loss ratio is not expected to increase, and a pore size of 20 nm is assumed for all data analysis in the present study. However, future research on the pore size of organic foulants in various ionic environments will be useful for universally-applicable fouling analysis and imperative

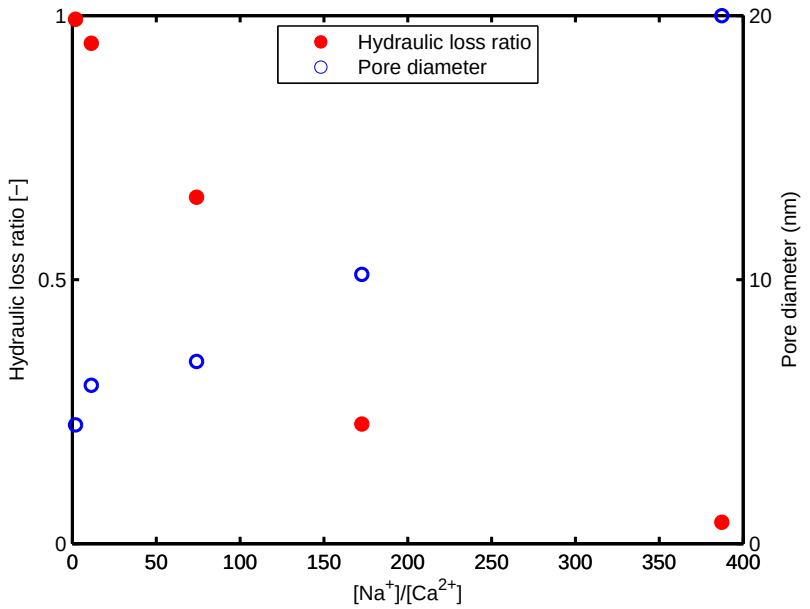

Figure B-1: Calculated hydraulic loss ratio (the fraction of flux decline caused by cake layer hydraulic resistance) and approximate pore diameter for a range of sodium:calcium concentration ratios with 1 mM $CaCl_2$ in the feed.

for the development of predictive modeling.

B.1.2 Membrane characterization

Although membrane properties vary somewhat between coupons, it is not practical to characterize every membrane coupon individually. Salt permeation coefficients were calculated from the manufacturer's specifications, and other properties were characterized experimentally. To account for some variability between membrane samples, the water permeability of each RO coupon and the dispersivity of the FO coupon were fit from the initial flux before foulant cake formation.

FO

The FO membrane's salt permeation coefficient was calculated from its manufacturer specifications [76] and also measured experimentally.

Rejection, R, is specified as 99% and is defined in the membrane's specifications

as:

$$R = 1 - \frac{C_{f,2}V_{f,2} - C_{f,1}V_{f,1}}{(V_{f,1} - V_{f,2})C_{d,ave}}, \tag{B.1}$$

where $V_{f,1}$ and $V_{f,2}$ are the feed volume before and after the test, $C_{f,1}$ and $C_{f,2}$ are the feed salt concentration before and after the test, and $C_{d,ave}$ is the average draw concentration during the test. Assuming values of 5×10^{-5} m/s for mass transfer coefficients on the feed and draw sides during the test, the salt permeation coefficient of the membrane was calculated from $R = 99\%$ using the foulant-free flux equations (Appendix B.2.3) as $B = 5.32 \times 10^{-8}$ m/s.

To experimentally measure salt rejection, the system was run in FO mode for approximately three hours, during which time 159.9 g of liquid moved from the feed to the draw. Initial draw and feed conductivity were measured at 191.1 mS/cm and 59.5 μS/cm, respectively. Final draw and feed conductivities were measured at 184.8 mS/cm and 169.5 μS/cm, respectively. From the foulant-free FO model (Eqs. B.8 and B.9) with the measured flux, feed and draw salinities (averaged between initial and final values), and cross-flow velocities, a salt permeation coefficient of $B = 1.37\times10^{-7}$ m/s was fit from the data, corresponding to a salt rejection of 99.4%. It is unsurprising that the measured salt rejection was higher than the specified salt rejection because the flux was much higher in our test (19.4 lmh vs. 9 lmh), resulting in significant ICP. However, despite our higher salt rejection, the salt permeation coefficient fit from our measurement was higher than that calculated from the specifications. A measurement made in a similarly-sized membrane module by Achilli et al. [15] with a CTA FO membrane from the same supplier found $B = 1.11 \times 10^{-7}$ m/s, which is closer to our measurement. It seems to be common for coupon-sized membrane cells to have higher salt permeation, which is most likely due to increased salt permeability where the membranes are compressed by the sealing o-rings. Because salt transport through the bulk of the membrane (not the edges) affects the foulant cake salinity, we use the value $B = 5.32 \times 10^{-8}$ m/s that was calculated from the manufacturer's test with a larger membrane sample and, presumably, less significant edge effects.

Using the salt permeation coefficient calculated from the FO membrane spec-

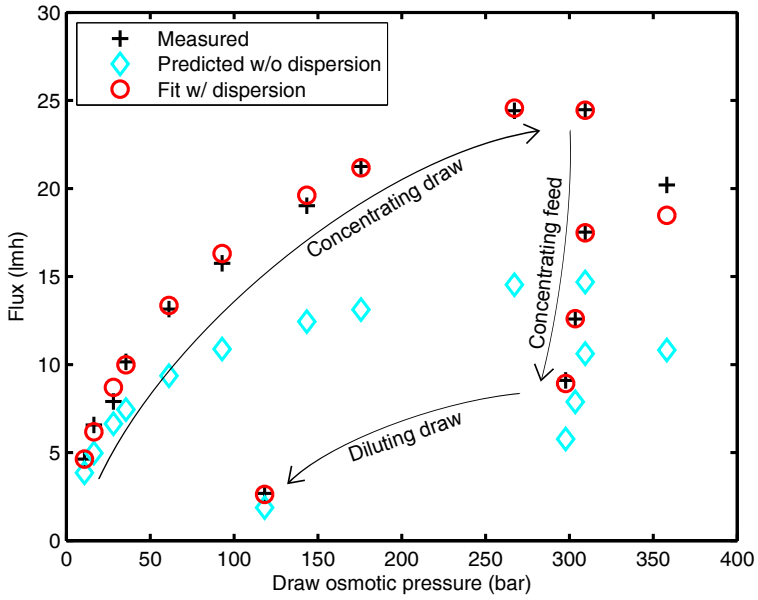

Figure B-2: Plot showing agreement between measured and predicted flux in FO based on a fit of permeability, structural parameter, and dispersivity across a range of feed and draw concentrations. Feed concentrations (not shown) ranged from 0-9% wt. NaCl. Flux predictions for the same experimental conditions using the membrane properties calculated by Achilli et al. [15] without dispersion are given for comparison.

ifications, the water permeability and the support layer structural parameter and dispersivity were fit from data collected from the FO unit over a wide range of feed and draw salinities. Using NaCl feed solutions and degassed NaCl draw solutions of various concentrations, the system was run with membranes in FO orientation (feed contacting active layer) for at least 30 minutes and until a stable flux was reached for each pair of feed and draw salinities. High cross-flow velocity (22.2 cm/s) was used on the feed side to prevent fouling. Feed and draw conductivity were measured for each test, and the parameters of interest were fit from the data and the foulant-free matrix equations (Eqs. B.8 and B.9). The experimental data and corresponding calculated values based on the fitted membrane parameters are shown in Fig. B-2 along with the values that would be calculated using the fitted parameters of Achilli et al. [15] and neglecting dispersion.

The values attained from the fit of the experimental data were $A = 1.9 \times 10^{-12}$

m/s-Pa, $S_S = 5.7 \times 10^{-4}$ m, and $\alpha = 1.65 \times 10^{-4}$ m. The calculated permeability was similar to that measured by Achilli et al. [15] ($A = 1.87 \times 10^{-12}$ m/s-Pa) in a pressurized pure water flux test with a membrane of the same type from the same manufacturer. The structural parameter fit by Achilli et al. was slightly greater than our value ($S_S = 6.78 \times 10^{-4}$ m), but agrees in order of magnitude. Figure B-2 shows that with the membrane parameters fitted by Achilli et al. (with $\alpha = 0$ because dispersion was not considered), the outcome is relatively well-predicted when the flux and draw osmotic pressure are low, but does not capture the behavior at high flux or high draw osmotic pressure. The fitted dispersion coefficient, as defined in Eq. 3.14, is within the range that would be expected for this membrane: using the the ratio $\tau_S/\epsilon_S = S_S/\delta_S = 7.125$ (based on measured membrane thickness), Eq. 3.15 gives an estimate of 6.5 μm for the product of pore diameter and inhomogeneity factor in the support layer, which is somewhat smaller than but comparable in order of magnitude to the pore sizes seen in micrographs [66] of the same type of FO membrane used here.

RO

Based on the measured feed conductivity and permeate mass and conductivity before and after eight hours of running RO with 3.5% NaCl feed, the salt rejection of the membrane module was estimated as 99.55%, which is close to the membrane's minimum rated salt rejection of 99.65% [153]. As with the FO membrane, the decrease in rejection is attributed to the small scale of the module and the rated rejection is used to calculate salt permeation coefficient. Using the foulant-free RO equations and the test conditions reported in the membrane data sheet [153], the salt permeation coefficient was determined to be $B = 2.38 \times 10^{-8}$ m/s. Permeability, which varied between samples, was fit for each coupon from the flux before fouling.

B.1.3 Mass transfer coefficients

Convective mass transfer affects flux in both FO and RO, but it is especially important to have a good estimate for the draw side mass transfer coefficient in FO because the high draw concentration results in a large concentration difference across the boundary layer (see Figs. 3-3 and 3-4). Mass transfer coefficients vary widely between studies, so for the purpose of analyzing the present experimental results, mass transfer coefficients were measured using the present experimental setup in an RO configuration. Flux was measured first with deionized water feed (no concentration polarization), and then with 3.5% wt. NaCl with the set of two fine spacers used in the draw channel in FO at two flow rates and with the coarse spacer used in the feel channels at one flow rate. The pulsation dampener typically used in the feed side of the apparatus was removed to simulate the pulsating flow that occurs in the draw channel.

The wetted area of the membrane is slightly larger than the channel area because of the offset O-ring. The O-ring meets the membrane 3.5 mm beyond the edge of the feed channel at the end of a gap less than 100 μm thick. In the absence of concentration polarization (i.e., in the pure water RO test mentioned above), we assume that the membrane in the gap is active; however, with saline feeds, we assume that the concentration polarization within the gap is so severe that the water permeation in the gap is negligible.

Using the foulant-free model (Appendix B.2.3) and the measured fluxes, the mass transfer coefficients were calculated to be 1.121×10^{-4} and 2.89×10^{-5} m/s for the twin fine spacers with feed velocities of 23.9 and 4.3 cm/s, respectively. The mass transfer coefficient with the single coarse spacer was measured as 3.61×10^{-5} m/s with a flow velocity of 8.3 cm/s. A correlation for long, spacer-filled channels by Koutsou et al. [154] gives mass transfer coefficients of a similar magnitude. In the absence of a correlation for developing, pulsating flow in channels with the present spacers, we assume a correlation of the form

$$\mathrm{Sh}_{D_h} \propto [(D_h/l)\mathrm{Re}_{D_h}\mathrm{Sc}]^n \tag{B.2}$$

and fit the exponent n from the two flow velocities with the twin fine spacers as 0.79. In Eq. B.2, D_h is the channel hydraulic diameter, Sh_{D_h} is the Sherwood number, Sc is the Schmidt number, and l is the channel length. For the present analysis of experimental data, we use the following correlations for mass transfer coefficient, where v is the cross-flow velocity, which are based on the form of Eq. B.2 with values measured experimentally: Eq. B.3 for the twin fine spacers and Eq. B.4 for the coarse spacer.

$$k_{\mathrm{fine}} = 1.121 \times 10^{-4}\ [\mathrm{m/s}] \times \left(\frac{v}{0.239\ [\mathrm{m/s}]}\right)^{0.79} \tag{B.3}$$

$$k_{\mathrm{coarse}} = 3.61 \times 10^{-5}\ [\mathrm{m/s}] \times \left(\frac{v}{0.083\ [\mathrm{m/s}]}\right)^{0.79} \tag{B.4}$$

There are several outstanding issues with the use of these empirical correlations in analyzing the present experiment. Although the mass transfer coefficients were measured in pulsating flow to simulate conditions in the draw channel, these correlations are also used in the feed channel, where the pulsation dampener significantly reduces flow oscillations. The direction of permeation velocity is opposite between the feed and draw channels, although the permeation velocity is very small compared to the cross-flow velocity (μm/s rather than cm/s). The difference in viscosity between alginate-containing feed solutions and foulant-free feeds is not accounted for, nor is the difference in sodium chloride diffusion coefficient between different boundary layer concentrations. Further investigation of mass transfer coefficients in spacer-filled channels will be beneficial for fouling prediction, but it is beyond the scope of the present work.

B.1.4 Accounting for time-varying solution concentrations

Even in the absence of fouling, flux is expected to decline in this experiment because the feed and draw concentrations are not controlled. Instead, feed and draw concentrations are predicted over time using conservation of species based on changes in measured permeate/draw mass and assuming negligible salt permeation or evaporation.

Cake structural parameter is calculated from the theory in Sec. 3.2 based on the feed and, in FO, draw solution concentrations computed from the change in scale mass. Foulant-free flux is predicted based on the calculated feed and draw concentrations using the foulant-free matrix equations given in Appendix B.2.3. Flux decline is then calculated as the ratio of measured flux to predicted foulant-free flux.

B.1.5 Uncertainty analysis

Flux decline and cake structural parameter are both calculated from measured flux, which itself has several sources of uncertainty. Here, we estimate the 95% confidence interval for our flux decline and cake structural parameter measurements using the propagation of uncertainty method.

Flux uncertainty arises from high-frequency fluctuations, low-frequency thermal fluctuations, and possible changes in membrane properties over time. In the present experiments, measured flux varies at a high frequency with an amplitude of about 0.10 lmh for RO and 0.19 lmh for FO (the standard deviation of flux measurements every 5 minutes for one hour at the end of a test when the flux decline was very slow). Based on the statistical uncertainty method with 12 measurements, this would indicate a 95% confidence interval of ± 0.22 lmh in RO ± 0.41 lmh in FO for these fluctuations, which seem to occur due to the low resolution of the digital scale compared to the mass flow into it during the 15 minute flux measurement interval. The larger variation in FO may be partly explained by the connection of the draw volume on the scale to the draw loop, whose volume fluctuates slightly due to the motions of the diaphragm pump. Flux also seems to vary over a period of hours, which is likely due to fluctuations in temperature. The temperature control system maintains the temperature between 20 and 21 °C. According to the model of Jin et al. [155] for RO membrane permeability temperature dependence, this difference should result in a $\pm 1.2\%$ permeability variation. Neglecting the effects of other layers on flux, the solution–diffusion model [61] would thus predict a $\pm 1.2\%$ variability in flux due to imperfect temperature control. Membrane properties could also change due to incomplete conditioning before beginning experiments, and to account for this, an

uncertainty of ±1% of flux is assumed. Propagation of uncertainty leads to a 95% confidence interval of approximately 2.5% of flux in RO and 4.0% of flux in FO based on the initial flux range of the present experiments.

Flux decline is the ratio of measured flux to predicted foulant-free flux. The latter is based on permeability measured from the initial flux, so the flux uncertainty applies to both measurements. The propagation of uncertainty method then dictates that the 95% confidence interval in flux decline is ±3.6 and ±5.7 percentage points in RO and FO, respectively.

Structural parameter uncertainty is based on uncertainties in flux and initial flux plus uncertainty in the assumption of 20 nm foulant pore size. The error in S_C due to the assumed 20 nm pore size is estimated to be 5% in the lowest salinity (2% NaCl) RO trial, and 2% for the higher salinity trials, where the effect of cake hydraulic resistance becomes negligible (see Fig. B-1). The change in calculated structural parameter based on a small change in measured flux varies depending on many variables, but to provide an estimate of the uncertainty for all trials, this derivative is calculated numerically for representative FO and RO cases near the end of the fouling run ($S_C \approx 100$ μm for RO and $S_C \approx 200$ μm for FO) as 1.64×10^{-5} m/lmh for RO and 3.14×10^{-5} m/lmh for FO. The greater change in cake structural parameter needed to change the flux by a given amount in FO is primarily due to the effect of internal concentration polarization. Propagation of uncertainty considering uncertainties in flux, initial flux, and pore size leads to the following 95% confidence intervals in cake structural parameter: ±40 μm for the FO test, ±14 μm for RO with 2% NaCl, and ±13 μm for the other (higher-salinity) RO tests.

There may be additional uncertainty in structural parameter due to uncertainty in dispersivity in the support layer and mass transfer coefficients in the feed and draw channels. Further research is needed in these areas.

B.2 Modeling details

B.2.1 Concentration-dependence of membrane water permeability

According to the solution–diffusion model, membrane water permeability scales with feed water concentration [61]. Therefore, to more accurately predict foulant accumulation from flux decline, we correct for the change in water permeability as the water concentration at the membrane, $C_{w,m}$, changes due to CEOP using Eq. B.5 for $A|_{C_m}$:

$$A|_{C_m} = A|_{C_{m,0}} \frac{C_{w,m}}{C_{w,m,0}} = A|_{C_{m,0}} \frac{\rho|_{C_m}(1 - s|_{C_m})}{\rho|_{C_{m,0}}(1 - s|_{C_{m,0}})}, \tag{B.5}$$

where $C_{w,m,0}$ and $C_{m,0}$ are the water and salt concentrations present when permeability was evaluated and s is the salt mass fraction. The dependence of permeability on water concentration results from the way permeability is defined: although flux is proportional to the gradient in solvent concentration within the membrane [61], permeability is defined as the ratio of flux to hydraulic–osmotic pressure difference outside the membrane. In Eq. B.5, any potential reduction in water concentration due to displacement by the foulant material is neglected in the current form of the model because of the high porosity of the alginate gels considered experimentally. However, the effect of nanostructured gels on water activity and membrane permeability could be a worthwhile subject for future investigation.

B.2.2 Diffusion coefficients

The NaCl diffusion coefficient itself varies about 10% across the range from dilute to saturated solutions [71], and the diffusion coefficient is generally higher on the draw side of the membrane. The variation in diffusion coefficient is taken into account by using roughly average values of diffusion coefficient in the support layer and foulant cake layer of $D_S = 1.3673 \times 10^{-9}$ m^2/s and $D_C = 1.2939 \times 10^{-9}$ m^2/s, respectively. These values are based on the data of Vitagliano and Lyons [71] at 25 °C and corrected

to 20 °C (the temperature maintained in our experiments) using the Stokes–Einstein relation.

B.2.3 Layered model matrix equations

The systems of equations presented herein for the layered transport models of FO and RO can be reduced to one equation each for the salt continuity and water flux, but the complexity of the salt flux equation increases with the number of layers. For the five-layer fouled FO model, we combine the equations for salt flux into a matrix equation that can be solved simultaneously with the corresponding equation for water flux in MATLAB. The matrix equation is created by subtracting the equation for salt flux through the active layer from each of the other salt flux equations. Some terms in the fouled equations are undefined when there is no foulant layer ($S_C = 0$), so equations for flux in the absence of fouling are also given here.

For FO with fouling, Eqs. B.6 and B.7 are solved simultaneously.

$$\begin{bmatrix} \frac{-J_w}{\exp(J_w/k_F)-1} & -B & B & 0 \\ \frac{J_w \exp(J_w S_C/D_C)}{\exp(J_w S_C/D_C)-1} & \frac{-J_w}{\exp(J_w S_C/D_C)-1} - B & B & 0 \\ 0 & -B & \frac{J_w \exp(J_w S_S/D_{S,\text{eff}})}{\exp(J_w S_S/D_{S,\text{eff}})-1} + B & \frac{-J_w}{\exp(J_w S_S/D_{S,\text{eff}})-1} \\ 0 & -B & B & \frac{J_w \exp(J_w/k_D)}{\exp(J_w/k_D)-1} \end{bmatrix} \times \begin{bmatrix} C_c \\ C_m \\ C_s \\ C_b \end{bmatrix} = \begin{bmatrix} \frac{-J_w C_f \exp(J_w/k_F)}{\exp(J_w/k_F)-1} \\ 0 \\ 0 \\ \frac{J_w C_d}{\exp(J_w/k_D)-1} \end{bmatrix} \quad \text{(B.6)}$$

$$J_w = A|_{C_m}(\pi|_{C_s} - \pi|_{C_m} - \frac{32\mu S_C J_w}{D_{h,C}^2}); \quad \text{(B.7)}$$

Note that $D_{S,\text{eff}}$ is itself a function of J_w (Eq. 3.14).

For FO without fouling, the equations to solve are Eqs. B.8 and B.9.

$$\begin{bmatrix} \frac{-J_w}{\exp(J_w/k_F)-1} - B & B & 0 \\ -B & \frac{J_w \exp(J_w S_S/D_{S,\text{eff}})}{\exp(J_w S_S/D_{S,\text{eff}})-1} + B & \frac{-J_w}{\exp(J_w S_S/D_{S,\text{eff}})-1} \\ -B & B & \frac{J_w \exp(J_w/k_D)}{1-\exp(J_w/k_D)-1} \end{bmatrix} \times \begin{bmatrix} C_m \\ C_s \\ C_b \end{bmatrix} = \begin{bmatrix} \frac{-J_w C_f \exp(J_w/k_F)}{\exp(J_w/k_F)-1} \\ 0 \\ \frac{J_w C_d}{\exp(J_w/k_D)-1} \end{bmatrix} \tag{B.8}$$

$$J_w = A|_{C_m}(\pi|_{C_s} - \pi|_{C_m}) \tag{B.9}$$

For RO with fouling, Eqs. B.10 and B.11 are solved simultaneously.

$$\begin{bmatrix} \frac{-J_w}{\exp(J_w/k_F)-1} & -B & B \\ \frac{J_w \exp(J_w S_C/D_C}{\exp(J_w S_C/D_C)-1} & \frac{-J_w}{\exp(J_w S_C/D_C)-1} - B & B \\ 0 & -B & J_w + B \end{bmatrix} \times \begin{bmatrix} C_c \\ C_m \\ C_p \end{bmatrix} = \begin{bmatrix} \frac{-J_w C_f \exp(J_w/k_F)}{\exp(J_w/k_F)-1} \\ 0 \\ 0 \end{bmatrix} \tag{B.10}$$

$$J_w = A|_{C_m}\Big(P_f - \frac{32\mu S_C J_w}{D_{h,C}^2} - [\pi|_{C_m} - \pi|_{C_p}]\Big) \tag{B.11}$$

For RO without fouling, Eqs. B.12 and B.13 can be used.

$$\begin{bmatrix} \frac{-J_w}{(\exp(J_w/k_F))-1} - B & B \\ -B & J_w + B \end{bmatrix} \times \begin{bmatrix} C_m \\ C_p \end{bmatrix} = \begin{bmatrix} \frac{-J_w C_f \exp(J_w/k_F)}{\exp(J_w/k_F)-1} \\ 0 \end{bmatrix} \tag{B.12}$$

$$J_w = A|_{C_m}(P_f - [\pi|_{C_m} - \pi|_{C_p}]) \tag{B.13}$$

Once the equations for water flux and concentrations have been solved simultaneously, salt flux (if desired) can be calculated from one of the algebraic equations for salt flux in Sec. 3.2, e.g., Eq. 3.9 for FO or Eq. 3.17 for RO.

B.2.4 Concentration and pressure profile equations

The layered transport model allows for the evaluation of concentration and pressure profiles throughout the various layers in fouled FO and RO. In this section, we present equations for concentration and pressure profiles based on interface concentrations and pressures, which must be calculated first using the equations in Sec. 3.2 or B.2.3. The equations given here are based on distance, x, which increases in the direction

of water flow and originates at the feed side of the membrane active layer.

To compute the concentration and pressure profiles, the thickness of the various layers must be known. The thickness of the feed and draw boundary layers can be computed from the mass transfer coefficients as $\delta_F = D_C/k_F$ and $\delta_D = D_S/k_D$, respectively, assuming the average diffusion coefficients in the porous layers are similar to those in the neighboring boundary layers. The membrane active layer, which is around $\delta_A = 200$ nm thick in RO membranes [156], is very thin compared to the other layers. The support layer thickness of a membrane can be measured with calipers or a micrometer, assuming that the contribution of the active layer to the thickness is negligible. The RO and FO membranes used in the present experiments were measured with calipers to be 150 and 80 μm thick, respectively. The thickness of the foulant cake can be measured experimentally or estimated from the calculated cake structural parameter and values of porosity and tortuosity taken from the literature (e.g., [63]), but the high porosity and correspondingly low tortuosity of alginate gels suggest that $\delta_C = S_C$ is a reasonable first approximation in many cases.

For FO, the concentration and (gauge) pressure profiles are piecewise equations (Eqs. B.14 and B.15) based on the models for each layer as shown in Fig. 3-1. The equations for the cake layer ($-\delta_C \leq x < 0$) assume that the pore size, tortuosity, and porosity are uniform within the cake layer, but future work may relax this assumption. The sorption coefficient, K, that appears in the active layer is a result of the solution–diffusion model [61].

$$C(x) = \begin{cases} C_f & x \leq -(\delta_F + \delta_C) \\ C_f + (C_c - C_f)\frac{\exp([x+\delta_F+\delta_C]J_w/D_C)-1}{\exp(\delta_F J_w/D_C)-1} & -(\delta_F + \delta_C) \leq x \leq -\delta_C \\ C_c + (C_m - C_c)\frac{\exp([x+\delta_C]J_w S_C/[D_C\delta_C])-1}{\exp(S_C J_w/D_C)-1} & -\delta_C \leq x < 0 \\ K(C_m + \frac{x}{\delta_A}[C_s - C_m]) & 0 < x < \delta_A \\ C_s + (C_b - C_s)\frac{\exp([x-\delta_A]J_w S_S/[D_{S,\text{eff}}\delta_S])-1}{\exp(S_S J_w/D_{S,\text{eff}})-1} & \delta_A < x \leq \delta_A + \delta_S \\ C_b + (C_d - C_b)\frac{\exp([x-\delta_A-\delta_S]J_w/D_S)-1}{\exp(\delta_D J_w/D_S)-1} & \delta_A + \delta_S \leq x \leq \delta_A + \delta_S + \delta_D \\ C_d & x \geq \delta_A + \delta_S + \delta_D \end{cases} \tag{B.14}$$

$$P(x) = \begin{cases} 0 & x \leq -\delta_C \\ -\frac{x+\delta_C}{\delta_C}\frac{32\mu S_C J_w}{D_{h,C}^2} & -\delta_C \leq x \leq 0 \\ -\frac{32\mu S_C J_w}{D_{h,C}^2} & 0 \leq x < \delta_A \\ 0 & x > \delta_A \end{cases} \tag{B.15}$$

The RO concentration and (gauge) pressure profiles are given in Eqs. B.16 and B.17.

$$C(x) = \begin{cases} C_f & x \leq -(\delta_F + \delta_C) \\ C_f + (C_c - C_f)\frac{\exp([x+\delta_F+\delta_C]J_w/D_C)-1}{\exp(\delta_F J_w/D_C)-1} & -(\delta_F + \delta_C) \leq x \leq -\delta_C \\ C_c + (C_m - C_c)\frac{\exp([x+\delta_C]J_w S_C/[D_C\delta_C])-1}{\exp(S_C J_w/D_C)-1} & -\delta_C \leq x < 0 \\ K(C_m - \frac{x}{\delta_A}[C_m - C_p]) & 0 < x < \delta_A \\ C_p & x > \delta_A \end{cases} \tag{B.16}$$

$$P(x) = \begin{cases} P_f & x \leq -\delta_C \\ P_f - \frac{x+\delta_C}{\delta_C}\frac{32\mu S_C J_w}{D_{h,C}^2} & -\delta_C \leq x \leq 0 \\ P_f - \frac{32\mu S_C J_w}{D_{h,C}^2} & 0 \leq x < \delta_A \\ 0 & x > \delta_A \end{cases} \tag{B.17}$$

Appendix C

Notes on the effect of pressure

C.1 Normalized flux

Plots of normalized flux are included in this appendix for completeness. Because the feed and draw concentrations evolve in time, normalized flux is defined as a ratio of the measured flux to the flux expected in the absence of foulants. The expected flux in the absence of foulants is predicted using our foulant-free FO model of Ref. [14], which was validated against flux measurements over a range of feed and draw concentrations encompassing the feed and draw concentrations used in the present study. During fouling, the feed and draw concentrations, from which the foulant-free flux is computed, are calculated from the change in draw mass, assuming negligible salt permeation. For the foulant-free flux calculation, membrane properties are assumed to be equivalent to those reported in [14], except for the support layer dispersivity, which is fit from the initial flux of each membrane coupon just after the addition of alginate. Although initial flux varied somewhat between membrane coupons, flux decline is computed relative to a fixed flux because foulant advection toward the membrane is proportional to flux [100].

In the following figures, flux is normalized by the minimum initial flux of the set of trials compared at a given salinity. The reported normalized flux, J_{norm}, at time t

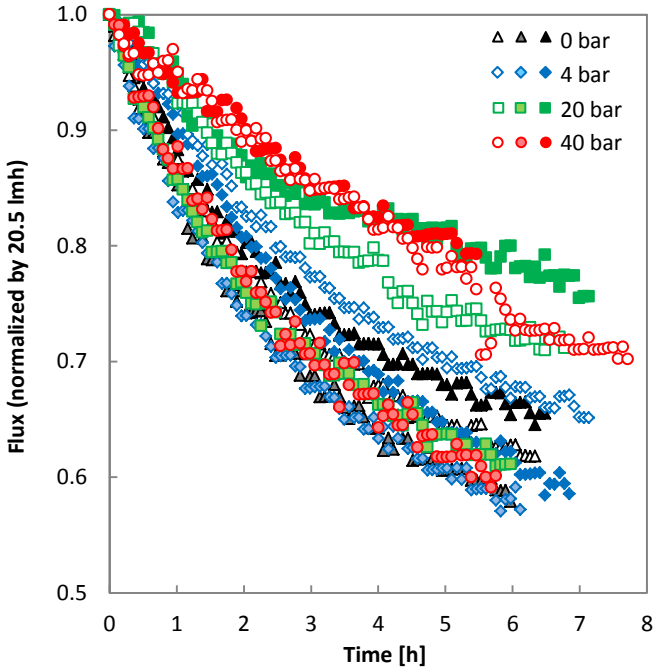

Figure C-1: Experimental flux decline curves for FO fouling at various pressures with a low-salinity feed (29 mM NaCl, 1 mM $CaCl_2$, and 200 mg/L alginate) and no feed spacer. Flux is normalized by 20.5 lmh. Duplicate trials are denoted by empty and filled symbols of the same shape and color.

is computed using the following equation:

$$J_{\text{norm}}(t) = \frac{J_w(t+t^\star)}{J_w^\star} \times \frac{J_{w,0}(t^\star)}{J_{w,0}(t+t^\star)}, \tag{C.1}$$

where J_w is the measured water flux, $J_w^\star$ is the designated normalization flux, the subscript 0 denotes predicted foulant-free flux, and $t^\star$ is the time at which the measured flux reaches the normalization flux. In this way, all trials have a normalized flux of 1 when $t = 0$, and flux measurements before each trial reached the normalization flux are still shown, but as $J_{\text{norm}} > 1$ when $t < 0$. We employed and justified the use of the same normalization procedure in our previous report comparing FO and RO fouling [14].

Normalized flux during fouling (normalized by 20.5 lmh, the lowest starting flux of the 12 trials, using Eq. C.1) for the low-salinity fouling trials shown in Figs. 4-6 and 4-7 are shown in Fig. C-1. The 95% confidence interval in normalized flux measurements

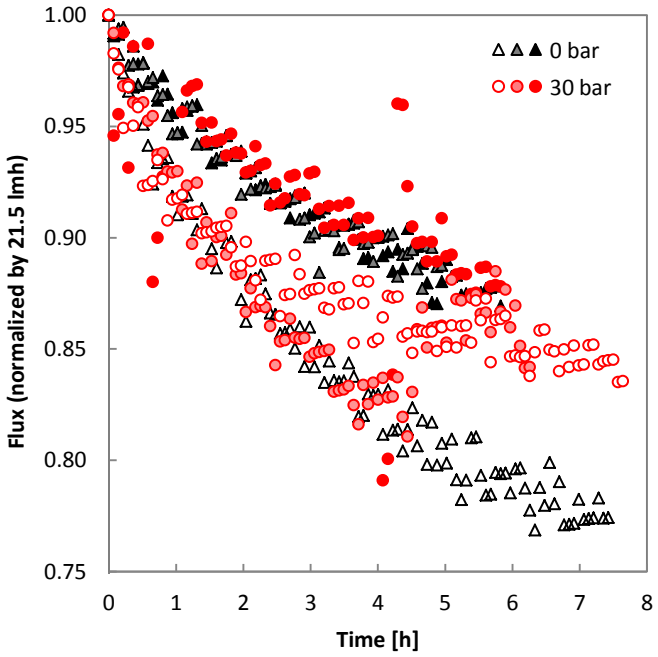

Figure C-2: Experimental flux decline curves for FO fouling with a feed spacer at various pressures with a medium-salinity feed (174 mM NaCl, 1 mM $CaCl_2$, and 200 mg/L alginate). Flux is normalized by 21.5 lmh. Duplicate trials are denoted by empty and filled symbols of the same shape and color.

is approximately 0.04, as discussed in C.3. Even when the flux decline is normalized in this way, there is significant variation between the rates of flux decline between different trials. The difference in flux decline rate does not appear to be correlated to pressure as much as it is to initial flux, as shown in Fig. 4-7.

Figure C-2 shows a similar set of normalized flux measurements (normalized by 21.5 lmh, the lowest starting flux of the 6 trials, using Eq. C.1) for the moderate salinity trials shown in Figs. 4-9 and 4-10. There is no clear effect of pressure on flux decline rate, although none was predicted for this water composition (see Sec. 4.2).

C.2 Cleaning effectiveness

The removal of foulant from the FO membrane by cleaning (using the protocol described in Sec. 4.3.3) is represented by a cleaning effectiveness, ϵ_c, which is calculated

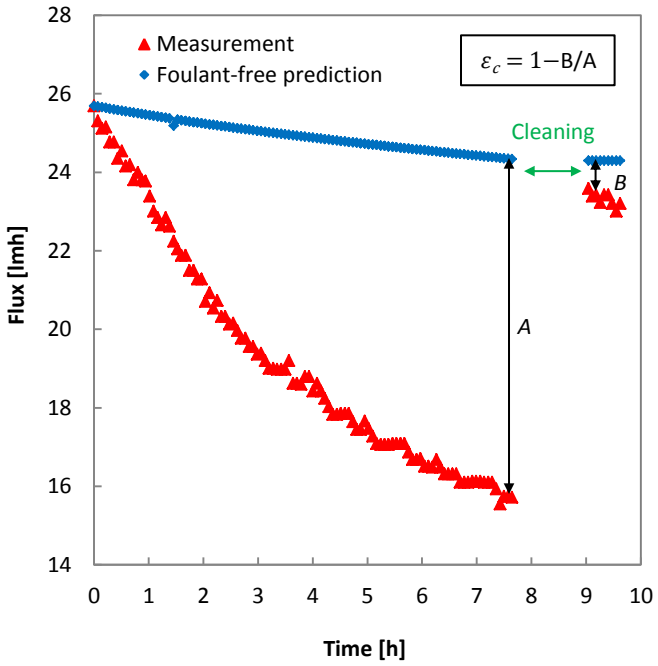

Figure C-3: Sample data for flux decline and recovery along with predicted foulant-free flux to illustrate the definition of cleaning effectiveness used in this study.

from the change in normalized flux due to cleaning as defined in Eq. C.2:

$$\epsilon_c = \frac{J_{w,a}/J_{w,a,0} - J_{w,b}/J_{w,b,0}}{1 - J_{w,b}/J_{w,b,0}}, \tag{C.2}$$

where J_w is the water flux, the subscript 0 refers to the foulant-free flux prediction, and the subscripts b and a refer to before and after cleaning, respectively. Similar definitions have been used in previous studies to quantify the recovery of flux by cleaning [12, 72]. The cleaning effectiveness is represented graphically in Fig. C-3 using actual flux measurements and foulant-free flux predictions for one trial at 40 bar. Permeate flow between 15 and 30 minutes after the conclusion of the cleaning step is used in calculating flux after cleaning and cleaning effectiveness. The uncertainty in cleaning effectiveness is discussed in C.3.

C.3 Uncertainty analysis

Using the method of propagation of uncertainty (see [157]) and the definition of cleaning effectiveness (Eq. C.2), the uncertainty (as a 95% confidence interval) in cleaning effectiveness, u_{ϵ_c}, can be expressed in terms of uncertainties in normalized flux before and after cleaning:

$$u_{\epsilon_c} = \sqrt{\left(u_{(J_{w,a}/J_{w,a,0})}\frac{\partial \epsilon_c}{\partial(J_{w,a}/J_{w,a,0})}\right)^2 + \left(u_{(J_{w,b}/J_{w,b,0})}\frac{\partial \epsilon_c}{\partial(J_{w,b}/J_{w,b,0})}\right)^2}. \tag{C.3}$$

Our previous report [14] showed that the 95% confidence interval in normalized FO flux for the present apparatus was approximately ± 0.04. Using this value for uncertainty in normalized flux both before and after cleaning ($u_{(J_{w,a}/J_{w,a,0})} = u_{(J_{w,b}/J_{w,b,0})} = 0.04$), and evaluating derivatives based on Eq. C.2:

$$\frac{\partial \epsilon_c}{\partial(J_{w,a}/J_{w,a,0})} = \frac{1}{1 - J_{w,b}/J_{w,b,0}} \tag{C.4}$$

and

$$\frac{\partial \epsilon_c}{\partial(J_{w,b}/J_{w,b,0})} = \frac{1 - J_{w,a}/J_{w,a,0}}{(1 - J_{w,b}/J_{w,b,0})^2}, \tag{C.5}$$

the 95% confidence interval in cleaning effectiveness can be estimated by Eq. C.6:

$$u_\epsilon = \frac{0.04}{1 - J_{w,b}/J_{w,b,0}}\sqrt{1 + \left(\frac{1 - J_{w,a}/J_{w,a,0}}{1 - J_{w,b}/J_{w,b,0}}\right)^2}. \tag{C.6}$$

Appendix D

System comparison experimental conditions

Tables D.1 and D.2 contain the experimental conditions of all scaling and organic fouling trials, respectively. Operating conditions (e.g., temperature) refer to the bulk feed at the module outlet. Operating pressure varied between RO experiments because of differences in membrane permeability between two sheets ordered on different dates. Although not included in Table D.2, the feed solution in all organic fouling trials contained 200 mg/L sodium alginate, 1 mM $CaCL_2$, and 50 mM NaCl.

Table D.1: Inorganic fouling experimental conditions

System	$[CaSO_4]_{bulk}$ (mM)	Temp. (°C)	Pressure (bar)	Initial flux (lmh)	Fouled?
RO	15.2	20	13.75	19.4	No
RO	19.3	20	13.75	19.7	No
RO	21.6	20	13.75	19.7	No
RO	23.7	20	23	19.7	Yes
RO	29.3	20	27.5	19.3	Yes
FO	23.7	20	0	20.2	No
FO	29.3	20	0	19.0	No
FO	36.3	20	0	19.4	Yes
FO	43.5	20	0	18.7	Yes
MD	23.7	60	0	19.0	No
MD	26.5	60	0	16.3	No
MD	29.3	60	0	18.9	Yes
MD	36.3	60	0	20.2	Yes

Table D.2: Organic fouling experimental conditions.

System	Temp. (°C)	Pressure (bar)	Initial flux (lmh)
RO	25	16.25	17.1
FO	25	0	18.7
MD	60	0	16.8

Bibliography

[1] Bryan D. Coday, Pei Xu, Edward G. Beaudry, Jack Herron, Keith Lampi, Nathan T. Hancock, and Tzahi Y. Cath. The sweet spot of forward osmosis: Treatment of produced water, drilling wastewater, and other complex and difficult liquid streams. *Desalination*, 333(1):23–35, 2014.

[2] Gregory P. Thiel, Emily W. Tow, Leonardo D. Banchik, Hyung Won Chung, and John H. Lienhard V. Energy consumption in desalinating produced water from shale oil and gas extraction. *Desalination*, 366:94–112, 2015.

[3] Robert L. McGinnis, Nathan T. Hancock, Marek S. Nowosielski-Slepowron, and Gary D. McGurgan. Pilot demonstration of the NH3/CO2 forward osmosis desalination process on high salinity brines. *Desalination*, 312:67–74, 2013.

[4] Nathan R. Hutchings, Eric W. Appleton, and Robert A. McGinnis. Making high quality frac water out of oilfield waste. In *Proceedings of the International Society of Petroleum Engineers 2010 Annual Technical Conference and Exhibition*, Florence, Italy, September 19-22, 2010.

[5] Peter G. Nicoll. Forward osmosis as a pre-treatment to reverse osmosis. In *Proceedings of the International Desalination Association World Congress on Desalination and Water Reuse*, Tianjin, China, Oct 20-25, 2013. Paper #TIAN13-121.

[6] DesalData, desaldata.com/projects, accessed 2014.

[7] Daniel Hoffman. The application of solar energy for large-scale seawater desalination. *Desalination*, 89(2):115–183, 1992.

[8] Tom Hayes and Blaine F. Severin. Evaluation of the aqua pure mechanical vapor recompression system in the treatment of shale gas flowback water: Barnett and appalachian shale water management and reuse technologies. Technical Report 08122-05.11, Research Partnership to Secure Energy in America, 2012.

[9] Sangyoup Lee, Chanhee Boo, Menachem Elimelech, and Seungkwan Hong. Comparison of fouling behavior in forward osmosis (FO) and reverse osmosis (RO). *Journal of Membrane Science*, 365(1–2):34–39, 2010.

[10] Baoxia Mi and Menachem Elimelech. Organic fouling of forward osmosis membranes: Fouling reversibility and cleaning without chemical reagents. *Journal of Membrane Science*, 348(1–2):337–345, 2010.

[11] Yeowon Kim, Menachem Elimelech, Ho Kyong Shon, and Seungkwan Hong. Combined organic and colloidal fouling in forward osmosis: Fouling reversibility and the role of applied pressure. *Journal of Membrane Science*, 460:206–212, 2014.

[12] Ming Xie, Jongho Lee, Long D. Nghiem, and Menachem Elimelech. Role of pressure in organic fouling in forward osmosis and reverse osmosis. *Journal of Membrane Science*, 493:748–754, 2015.

[13] Emily W. Tow, Martin M. Rencken, and John H. Lienhard V. In situ visualization of organic fouling and cleaning mechanisms in reverse osmosis and forward osmosis. *Desalination*, 399:138–147, 2016.

[14] Emily W. Tow and John H. Lienhard V. Quantifying osmotic membrane fouling to enable comparisons across diverse processes. *Journal of Membrane Science*, 511:92–107, 2016.

[15] Andrea Achilli, Tzahi Y. Cath, and Amy E. Childress. Power generation with pressure retarded osmosis: An experimental and theoretical investigation. *Journal of Membrane Science*, 343(1–2):42–52, 2009.

[16] Charles J. Vörösmarty, Pamela Green, Joseph Salisbury, and Richard B. Lammers. Global water resources: Vulnerability from climate change and population growth. *Science*, 289(5477):284–288, 2000.

[17] Karan H. Mistry, Ronan K. McGovern, Gregory P. Thiel, Edward K. Summers, Syed M. Zubair, and John H. Lienhard V. Entropy generation analysis of desalination technologies. *Entropy*, 13(10):1829–1864, 2011.

[18] Anand K. Plappally and John H. Lienhard V. Energy requirements for water production, treatment, end use, reclamation, and disposal. *Renewable and Sustainable Energy Reviews*, 16(7):4818–4848, 2012.

[19] John H. Lienhard V, Gregory P. Thiel, David E. M. Warsinger, and Leonardo D. Banchik (eds.). Low carbon desalination: Status and research, development, and demonstration needs, report of a workshop conducted at the Massachusetts Institute of Technology in association with the Global Clean Water Desalination Alliance, MIT Abdul Latif Jameel World Water and Food Security Lab, Cambridge, Massachusetts, 2016.

[20] Emily W. Tow, Ronan K. McGovern, and John H. Lienhard V. Raising forward osmosis brine concentration efficiency through flow rate optimization. *Desalination*, 366:71–79, 2015.

[21] David Cohen-Tanugi, Ronan K. McGovern, Shreya H. Dave, John H. Lienhard V, and Jeffrey C. Grossman. Quantifying the potential of ultra-permeable membranes for water desalination. *Energy & Environmental Science*, 7:1134–1141, 2014.

[22] David M. Warsinger, Emily W. Tow, Kishor G. Nayar, Laith A. Maswadeh, and John H. Lienhard V. Energy efficiency of batch and semi-batch (CCRO) reverse osmosis desalination. *Water Research*, 106:272–282, 2016.

[23] Ronan K. McGovern and John H. Lienhard V. On the potential of forward osmosis to energetically outperform reverse osmosis desalination. *Journal of Membrane Science*, 469:245–250, 2014.

[24] David M. Warsinger, Karan H. Mistry, Kishor G. Nayar, Hyung Won Chung, and John H. Lienhard V. Entropy generation of desalination powered by variable temperature waste heat. *Entropy*, 17(11):7530–7566, 2015.

[25] David M. Warsinger, Jaichander Swaminathan, Elena Guillen-Burrieza, Hassan A. Arafat, and John H. Lienhard V. Scaling and fouling in membrane distillation for desalination applications: A review. *Desalination*, 356:294–313, 2015.

[26] D. E. Potts, Robert C. Ahlert, and Shaw S. Wang. A critical review of fouling of reverse osmosis membranes. *Desalination*, 36:235–264, 1981.

[27] Qianhong She, Rong Wang, Anthony G. Fane, and Chuyang Y. Tang. Membrane fouling in osmotically driven membrane processes: A review. *Journal of Membrane Science*, 499:201–233, 2016.

[28] Min Luo and Zhangsheng Wang. Complex fouling and cleaning-in-place of a reverse osmosis desalination system. *Desalination*, 141(1):15–22, 2001.

[29] Eric M.V. Hoek, Jeff Allred, Tom Knoell, and Byeong-Heon Jeong. Modeling the effects of fouling on full-scale reverse osmosis processes. *Journal of Membrane Science*, 314(1–2):33–49, 2008.

[30] Tom Pankratz, Fuzzy logic: Oilfield brine management, in: Water Desalination Report, Media Analytics, Houston, TX, 48(14):1–3, 2012.

[31] Shuaifei Zhao, Linda Zou, Chuyang Y. Tang, and Dennis Mulcahy. Recent developments in forward osmosis: Opportunities and challenges. *Journal of Membrane Science*, 396:1–21, 2012.

[32] G. Prakash Narayan and John H. Lienhard V. Thermal design of humidification dehumidification systems for affordable small-scale desalination. *IDA Journal*, 4(3):24–34, 2012.

[33] Karim M. Chehayeb, G. Prakash Narayan, Syed M. Zubair, and John H. Lienhard V. Use of multiple extractions and injections to thermodynamically balance the humidification dehumidification desalination system. *International Journal of Heat and Mass Transfer*, 68:422–434, 2014.

[34] G. Prakash Narayan, Karim M. Chehayeb, Ronan K. McGovern, Gregory P. Thiel, Syed M. Zubair, and John H. Lienhard V. Thermodynamic balancing of the humidification dehumidification desalination system by mass extraction and injection. *International Journal of Heat and Mass Transfer*, 57(2):756–770, 2013.

[35] Ronan K. McGovern, Gregory P. Thiel, G. Prakash Narayan, Syed M. Zubair, and John H. Lienhard V. Performance limits of zero and single extraction humidification-dehumidification desalination systems. *Applied Energy*, 102:1081–1090, 2013.

[36] Gregory P. Thiel and John H. Lienhard V. Entropy generation in condensation in the presence of high concentrations of noncondensable gases. *International Journal of Heat and Mass Transfer*, 55(19–20):5133–5147, 2012.

[37] Gregory P. Thiel, Ronan K. McGovern, Syed M. Zubair, and John H. Lienhard V. Thermodynamic equipartition for increased second law efficiency. *Applied Energy*, 118:292–299, 2014.

[38] Karan H. Mistry and John H. Lienhard V. Generalized least energy of separation for desalination and other chemical separation processes. *Entropy*, 15(6):2046–2080, 2013.

[39] Adrian Bejan. *Advanced Engineering Thermodynamics, 3rd ed.* John Wiley & Sons, Inc., Hoboken, NJ, USA, 2006.

[40] Sui Zhang, Peng Wang, Xiuzhu Fu, and Tai-Shung Chung. Sustainable water recovery from oily wastewater via forward osmosis-membrane distillation (FO-MD). *Water Research*, 52:112–121, 2014.

[41] Ali Altaee and Guillermo Zaragoza. A conceptual design of low fouling and high recovery FO-MSF desalination plant. *Desalination*, 343:2–7, 2013.

[42] Raphael Semiat, Jacob Sapoznik, and David Hasson. Energy aspects in osmotic processes. *Desalination and Water Treatment*, 15(1–3):228–235, 2010.

[43] Devin L. Shaffer, Ngai Yin Yip, Jack Gilron, and Menachem Elimelech. Seawater desalination for agriculture by integrated forward and reverse osmosis: Improved product water quality for potentially less energy. *Journal of Membrane Science*, 415–416:1–8, 2012.

[44] Ali Altaee, Guillermo Zaragoza, and H. Rost van Tonningen. Comparison between forward osmosis-reverse osmosis and reverse osmosis processes for seawater desalination. *Desalination*, 336:50–57, 2014.

[45] Ethan Butler, Andrew Silva, Kyle Horton, Zachary Rom, Malgorzata Chwatko, Arie Havasov, and Jeffrey R. McCutcheon. Point of use water treatment with forward osmosis for emergency relief. *Desalination*, 312:23–30, 2013.

[46] Sherub Phuntsho, Ho Kyong Shon, Seungkwan Hong, Sangyoup Lee, and Saravanamuthu Vigneswaran. A novel low energy fertilizer driven forward osmosis desalination for direct fertigation: Evaluating the performance of fertilizer draw solutions. *Journal of Membrane Science*, 375(1–2):172–181, 2011.

[47] Laura A. Hoover, William A. Phillip, Alberto Tiraferri, Ngai Yin Yip, and Menachem Elimelech. Forward with osmosis: Emerging applications for greater sustainability. *Environmental Science & Technology*, 45(23):9824–9830, 2011.

[48] Chalida Klaysom, Tazhi Y. Cath, Tom Depuydt, and Ivo F. J. Vankelecom. Forward and pressure retarded osmosis: potential solutions for global challenges in energy and water supply. *Chem. Soc. Rev.*, 42:6959–6989, 2013.

[49] Baoxia Mi and Menachem Elimelech. Chemical and physical aspects of organic fouling of forward osmosis membranes. *Journal of Membrane Science*, 320(1–2):292–302, 2008.

[50] Leonardo D. Banchik, Mostafa H. Sharqawy, and John H. Lienhard V. Effectiveness-mass transfer units (epsilon-MTU) model of a reverse osmosis membrane mass exchanger. *Journal of Membrane Science*, 458:189–198, 2014.

[51] Ngai Yin Yip, Alberto Tiraferri, William A. Phillip, Jessica D. Schiffman, and Menachem Elimelech. High performance thin-film composite forward osmosis membrane. *Environmental Science & Technology*, 44(10):3812–3818, 2010.

[52] Laura Chekli, Sherub Phuntsho, Ho Kyong Shon, Saravanamuthu Vigneswaran, Jaya Kandasamy, and Amit Chanan. A review of draw solutes in forward osmosis process and their use in modern applications. *Desalination and Water Treatment*, 43(1–3):167–184, 2012.

[53] Andrea Achilli, Tzahi Y. Cath, Eric A. Marchand, and Amy E. Childress. The forward osmosis membrane bioreactor: A low fouling alternative to MBR processes. *Desalination*, 239(1–3):10–21, 2009.

[54] Ronan K. McGovern, Jordan P. Mizerak, Syed M. Zubair, and John H. Lienhard V. Three dimensionless parameters influencing the optimal membrane orientation for forward osmosis. *Journal of Membrane Science*, 458:104–110, 2014.

[55] Victor Darde, Willy J. M. van Well, Erling H. Stenby, and Kaj Thomsen. Modeling of carbon dioxide absorption by aqueous ammonia solutions using the extended UNIQUAC model. *Industrial & Engineering Chemistry Research*, 49(24):12663–12674, 2010.

[56] Donald D. Wagman. *The NBS tables of chemical thermodynamic properties: Selected values for inorganic and C1 and C2 organic substances in SI units*. American Chemical Society and the American Institute of Physics for the National Bureau of Standards., 1982.

[57] Asif Matin, Hafiz Z. Shafi, Minghui Wang, Zafarullah Khan, Karen K. Gleason, and Faizur A. Rahman. Reverse osmosis membranes surface-modified using an initiated chemical vapor deposition technique show resistance to alginate fouling under cross-flow conditions: Filtration & subsequent characterization. *Desalination*, 379:108–117, 2016.

[58] Elizabeth L. Farias, Kerry J. Howe, and Bruce M. Thomson. Spatial and temporal evolution of organic foulant layers on reverse osmosis membranes in wastewater reuse applications. *Water Research*, 58:102–110, 2014.

[59] Anh H. Nguyen, John E. Tobiason, and Kerry J. Howe. Fouling indices for low pressure hollow fiber membrane performance assessment. *Water Research*, 45(8):2627–2637, 2011.

[60] Eric M. V. Hoek and Menachem Elimelech. Cake-enhanced concentration polarization: A new fouling mechanism for salt-rejecting membranes. *Environmental Science & Technology*, 37(24):5581–5588, 2003.

[61] Johannes G. Wijmans and Richard W. Baker. The solution-diffusion model: a review. *Journal of Membrane Science*, 107(1–2):1–21, 1995.

[62] Endre Nagy. A general, resistance-in-series, salt- and water flux models for forward osmosis and pressure-retarded osmosis for energy generation. *Journal of Membrane Science*, 460:71–81, 2014.

[63] Anastasios J. Karabelas and Dimitris C. Sioutopoulos. New insights into organic gel fouling of reverse osmosis desalination membranes. *Desalination*, 368:114–126, 2015.

[64] Cheryl Simpliciano, Larissa Clark, Behrokh Asi, Nathan Chu, Maria Mercado, Steven Diaz, Michel Goedert, and Maryam Mobed-Miremadi. Cross-linked alginate film pore size determination using atomic force microscopy and validation using diffusivity determinations. *Journal of Surface Engineered Materials and Advanced Technology*, 3(4A):1–12, 2013.

[65] T.K. Perkins and O.C. Johnston. A review of diffusion and dispersion in porous media. *Society of Petroleum Engineers Journal*, 3(1):70–84, 1963.

[66] Yining Wang, Filicia Wicaksana, Chuyang Y. Tang, and Anthony G. Fane. Direct microscopic observation of forward osmosis membrane fouling. *Environmental Science & Technology*, 44(18):7102–7109, 2010.

[67] Kenneth S Pitzer. Thermodynamics of electrolytes. I. Theoretical basis and general equations. *The Journal of Physical Chemistry*, 77(2):268–277, 1973.

[68] Gregory P. Thiel and John H. Lienhard V. Treating produced water from hydraulic fracturing: Composition effects on scale formation and desalination system selection. *Desalination*, 346:54–69, 2014.

[69] Karan H. Mistry and John H. Lienhard V. Effect of nonideal solution behavior on desalination of a sodium chloride (NaCl) solution and comparison to seawater. *Journal of Energy Resources Technology*, 135(4):042003, 2013.

[70] Kishor G. Nayar, Mostafa H. Sharqawy, Leonardo D. Banchik, and John H. Lienhard V. Thermophysical properties of seawater: A review and new correlations that include pressure dependence. *Desalination*, 390:1–24, 2016.

[71] V. Vitagliano and Phillip A. Lyons. Diffusion coefficients for aqueous solutions of sodium chloride and barium chloride. *Journal of the American Chemical Society*, 78(8):1549–1552, 1956.

[72] Sangyoup Lee and Menachem Elimelech. Salt cleaning of organic-fouled reverse osmosis membranes. *Water Research*, 41(5):1134–1142, 2007.

[73] Robert A. Robinson and Robert H. Stokes. *Electrolyte Solutions: Second Revised Edition*. Dover Publications, Incorporated, 2012.

[74] Emily W. Tow and John H. Lienhard V. Heat transfer to a horizontal cylinder in a shallow bubble column. *International Journal of Heat and Mass Transfer*, 79:353–361, 2014.

[75] Emily W. Tow and John H. Lienhard V. Experiments and modeling of bubble column dehumidifier performance. *International Journal of Thermal Sciences*, 80:65 – 75, 2014.

[76] *HTI OsMem CTA-ES Membrane Specifications, Hydration Technology Innovations*, received in 2014.

[77] Jinjian Wu, Alison E. Contreras, and Qilin Li. Studying the impact of RO membrane surface functional groups on alginate fouling in seawater desalination. *Journal of Membrane Science*, 458:120–127, 2014.

[78] Muhammad Tariq Khan, Markus Busch, Veronica Garcia Molina, Abdul-Hamid Emwas, Cyril Aubry, and Jean-Philippe Croue. How different is the composition of the fouling layer of wastewater reuse and seawater desalination RO membranes? *Water Research*, 59:271–282, 2014.

[79] Yun Ye, Pierre Le Clech, Vicki Chen, Anthony G. Fane, and Bruce Jefferson. Fouling mechanisms of alginate solutions as model extracellular polymeric substances. *Desalination*, 175(1):7–20, 2005.

[80] Edwin R. Morris, David A. Rees, David Thom, and Jonathan Boyd. Chiroptical and stoichiometric evidence of a specific, primary dimerisation process in alginate gelation. *Carbohydrate Research*, 66(1):145–154, 1978.

[81] Isabelle Braccini and Serge Perez. Molecular basis of Ca^{2+}-induced gelation in alginates and pectins: The egg-box model revisited. *Biomacromolecules*, 2(4):1089–1096, 2001.

[82] Arne Haug and Olav Smidsrod. The effect of divalent metals on the properties of alginate solutions II: Comparison of different metal ions. *Acta Chemica Scandinavica*, 19:341–351, 1965.

[83] Tanyarut Boontheekul, Hyun-Joon Kong, and David J. Mooney. Controlling alginate gel degradation utilizing partial oxidation and bimodal molecular weight distribution. *Biomaterials*, 26(15):2455–2465, 2005.

[84] Joachim Klein, Jurgen Stock, and Klaus-Dieter Vorlop. Pore size and properties of spherical Ca-alginate biocatalysts. *European Journal of Applied Microbiology and Biotechnology*, 18(2):86–91, 1983.

[85] Molly S. Shoichet, Rebecca H. Li, Melissa L. White, and Shelley R. Winn. Stability of hydrogels used in cell encapsulation: An in vitro comparison of alginate and agarose. *Biotechnology and Bioengineering*, 50(4):374–381, 1996.

[86] John S. Sperry, Nicanor Z. Saliendra, William T. Pockman, Herve Cochard, Pierre Cruiziat, Stephen D. Davis, Frank W. Ewers, and Melvin T. Tyree. New evidence for large negative xylem pressures and their measurement by the pressure chamber method. *Plant, Cell & Environment*, 19(4):427–436, 1996.

[87] Jennifer S. Louie, Ingo Pinnau, Isabelle Ciobanu, Kenneth P. Ishida, Alvin Ng, and Martin Reinhard. Effects of polyether-polyamide block copolymer coating on performance and fouling of reverse osmosis membranes. *Journal of Membrane Science*, 280(1–2):762–770, 2006.

[88] Bilal A. Qureshi, Syed M. Zubair, Anwar K. Sheikh, Aditya Bhujle, and Steven Dubowsky. Design and performance evaluation of reverse osmosis desalination systems: An emphasis on fouling modeling. *Applied Thermal Engineering*, 60(1–2):208–217, 2013.

[89] Emily W. Tow and John H. Lienhard V. Unpacking compaction: Effect of hydraulic pressure on alginate fouling. *Submitted for publication*, 2017.

[90] Robert L. McGinnis and Menachem Elimelech. Energy requirements of ammonia-acarbon dioxide forward osmosis desalination. *Desalination*, 207(1–3):370–382, 2007.

[91] Raphael Semiat. Energy issues in desalination processes. *Environmental Science & Technology*, 42(22):8193–8201, 2008.

[92] Devin L. Shaffer, Jay R. Werber, Humberto Jaramillo, Shihong Lin, and Menachem Elimelech. Forward osmosis: Where are we now? *Desalination*, 356:271–284, 2015.

[93] Youngpil Chun, François Zaviska, Sung-Jo Kim, Dennis Mulcahy, Euntae Yang, In S. Kim, and Linda Zou. Fouling characteristics and their implications on cleaning of a FO-RO pilot process for treating brackish surface water. *Desalination*, 394:91–100, 2016.

[94] Chanhee Boo, Menachem Elimelech, and Seungkwan Hong. Fouling control in a forward osmosis process integrating seawater desalination and wastewater reclamation. *Journal of Membrane Science*, 444:148–156, 2013.

[95] Ryan W. Holloway, Amy E. Childress, Keith E. Dennett, and Tzahi Y. Cath. Forward osmosis for concentration of anaerobic digester centrate. *Water Research*, 41(17):4005–4014, 2007.

[96] Guanglei Qiu and Yen-Peng Ting. Short-term fouling propensity and flux behavior in an osmotic membrane bioreactor for wastewater treatment. *Desalination*, 332(1):91–99, 2014.

[97] Winson C. L. Lay, Chong Tzyy Haur, Chuyang Y. Tang, Anthony G. Fane, Zhang Jinsong, and Liu Yu. Fouling propensity of forward osmosis: investigation of the slower flux decline phenomenon. *Water Science & Technology*, 61(4):927–936, 2010.

[98] Sarah E. Kwan, Edo Bar-Zeev, and Menachem Elimelech. Biofouling in forward osmosis and reverse osmosis: Measurements and mechanisms. *Journal of Membrane Science*, 493:703–708, 2015.

[99] Stoerker T. Moe, Gundmund Skjaak-Braek, Arnljot Elgsaeter, and Olav Smidsrod. Swelling of covalently crosslinked alginate gels: influence of ionic solutes and nonpolar solvents. *Macromolecules*, 26(14):3589–3597, 1993.

[100] Robert W. Field, Dengxi Wu, John A. Howell, and Bharat B. Gupta. Critical flux concept for microfiltration fouling. *Journal of Membrane Science*, 100(3):259–272, 1995.

[101] Changxiang Wang, C. Cowen, Zhibing Zhang, and Colin R. Thomas. High-speed compression of single alginate microspheres. *Chemical Engineering Science*, 60(23):6649–6657, 2005.

[102] Ali S. Argon, Stanley Backer, Frank A. McClintock, George S. Reichenbach, Egon Orowan, Milton C. Shaw, and Ernest Rabinowicz. *Mechanical Behavior of Materials*. Addison-Wesley Publishing Company, Inc., 1966.

[103] David Cohen-Tanugi and Jeffrey C. Grossman. Water desalination across nanoporous graphene. *Nano Letters*, 12(7):3602–3608, 2012.

[104] Donald R. Paul. Reformulation of the solution-diffusion theory of reverse osmosis. *Journal of Membrane Science*, 241(2):371–386, 2004.

[105] Donald R. Paul. The role of membrane pressure in reverse osmosis. *Journal of Applied Polymer Science*, 16(3):771–782, 1972.

[106] Takahiro Fujioka, Nagayasu Oshima, Ryoichi Suzuki, William E. Price, and Long D. Nghiem. Probing the internal structure of reverse osmosis membranes by positron annihilation spectroscopy: Gaining more insight into the transport of water and small solutes. *Journal of Membrane Science*, 486:106–118, 2015.

[107] Behzad Ghanbarian, Allen G. Hunt, Robert P. Ewing, and Muhammad Sahimi. Tortuosity in porous media: A critical review. *Soil Science Society of America Journal*, 77:1461–1477, 2013.

[108] Evelyne Mauret and Maurice Renaud. Transport phenomena in multi-particle systems–I. Limits of applicability of capillary model in high voidage beds-application to fixed beds of fibers and fluidized beds of spheres. *Chemical Engineering Science*, 52(11):1807–1817, 1997.

[109] Jia Shin Ho, Lee Nuang Sim, Jun Gu, Richard D. Webster, Anthony G. Fane, and Hans G.L. Coster. A threshold flux phenomenon for colloidal fouling in reverse osmosis characterized by transmembrane pressure and electrical impedance spectroscopy. *Journal of Membrane Science*, 500:55–65, 2016.

[110] Olav Smidsrod. Molecular basis for some physical properties of alginates in the gel state. *Faraday Discussions of the Chemical Society*, 57:263–274, 1974.

[111] Emily W. Tow and John H. Lienhard V. Effect of pressure on alginate fouling in forward osmosis. In *AMTA/AWWA Membrane Technology Conference*, Long Beach, CA, USA, Feb. 13–17, 2017.

[112] Taylor A. Swift. "Shake It Off," *1989*. 2014.

[113] Boris Liberman and Igal Liberman. Forward osmotic and water hammer method of membrane cleaning, 2016. WO Patent App. PCT/IB2015/055,665.

[114] Olav Smidsrod and Arne Haug. The effect of divalent metals on the properties of alginate solutions: I. Calcium ions. *Acta Chemica Scandinavica*, 19:329–340, 1965.

[115] Michelle A. LeRoux, Farshid Guilak, and Lori A. Setton. Compressive and shear properties of alginate gel: Effects of sodium ions and alginate concentration. *Journal of Biomedical Materials Research*, 47(1):46–53, 1999.

[116] Emily W. Tow, David E. M. Warsinger, Jaichander Swaminathan, Ali M. Trueworthy, Gregory P. Thiel, Syed M. Zubair, Allan S. Myerson, and John H. Lienhard V. Comparison of fouling propensity between reverse osmosis, forward osmosis, and membrane distillation. *In preparation*, 2017.

[117] Jaichander Swaminathan, Hyung Won Chung, David M. Warsinger, and John H. Lienhard V. Membrane distillation model based on heat exchanger theory and configuration comparison. *Applied Energy*, 184:491–505, 2016.

[118] Muhammad Tauha Ali, Hassan E.S. Fath, and Peter R. Armstrong. A comprehensive techno-economical review of indirect solar desalination. *Renewable and Sustainable Energy Reviews*, 15(8):4187–4199, 2011.

[119] Ashraf S. Hassan and Hassan E.S. Fath. Review and assessment of the newly developed MD for desalination processes. *Desalination and Water Treatment*, 51(1–3):574–585, 2013.

[120] Baoxia Mi and Menachem Elimelech. Gypsum scaling and cleaning in forward osmosis: Measurements and mechanisms. *Environmental Science & Technology*, 44(6):2022–2028, 2010.

[121] David E. M. Warsinger, Emily W. Tow, Jaichander Swaminathan, and John H. Lienhard V. Theoretical framework for predicting inorganic fouling in membrane distillation and experimental validation with calcium sulfate. *Journal of Membrane Science*, 528:381–390, 2016.

[122] David M. Warsinger, Amelia Servi, Sarah Van Belleghem, Jocelyn Gonzalez, Jaichander Swaminathan, Jehad Kharraz, Hyung Won Chung, Hassan A. Arafat, Karen K. Gleason, and John H. Lienhard V. Combining air recharging and membrane superhydrophobicity for fouling prevention in membrane distillation. *Journal of Membrane Science*, 505:241 – 252, 2016.

[123] Youngbin Baek, Junil Kang, Patrick Theato, and Jeyong Yoon. Measuring hydrophilicity of RO membranes by contact angles via sessile drop and captive bubble method: A comparative study. *Desalination*, 303:23 – 28, 2012.

[124] Kevin W. Lawson and Douglas R. Lloyd. Membrane distillation. *Journal of Membrane Science*, 124(1):1–25, 1997.

[125] Abdulaziz M. Alklaibi and Noam Lior. Membrane-distillation desalination: Status and potential. *Desalination*, 171(2):111–131, 2005.

[126] Bhausaheb L. Pangarkar, Mukund G. Sane, and Mahendra Guddad. Reverse osmosis and membrane distillation for desalination of groundwater: A review. *ISRN Materials Science*, 2011, 2011.

[127] Leonard D. Tijing, Yun Chul Woo, June-Seok Choi, Sangho Lee, Seung-Hyun Kim, and Ho Kyong Shon. Fouling and its control in membrane distillation–a review. *Journal of Membrane Science*, 475:215–244, 2015.

[128] Shiliang He, John E. Oddo, and Mason B. Tomson. The nucleation kinetics of calcium sulfate dihydrate in nacl solutions up to 6 m and 90°C. *Journal of Colloid and Interface Science*, 162(2):297–303, 1994.

[129] Brahim Messnaoui and Tijani Bounahmidi. On the modeling of calcium sulfate solubility in aqueous solutions. *Fluid Phase Equilibria*, 244(2):117–127, 2006.

[130] Long D. Nghiem and Tzahi Cath. A scaling mitigation approach during direct contact membrane distillation. *Separation and Purification Technology*, 80(2):315–322, 2011.

[131] Hung C. Duong, Mikel Duke, Stephen Gray, Paul Cooper, and Long D. Nghiem. Membrane scaling and prevention techniques during seawater desalination by air gap membrane distillation. *Desalination*, 397:92–100, 2016.

[132] Youngjin Kim, Songbok Lee, Ho Kyong Shon, and Seungkwan Hong. Organic fouling mechanisms in forward osmosis membrane process under elevated feed and draw solution temperatures. *Desalination*, 355:169–177, 2015.

[133] William J. Leo, Aiden J. McLoughlin, and Dermot M. Malone. Effects of sterilization treatments on some properties of alginate solutions and gels. *Biotechnology Progress*, 6(1):51–53, 1990.

[134] Edward K. Summers, Hassan A. Arafat, and John H. Lienhard V. Energy efficiency comparison of single-stage membrane distillation (MD) desalination cycles in different configurations. *Desalination*, 290:54–66, 2012.

[135] Shuwen Goh, Qiaoyun Zhang, Jinsong Zhang, Diane McDougald, William B. Krantz, Yu Liu, and Anthony G. Fane. Impact of a biofouling layer on the vapor pressure driving force and performance of a membrane distillation process. *Journal of Membrane Science*, 438:140–152, 2013.

[136] Jongho Lee and Rohit Karnik. Desalination of water by vapor-phase transport through hydrophobic nanopores. *Journal of Applied Physics*, 108(4):044315, 2010.

[137] David M. Warsinger, Jaichander Swaminathan, Hyung Won Chung, Seongpil Jeong, and John H. Lienhard V. The effect of filtration and particulate fouling in membrane distilliation. In *Proceedings of The International Desalination Association World Congress on Desalination and Water Reuse, San Diego, CA, USA*, August 2015.

[138] Anthony F. Mills. *Basic Heat and Mass Transfer*. Prentice Hall, 1999.

[139] Yuan-Hui Li and Sandra Gregory. Diffusion of ions in sea water and in deep-sea sediments. *Geochimica et Cosmochimica Acta*, 38(5):703–714, 1974.

[140] Ronan Killian McGovern, Dillon McConnon, and John H. Lienhard V. The effect of very high hydraulic pressure on the permeability and salt rejection of reverse osmosis membranes. In *IDA World Congress on Desalination and Water Reuse*, San Diego, CA, 2015.

[141] Georges Belfort, Robert H. Davis, and Andrew L. Zydney. The behavior of suspensions and macromolecular solutions in crossflow microfiltration. *Journal of Membrane Science*, 96(1):1–58, 1994.

[142] Surapit Srisurichan, Ratana Jiraratananon, and A.G. Fane. Mass transfer mechanisms and transport resistances in direct contact membrane distillation process. *Journal of Membrane Science*, 277(1–2):186–194, 2006.

[143] Marek Gryta. Fouling in direct contact membrane distillation process. *Journal of Membrane Science*, 325(1):383–394, 2008.

[144] Anurag P Mairal, Alan R Greenberg, William B Krantz, and Leonard J Bond. Real-time measurement of inorganic fouling of RO desalination membranes using ultrasonic time-domain reflectometry. *Journal of Membrane Science*, 159(1–2):185–196, 1999.

[145] Jianxin Li, V Yu Hallbauer-Zadorozhnaya, D. K. Hallbauer, and R. D. Sanderson. Cake-layer deposition, growth, and compressibility during microfiltration measured and modeled using a noninvasive ultrasonic technique. *Industrial & engineering chemistry research*, 41(16):4106–4115, 2002.

[146] Hongyu Li, Anthony G. Fane, Hans G.L. Coster, and Saravanamuth Vigneswaran. Direct observation of particle deposition on the membrane surface during crossflow microfiltration. *Journal of Membrane Science*, 149(1):83–97, 1998.

[147] John Thompson, Nancy Lin, Eric Lyster, Ronit Arbel, Tom Knoell, Jack Gilron, and Yoram Cohen. RO membrane mineral scaling in the presence of a biofilm. *Journal of Membrane Science*, 415-416:181–191, 2012.

[148] Qiming Wang and Xuanhe Zhao. A three-dimensional phase diagram of growth-induced surface instabilities. *Scientific Reports*, 5:8887, 2015.

[149] Changwoo Kim, Sangyoup Lee, and Seungkwan Hong. Application of osmotic backwashing in forward osmosis: mechanisms and factors involved. *Desalination and Water Treatment*, 43(1–3):314–322, 2012.

[150] Chuyang Y. Tang, Qianhong She, Winson C.L. Lay, Rong Wang, and Anthony G. Fane. Coupled effects of internal concentration polarization and fouling on flux behavior of forward osmosis membranes during humic acid filtration. *Journal of Membrane Science*, 354(1–2):123–133, 2010.

[151] John L. Anderson and Dermot M. Malone. Mechanism of osmotic flow in porous membranes. *Biophysical Journal*, 14(12):957–982, 1974.

[152] David M. Warsinger, Sudip Chakraborty, Emily W. Tow, Megan H. Plumleee, Savvina Loutatidou, Christopher Bellona, Leila Karimi, Anne M. Mikelonis, Andrea Achilli, Abbas Ghassemi, Lokesh P. Padhye, Shane A. Snyder, Stefano

Curcio, Chad Vecitis, Hassan A. Arafat, and John H. Lienhard V. A review of polymeric membranes and processes for potable water reuse. *Submitted for publication*, 2017.

[153] *DOW FILMTEC SW30HR380 Element Product Data Sheet, Dow Water & Process Solutions*, 2015.

[154] Chrysafenia P. Koutsou, Stergios G. Yiantsios, and Anastasios J. Karabelas. A numerical and experimental study of mass transfer in spacer-filled channels: Effects of spacer geometrical characteristics and Schmidt number. *Journal of Membrane Science*, 326(1):234–251, 2009.

[155] Xue Jin, Anna Jawor, Suhan Kim, and Eric M.V. Hoek. Effects of feed water temperature on separation performance and organic fouling of brackish water RO membranes. *Desalination*, 239(1–3):346–359, 2009.

[156] *FILMTEC(TM) Reverse Osmosis Membranes Technical Manual, Dow Water & Process Solutions*, 2011.

[157] Thomas G. Beckwith, Roy D. Marangoni, and John H. Lienhard V. *Mechanical Measurements, 6th edition*. Pearson, 2007.